Bandgap-universal passivation enables stable perovskite solar cells with low photovoltage loss

Authors: Yen-Hung Lin[1,2,3*], Vikram[4,†], Fengning Yang[1,†], Xue-Li Cao[2,3†], Akash Dasgupta[1,†], Robert D. J. Oliver[1,5,†], Aleksander M. Ulatowski[1,†], Melissa M. McCarthy[1], Xinyi Shen[1], Qimu Yuan[1], M. Greyson Christoforo[1], Fion Sze Yan Yeung[2,3], Michael B. Johnston[1], Nakita K. Noel[1], Laura M. Herz[1], M. Saiful Islam[4], Henry J. Snaith[1,*]

Affiliations:

[1]Department of Physics, University of Oxford; Clarendon Laboratory, Parks Road, Oxford, OX1 3PU, U.K.

[2]Department of Electronic and Computer Engineering, The Hong Kong University of Science and Technology; Clear Water Bay, Kowloon, Hong Kong SAR.

[3]State Key Laboratory of Advanced Displays and Optoelectronics Technologies, The Hong Kong University of Science and Technology; Clear Water Bay, Kowloon, Hong Kong SAR.

[4]Department of Materials, University of Oxford; Parks Road, Oxford, OX1 3PH, U.K.

[5]Department of Materials Science and Engineering, University of Sheffield; Mappin Street, Sheffield, S1 3JD, U.K.

*Corresponding authors. Emails: yh.lin@ust.hk , henry.snaith@physics.ox.ac.uk

†These authors contributed equally to this work.

Abstract: Efficiency and longevity of metal-halide perovskite solar cells are typically dictated by non-radiative defect-mediated charge recombination. Here, we demonstrate a vapor-based amino-silane passivation that reduces photovoltage deficits from 100 to 120 millivolts (> 90% of the thermodynamic limit) in perovskite solar cells of bandgaps between 1.6 and 1.8 electron volts, crucial for tandem applications. Primary, secondary, or tertiary-amino silane alone negatively affected or barely impacted perovskite crystallinity and charge transport, but amino-silanes incorporating primary and secondary amines yield up to a 60-fold increase in photoluminescence quantum yield and preserve long-range conduction. Amino-silane-treated devices retained 95% power conversion efficiency for more than 1,500 hours under full-spectrum sunlight at 85 degrees Celsius and open-circuit conditions in ambient air with a relative humidity of 50 to 60%.

One-Sentence Summary: A molecular strategy transcends limitations posed to perovskite solar cells by enhancing operational stability and surpassing photovoltage thresholds.

Main Text: Although metal-halide perovskites are considered "defect-tolerant" (*1, 2*), they still require careful crystallization and growth (*3, 4*) and defect passivation via molecular bonding (*5*) or incorporating organic cations that form low-dimensional perovskites which interface to form a passivation "heterojunction" with the three-dimensional perovskite (*6-8*) to reach the highest power conversion efficiency (PCE) and exhibit improved long-term operational stability in optoelectronic devices (*9-11*). For isolated perovskite thin films or nanocrystals, a broad range of approaches can be adopted, including the use of molecular Lewis acids or bases (*12, 13*) and ligands that are typically used in nanocrystal growth, such as trioctylphosphine oxide (*14*) and oleic acid (*15*). Large organic molecules that can lead to internal luminescence efficiency approaching unity in polycrystalline perovskite films (*16*) and yield stable passivation often inhibit charge-carrier transport in perovskite films and have yet to be demonstrated in high-performance solar cells (*17*).

For more molecularly defined passivation, amine-based functional groups have emerged as a key component because of their strong binding energies to the perovskite surface (*18-21*). Despite demonstrating exceptional photoluminescence quantum yield (PLQY) properties in passivated perovskite films, some of these amine-based molecular passivation strategies have yet to be proven effective in achieving high efficiency or photovoltaic (PV) parameters near the radiative limit (*18-20*). The challenge in translating the enhanced PLQY observed in passivated perovskite films into comparable PCE gains in full solar cell devices underscores a gap in our current understanding.

This gap pertains to how amine-based and, more broadly, Lewis-base-based molecules contribute to effective defect passivation (*18-21*). Additionally, optimizing passivation strategies for wider bandgap perovskites, which consist of mixed halides and cations, remains crucial for the development of tandem solar cells (*22*). This need is especially pertinent since most current passivation strategies are predominately designed for narrow bandgap perovskites with compositions near $FAPbI_3$ (where FA is formamidinium) (*9, 21, 23, 24*), thereby lacking versatile strategies applicable across a broader spectrum of perovskite compositions.

Here, we used a series of amino-silane molecules (Fig. 1A) with various types of amines (primary, secondary, tertiary, or their combinations) to explore the underlying optoelectronic and material mechanisms and devise a universal passivation strategy for perovskites with bandgaps ranging from 1.6 to 1.8 eV. Using the identified efficient amino-silane molecules, we demonstrate medium-area (0.25 cm^2) and large-area (1 cm^2) perovskite solar cells exhibiting power conversion efficiencies derived from maximum power point tracking (MPPT) to reach 22.4 and 21.9%, 20.7 and 20.1%, and 18.6 and 18.4%, for 1.60-, 1.67-, and 1.77-eV mixed-cation, mixed-anion based perovskites, respectively.

All perovskite solar cells passivated with the best performing amino-silane molecular compound achieved photovoltage deficits as low as 100 to 120 mV, thus surpassing 90% of the maximum photovoltage dictated by thermodynamic detailed balance theory. Furthermore, our passivation strategy notably enhanced the durability of perovskite solar cells, allowing them to retain 95% efficiency for more than 1,500 hours under full spectrum simulated sunlight. Our aging was conducted without ultraviolet (UV) filters, at an elevated temperature of 85 °C, and under open-circuit conditions in ambient air with a relative humidity of 50 to 60%.

Impacts of amino-silane molecules on metal-halide perovskites

We investigated the impact of primary-amine based (3-aminopropyl)trimethoxysilane (APTMS, see Fig. 1A) molecules using vapor phase treatment on mixed-cation lead mixed-anion perovskite thin films and their corresponding positive-intrinsic-negative (p-i-n) perovskite solar cells. We show schematics of the device architecture and the film passivation process in Fig. 1, B and C, respectively. For the perovskite light absorber, we used an "MA-free" (where MA = methylammonium) composition, $Cs_{0.13}FA_{0.87}Pb(I_{0.9}Br_{0.1})_3$, hereafter abbreviated as $Cs_{13}Br_{10}$, that had a bandgap of 1.6 eV and was suitable for the middle sub-cell of triple-junction perovskite tandem solar cells (*25*). Here, we measured a substantial increase in PLQY (from ~ 6% to 24%) for perovskite films before and after the APTMS treatment.

For integration into p-i-n PV devices, we used [4-(3,6-dimethyl-9H-carbazol-9-yl)butyl]phosphonic acid (Me-4PACz) and [6,6]-phenyl-C61-butyric acid methyl ester ($PC_{61}BM$), as the hole transport and electron transport materials, respectively. For further details, we described the full device fabrication protocol in the materials and methods section of the supplementary materials. The current density-voltage (J-V) characteristics and other corresponding PV performance parameters obtained from our APTMS-treated and reference solar cells are shown in fig. S1. Despite the boost in PLQY of the isolated perovskite films, the PV performance of APTMS-treated cells was poor, much worse than our reference cells, and exhibited substantial hysteresis in the J-V characteristics. This unexpected outcome led us to delve deeper into the effects of passivation using amino-silane molecules.

Silane molecules are used to treat silicon wafers to alter their surface properties (*26*), where Si-O-Si bonds are formed, and the additional moieties alter the surface energy of the wafer. The treatments do not necessarily lead to a single molecular monolayer, and thicker cross-linked films of (hydrated) silicon oxide can form. When treating the perovskite films with amino-silane molecules, like APTMS, both the silane units and the amine units may interact with the perovskite surface and each other, hence influencing their growth (*18, 19*).

To understand how the structure of amino-silane molecules impacts perovskites, apart from APTMS, we treated perovskite thin films with amino-silane molecules with various types of amines and silane molecules alone. These molecules include secondary-amine based trimethoxy[3-(methylamino)propyl]silane (MAPTMS), tertiary-amine based (*N*, *N*-Dimethylaminopropyl)trimethoxysilane (DMAPTMS), primary- and secondary-amine based [3-(2-aminoethylamino)propyl]trimethoxysilane (AEAPTMS) and 3-[2-(2-aminoethylamino)ethylamino]propyltrimethoxysilane [$(AE)_2$APTMS], as well as the alkyl-silane molecule, trimethoxy(propyl)silane (PTMS), absent of amine moieties. The corresponding molecular structures are drawn in Fig. 1A. In Fig. 1D, we show photographs of perovskite films treated with these (amino-)silane molecules and a reference film without any treatment.

We examined perovskite thin films with the compositions of $Cs_{13}Br_{10}$ and $Cs_{0.15}FA_{0.85}Pb(I_{0.6}Br_{0.4})_3$, hereafter abbreviated as $Cs_{15}Br_{40}$. The latter had a photovoltaic bandgap of 1.77 eV (*27*) and is widely used as the top cell in perovskite/perovskite tandem solar cells (*28-30*). Except for PTMS, all of the amino-silane molecules improved the PLQY for $Cs_{13}Br_{10}$ as compared to the reference (as shown in Fig. 1E), whereas for $Cs_{15}Br_{40}$, the PLQY was improved after treatment with all of the molecules apart from PTMS and DMAPTMS (fig. S2). In particular, for the wider bandgap $Cs_{15}Br_{40}$ perovskite, we only observed an increase in PLQY from ~ 1.5 to

3% for the APTMS treatment. However, this value increased to > 7% and to > 20% for the AEAPTMS and $(AE)_2$APTMS treatments, respectively.

We then conducted a series of PLQY measurements under 1-sun equivalent photoexcitation on a variety of perovskite films and "half-stacks". These were composed of either indium tin oxide (ITO) glass/hole transport layer (HTL, Me-4PACz with a wetting layer formed of aluminum oxide nanoparticles)/perovskite, or glass/aluminum oxide nanoparticles/perovskite/electron transport layer (ETL, containing $PC_{61}BM$ with a hole blocking layer formed of bathocuproine, BCP) using AEAPTMS (figs. S3 to S5). We observed the most significant improvement in PLQY from the amino-silane molecules that contain both primary and secondary amine groups [i.e., AEAPTMS and $(AE)_2$APTMS, Fig. 1E].

Since PLQY is indicative of a solar cell's behavior at the open-circuit condition, maximized PL in these half-stacks is crucial for achieving higher photovoltages due to reducing non-radiative recombination losses. For example, perovskite/ETL films treated with AEAPTMS molecules, including $Cs_{13}Br_{10}$, $Cs_{15}Br_{40}$ and $Cs_{0.17}FA_{0.83}Pb(I_{0.77}Br_{0.23})_3$, hereafter abbreviated as $Cs_{17}Br_{23}$, had a staggering 60-fold increase in PLQY (see fig. S4A), with the PLQY for the glass substrate/$Cs_{15}Br_{40}$/ETL stack increasing from 0.07% for the control, to 4.1% for the AEAPTMS treated films. In fig. S4B, we also show their corresponding calculated quasi-Fermi level splitting (QFLS) values for further comparison (*31*). Thus, the AEAPTMS passivation specifically inhibited nonradiative recombination at the perovskite/ETL interface, which is generally regarded as the most lossy part in a p-i-n perovskite solar cell (*27, 32*).

Because we observed the largest enhancement in the PLQY for the perovskite composition of $Cs_{13}Br_{10}$ when using APTMS, we performed UV-visible absorption spectroscopy and non-contact transient terahertz (THz) photoconductivity measurements on $Cs_{13}Br_{10}$ films to probe the impact of the amino-silane passivation further. In fig. S6, we show UV-visible absorption spectra of $Cs_{13}Br_{10}$ perovskite films with and without passivation. For the perovskite film passivated with APTMS, we observed a considerable reduction in the optical density, less than half over the entire absorption range, indicating a bulk change to the perovskite film after passivation rather than just at the surface. All of the other passivated films exhibited a small reduction in optical absorption in comparison to the reference film.

Optical pump THz probe spectroscopy reveals the change in conductivity of a sample after photoexcitation and can be used to determine the "short-range" charge-carrier mobility (see the supplementary text section). This technique revealed surprising differences between our perovskite films (Fig. 1F and figs. S7 and S8). For the reference films, the sum of electron and hole mobilities was ~ 60 $cm^2\ V^{-1}\ s^{-1}$, which is a high value for lead-halide perovskites (*33*). For all of the passivation treatments, apart from PTMS, the mobilities were reduced (Fig. 1F). For the APTMS-treated $Cs_{13}Br_{10}$ film, this reduction in mobility was precipitous, with values dropping to 1.5 $cm^2\ V^{-1}\ s^{-1}$. This drop in mobility indicates a major disruption to the crystalline order throughout the APTMS-treated perovskite films on a length scale short enough to inhibit the THz-derived charge carrier mobility. In contrast, the reduction in charge-carrier mobility was much less severe for the other passivation molecules investigated; for example, we determined a sum mobility of 46 $cm^2\ V^{-1}\ s^{-1}$ for the AEAPTMS-treated films.

With such a severe disruption to crystalline order for the APTMS-treated films, inferred from both the drop in THz mobility and the optical absorption strength, we tried to discern changes in the morphology or crystallinity of the thin films by electron microscopy or x-ray diffraction (XRD).

We first investigated the influence of different amino-silane molecules on the film formation quality by examining the surface morphology of the $Cs_{13}Br_{10}$ perovskite films by scanning electron microscopy (SEM, fig. S9). We observed the characteristic polycrystalline morphology in all of the perovskite films with apparent grain sizes in the range of 150 to 200 nm. However, SEM images are a very coarse indication of grain size, and there are many examples with metal halide perovskites where the crystalline domain size, as studied by high-resolution electron microscopy, is much smaller than the apparent size in SEM images (*34*, *35*). The apparent grains observed in SEM images of the APTMS-treated perovskite film, although resembling those in the reference in size, could equally represent interaggregate grains of much smaller sizes rather than genuine grains of single crystalline domains. In addition to the apparent remaining grains, for both the APTMS- and MAPTMS-treated perovskite films, more than 50% of the film surfaces appear to be ill-defined and "cloudy." This effect could be caused by a complete change to the morphology within these regions, or a thick "capping layer" of an amorphous material being present. For the AEAPTMS and $(AE)_2$APTMS treated films, the polycrystalline structures were discernible over the entire surface area, but there is more "haziness" to the images, suggestive of a surface coating with an insulating material.

In fig. S10, we show XRD 2θ plots for the series of treated films, which again revealed striking differences. The XRD traces of PTMS-, DMAPTMS-, and AEAPTMS-treated $Cs_{13}Br_{10}$ films did not differ appreciably from that of the untreated reference films, and all exhibited the characteristic XRD pattern of polycrystalline perovskite films without any additional diffraction peaks or changes in scattering intensities (*36*). For the $(AE)_2$APTMS-treated perovskite film, we observed a slight decrease in peak intensities, with the full-width at half-maximum (FWHM) of the perovskite peaks broadening. Meanwhile the corresponding peaks for the AEAPTMS-treated film showed narrowing FWHM values compared with the untreated perovskite film (see the supplementary text and the supplementary table S1). However, for the APTMS-treated $Cs_{13}Br_{10}$ film, all of the scattering peaks were reduced in intensity by more than an order of magnitude.

The THz mobility measurements, XRD patterns, and UV-vis absorption spectra taken together indicate that the APTMS molecules strongly influenced the crystallinity throughout perovskite films, introducing short-range scattering defects or disrupting the crystalline domains to such an extent that the charge carriers underwent short-range scattering and had severely limited charge carrier mobility. However, for previous measurements of perovskite nanocrystals with a crystal diameter of 10 nm, the charge-carrier mobility is only reduced by a factor of 3, versus the bulk mobility in a polycrystalline $CsPbBr_3$ film (*33*, *37*). Here, the reduction in mobility by a factor of 40 indicated that the complete break-up of the crystalline order, or introduction of charge-scattering sites, occurred on a much shorter length scale than 10 nm. In contrast, applying AEAPTMS and $(AE)_2$APTMS molecules appeared to leave the crystalline order and charge-carrier mobility largely unaffected, but still enables an equally substantial increase in PLQY.

Insights of passivation molecule formations and bonding interactions

Despite these results, it remained unclear why different types of amines, whether primary (such as APTMS) or secondary (such as MAPTMS) could have vastly different impacts on perovskite films. To explore how APTMS, MAPTMS, and AEAPTMS impacted metal halide perovskites in more detail, we used grazing-incidence wide-angle x-ray scattering (GIWAXS) to study their effects on the orientation and crystallinity of treated $Cs_{13}Br_{10}$ perovskite films. First, we used an ex-situ GIWAXS setup to survey as-treated perovskite thin films (figs. S11 and S12). We initially

used GIWAXS at a lower incidence angle (0.5°), which provides information about the surface region with an attenuation length of ~ 70 nm (see the supplementary text). For the APTMS-treated perovskite films, there were no clear Debye-Scherrer diffraction rings observed in the GIWAXS patterns (fig. S11), consistent with the 2θ XRD scans. In contrast, for the AEAPTMS-treated perovskite films, we observed a higher scattering intensity in the small angle GIWAXS scans than the untreated films.

At the higher incidence angle (1.5°), we obtained information about the deeper regions within the perovskite films. We observed continuous Debye-Scherrer diffraction rings, but with differing intensities, at scattering wavevector Q_{xy} =1.0, 1.4, 1.7, 2.0 $Å^{-1}$ in all of the APTMS-, AEAPTMS-, and MAPTMS-treated films (fig. S11), which, respectively, corresponded to (100), (110), (111) and (200) diffraction peaks in 1D XRD patterns (fig. S10). For the MAPTMS-treated perovskite films, a series of discrete scattering points in the low Q-space were observed that we assigned to a highly oriented two-dimensional (2D) species (figs. S11 and S12). The relative intensities of these peaks, in comparison with the main perovskite peaks, were higher in the low-angle GIWAXS scans, indicating that the material responsible was predominantly located near the top of the perovskite films. We further elaborate upon these observations, including their orientation and layer spacing, in the supplementary text and fig. S13.

Next, we used a synchrotron-based in-situ GIWAXS setup (see fig. S14) to gain insight into the evolution of perovskite film crystallinity during the vapor-based amino-silane treatment. For these measurements, our treatment conditions were adapted to be compatible with the synchrotron environment, so the treatment times were considerably extended. The in-situ time-dependent GIWAXS patterns are shown in Fig. 2A for the APTMS- and AEAPTMS-treated films, and the pattern evolutions were recorded in the supplementary movies 1 to 4.

The time-dependent GIWAXS patterns of the APTMS-treated perovskite films were highly revealing (Fig. 2A and the supplementary movies 1 and 2). Between 150 to 450 s, a highly intense series of low Q reflection rings appeared, indicating the emergence of larger d-spacing scattering features, which could, for example, be a lower dimensional perovskite phase. From ~ 600 s, the newly emerged low Q scattering rings and the main perovskite scattering rings rapidly faded until they become indiscernible after ~ 1,000 s. These results were consistent with the APTMS molecules first causing a structural transformation followed by “disintegration” of the perovskite structure.

Coupled with the knowledge that primary amines can strongly interact with and “solvate” metal halide perovskites (*38*, *39*), our observations indicated that the perovskite films underwent a solvation process during the APTMS treatment by reacting with primary amines, then crystallizing into an intermediate species with a larger d-spacing than the ABX_3 perovskites as seen in Fig. 2A and then completely breaking down and losing nearly all of their crystallinity. This APTMS-triggered solvation process resulted in a noticeable visual transformation of the treated films that caused them to become “hazier” and more transparent (see supplementary movie 5). The peculiarity is that the UV-vis absorption spectra indicated that at least half the absorption strength remained, and the PLQY remained extremely strong (Fig. 1E), with a small blueshift in the emission peak as compared to the reference perovskite films (fig. S15). These findings imply that the three-dimensional (3D) perovskite structure, while undergoing significant transformation, partially remained present in a modified but well-passivated form, corroborating our observation that exposure to APTMS molecules gradually solvate the 3D perovskite phase (Fig. 2A).

For the AEAPTMS-treated perovskite films, the evolution in GIWAXS patterns was less dramatic (Fig. 2A and the supplementary movies 3 and 4). The relative intensity ratio of perovskite rings remained consistent throughout the entire AEAPTMS treatment and there was no evidence of discrete larger d-spacing phases emerging. This result indicated that the isotropic orientation of the bulk perovskite was maintained before and after the AEAPTMS treatment. The absolute intensities of all of the perovskite peaks did become weaker with time, and a pair of broad, amorphous rings appeared in the low Q-space, which we interpreted to belong to the organic molecules of AEAPTMS. This result indicates that during this in-situ treatment, AEAPTMS molecules coated and accumulated onto the surface of the perovskite film with a long-processing time (~ 30 min, the supplementary movies 3 and 4), which might have screened the x-ray scattering from the underlying perovskite film.

To verify if the different passivation treatments were located upon the film surface or penetrating throughout the bulk of the films, we further examined the films using time-of-flight secondary ion mass spectrometry (ToF-SIMS), looking at the elemental depth profile. Although APTMS (fig. S16A) and MAPTMS (fig. S16B) both exhibited varying degrees of Si signal penetration throughout the films, The Si signal for perovskite films treated with AEAPTMS molecules remained predominantly within the surface region of the perovskite layer (fig. S16C). This observation held even when the treatment duration was tripled (fig. S16D).

The structures and interactions of the amino-silane molecules at perovskite surfaces were, however, not fully understood at the atomic level. To gain further insights into such properties, we have used density functional theory (DFT) and ab-initio molecular dynamics (AIMD) methods to investigate four types of silane molecules covering different possible amine positions: primary (APTMS), secondary (MAPTMS), both primary and secondary (AEAPTMS), as well in the absence of an amino group (PTMS) (see the supplementary text). Their interactions on the pristine perovskite surface and on surfaces with an iodide vacancy defect were examined. Iodide vacancy defects play highly detrimental roles in affecting the operational efficiency and stability of perovskite solar cells, including facilitating ion migration to surfaces (*40-42*) and non-radiative photocarrier recombination (*43, 44*). To investigate key adsorption and structural trends for the range of amino-silanes on FA-based, MA-free perovskite triiodides, we examined the (001) PbI_2 terminated pristine $FAPbI_3$ surface, because it is one of the most stable and studied halide perovskite surfaces (*45, 46*). We provided computational details in the supplementary materials.

Figure 2, B and C, show the optimized structures and calculated binding energies of the amino-silane molecules (Fig. 2D) on the pristine surface and on the iodide vacancy defect surface. Three important features emerged. First, favorable binding energies showed strong bonding affinity between the molecules and the surface, with the highest and lowest binding energies found for AEAPTMS and PTMS, respectively; however, only for AEAPTMS did the surface binding energy increase substantially from the pristine surface to the iodide vacancy defect surface. Second, the strongest adsorption for AEAPTMS suggested the role of larger amino-silane molecules having both primary and secondary amine groups in providing effective surface defect passivation. As surface Pb ions adjacent to an iodide vacancy were severely undercoordinated (with four-fold coordination versus octahedral in the bulk of perovskites), the strong passivator adsorption of AEAPTMS increased the coordination around these Pb ions and eliminated the effects of surface vacancy defects (Fig. 2E and fig. S17). Third, noting the speculation around the precise atomistic interactions of the amino-silane molecules at the perovskite surfaces (*18*), our simulations revealed that the terminal amines in AEAPTMS bind to the surface Pb atoms with an N-Pb bond length of

2.51 Å, versus the longer Pb-I bond length of 3.15 Å. The schematic (Fig. 2E) shows that the AEAPTMS molecule bridged the two Pb ions adjacent to the iodide vacancy via N-Pb bonds.

In addition to speculation around N-Pb interactions from previous work (*18*), we also observed O-Pb bonding with an average bond length of 2.80 Å. Changes in the charge density profile around all of the species (Fig. 2C) showed silane-surface charge transfer around the surface Pb cations, again indicating O-Pb and N-Pb chemical bonds. Such multidentate interactions increased the binding or anchoring strength on the surface and enhanced the effective passivation. Overall, these ab-initio simulation results also agreed with our experimental findings and provide new structural and mechanistic insights at the atomic level.

Photovoltaic cell operational performance and stability

We fabricated and measured a series of solar cells (fig. S18; the designs of our cell layouts shown in fig. S19) to screen all of the amino-silane molecules of interest (Fig. 1A). The amino-silane molecule, AEAPTMS, appeared to result in the largest improvement in PV performance parameters for the $Cs_{13}Br_{10}$-based perovskite. Cells treated with $(AE)_2APTMS$ also exhibited enhanced PV performance, but in many cases, we found $(AE)_2APTMS$-treated cells showed lower short-circuit current density J_{SC} and fill factor FF, and hence a lower PCE as compared to AEAPTMS-treated cells, and required a very narrow processing window, i.e., < 10 seconds, for the vapor treatment process (Fig. 1C).

We next focused upon the AEAPTMS treatment. To illustrate its influence, we present representative J-V characteristics of reference and AEAPTMS-treated cells using $Cs_{13}Br_{10}$, $Cs_{17}Br_{23}$, and $Cs_{15}Br_{40}$ in Fig. 3, A, B and C, respectively. These cells, with an optically masked aperture of 0.25 cm^2, exhibited the corresponding PV parameters of an open-circuit voltage V_{OC} = 1.22, 1.26, and 1.35 V, J_{SC} = 22.3, 19.5, and 17.2 mA cm^{-2}, FF = 83.4, 84.0, and 80.9%, and PCE = 22.6, 20.6, and 18.7%, respectively, for the scanning direction from forward-bias to short-circuit (FB-SC) conditions. Figures S20, S21, and S22 show the corresponding external quantum efficiency (EQE) and 120-s MPPT with MPP efficiency of 22.4, 20.7, and 18.6% for $Cs_{13}Br_{10}$, $Cs_{17}Br_{23}$, and $Cs_{15}Br_{40}$-based cells, respectively.

The EQE analysis revealed that the integrated J_{SC} exhibited a negligible variation (< 1%) compared to the J_{SC} measured from the corresponding cells under simulated sunlight, as shown in the insets of Fig. 3, A to C. The EQE-derived PV bandgaps (*31*) are 1.60, 1.67, and 1.77 eV for $Cs_{13}Br_{10}$, $Cs_{17}Br_{23}$, and $Cs_{15}Br_{40}$, respectively, with the statistical results for V_{OC}, J_{SC}, FF, and PCE shown in figs. S23, S24, S25, and S26, respectively. Of particular note is that V_{OC} could reach as high as 1.28 and 1.38 V for wide bandgap 1.67 and 1.77-eV perovskites (i.e., $Cs_{17}Br_{23}$ and $Cs_{15}Br_{40}$), respectively. Such high photovoltages from mixed-cation, mixed-anion perovskite cells are crucial for the development of next-generation perovskite-based tandem PV cells. Because multi-junction perovskite-on-silicon and all-perovskite tandem cells usually use thermally evaporated C_{60} as an ETL, to demonstrate the compatibility of our passivation treatment, we fabricated $Cs_{17}Br_{23}$ with an evaporated C_{60} and BCP ETL stack and obtained an enhancement of V_{OC} from 1.21 V for the $Cs_{17}Br_{23}$ reference cell to 1.26 V for the AEAPTMS-treated $Cs_{17}Br_{23}$ cells. This result confirmed the suitability of our approach for use in tandem cells (fig. S27).

We then proceeded to fabricate 1-cm^2 cells, and the corresponding J-V characteristics, MPPT, and EQE are shown in Fig. 3, D and E, and fig. S28, respectively. The enhancement obtained in the PV parameters for these 1-cm^2 cells (the supplementary table S2) was similar to that seen in 0.25-

cm^2 small-area cells with a minimum performance deficit when enlarging the cell area. Our 1-cm^2 cell device data suggested that this vapor-based passivation approach could result in a highly uniform passivation effect. Furthermore, we estimated the thermodynamic detailed balance V_{OC} limits for the perovskite absorbers of different bandgaps and compared them to the values we obtained from our devices and the literature (fig. S29). The AEAPTMS molecule could universally boost V_{OC} to > 90% of the thermodynamic limit (*31*) and result in outstanding performance when adopting PV cell sizes of a medium area of 0.25 cm^2 and a large area of 1 cm^2. Therefore, the photovoltages obtained from perovskite PV cells treated with AEAPTMS are approaching what has previously only been attainable from those made of single-crystal epitaxially grown III-V semiconductors (fig. S29) (*31*).

Building on this success, we further explored whether AEAPTMS could bring any additional benefits, such as inhibiting halide segregation, which often occurs in wide bandgap mixed halide perovskites during operation. We used a 1-cm^2 $Cs_{15}Br_{40}$-based solar cell (fig. S30, A and B) and applied a voltage sweep from 0 to 4 V to the cell while measuring the electroluminescence (Fig. 3F, fig. S30C, and the supplementary movie S6). We obtained a peak electroluminescence quantum efficiency (EQE_{EL}) of 3.2% at an injection current density ~ 820 mA cm^{-2} (Fig. 3F), which corresponded to exposure to illumination at the intensity of ~ 40 suns (based on the detailed balance limit derived 1-sun J_{SC}, which is ~ 20.5 mA cm^{-2}) and leads to a QFLS of ~ 1.49 eV for a solar cell of a 1.77-eV bandgap under these high injection conditions. An EQE_{EL} of 3.2% under 1-sun irradiance would lead to a QFLS of ~ 1.40 eV (*31*). However, under a forward bias injection current density near 1-sun J_{SC} (~ 17.5 mA cm^{-2}), we determined an EQE_{EL} of ~ 0.4%, which corresponded to a QFLS of ~ 1.35 eV. This value is in close agreement with the V_{OC} obtained for AEAPTMS-treated $Cs_{15}Br_{40}$-based cells (fig. S23). Very encouragingly, the output spectrum of our cell could remain constant in both intensity and wavelength for 10 min at a charge injection current density of 17 mA cm^{-2} (as shown in the inset of Fig. 3F and fig. S30D). This result matches the bandgap stability and surpasses the absolute irradiance stability of a reported state-of-the-art perovskite red-light emitting diode, which used well-passivated perovskite nanocrystals (*15*).

Next, we investigated how AEAPTMS impacted a solar cell's long-term operational stability. We aged encapsulated reference and AEAPTMS-treated $Cs_{13}Br_{10}$ solar cells by exposing them to full-spectrum simulated sunlight in a xenon lamp aging box at 85 °C under an open-circuit condition in ambient air with a relative humidity in the laboratory of 50 to 60%, resembling an aging condition close to the ISOS-L-3 protocol (ISOS: International Summit on Organic Photovoltaic Stability) (*21, 47, 48*). The devices were periodically taken out of the aging chamber, allowed to cool to room temperature and characterized under 1-sun simulated sunlight at various time intervals.

The mean MPP tracked efficiency, conducted "ex-situ" at specified aging times as described above, and J-V derived PCE of the aged cells, along with their standard deviations, are plotted in Fig. 4A and fig. S31A, respectively. The evolution of the corresponding PV performance parameters, V_{OC}, J_{SC}, and FF are shown in figs. S32, S33, and S34, respectively, and the evolution of the MPP efficiency and PCE of each individual cell recorded is plotted in Fig. 4B and fig. S31B, respectively. Representative J-V curves, captured at various aging times, are presented in fig. S35. Our AEAPTMS-treated cells demonstrated substantial operational stability during the aging process. The MPP efficiency and PCE of the champion cell decreased to 95% of their initial values (i.e., $T_{95,\,Champ}$) after ~ 1,600 and 1,440 hours, respectively. At $T_{95,\,Champ}$, the MPP efficiency was

recorded at 19.4% (Fig. 4B), and the PCE was 20.1% (fig. S31B). These performance metrics indicate exceptional stability for perovskite solar cells (*21*, *48*).

If we assume a linear degradation model (*47*), our stability results, represent an order of magnitude enhancement in longevity compared to our previously reported best stability under identical aging conditions, where we reported a champion T_{80} lifetime (time to reach 80% of the peak performance) of 490 hours (*49*). Current state-of-the-art stable perovskite solar cells predominantly adopt a narrower bandgap perovskite adsorber, i.e., $FAPbI_3$ (*4*, *9*, *21*, *23*, *48*, *50*, *51*). However, comparing the stability of mixed-cation, mixed-halide perovskite solar cells with $FAPbI_3$ like perovskites is not straightforward because of inherent differences in degradation pathways (*52*). Nonetheless, our results show a notable advancement in stability when benchmarking against a range of reported compositions. Our mixed-cation, mixed-halide perovskite solar cells rank among the best in terms of operational longevity and demonstrated some of the most promising outcomes reported to date (table S3), especially given rigorous ISOS-L-3 protocol we employed (*47*) that includes full-spectrum simulated sunlight at an open-circuit condition (*53*). Importantly, only a few studies have used a light source that replicates the full spectrum of sunlight for stability testing (table S3).

After establishing the enhanced operational stability of AEAPTMS-treated cells, as evidenced by their prolonged efficiency retention under stringent aging conditions discussed above, we further examined their resilience to environmental stressors. One such stressor is water ingression (*54*). As presented in the supplementary movie S7, soon after we dropped a water droplet onto the $Cs_{13}Br_{10}$ films, we observed a stark contrast between the AEAPTMS-treated and reference perovskite films: the reference immediately turned yellow, indicating rapid hydration and disintegration of perovskite crystalline structures, whereas the AEAPTMS-treated thin perovskite films demonstrated remarkable resistance, lasting > 20 s before showing any signs of partial discoloration.

However, we still observed that, even when using a cover glass slip for encapsulation with epoxy resin edge sealing (as shown in fig. S36, A and B), we required a capping layer of CYTOP (an amorphous fluoropolymer) to coat the completed devices to obtain the best stability results. In the absence of an "on-cell capping layer," cell areas underwent discoloration (fig. S36C). Because the cells were encapsulated in an N_2-filled glove box, we assumed that this discoloration was caused by the loss of iodine during photoinduced degradation, which would leave voids in the film and react with the metallic electrodes (*52*, *55*). However, when comparing the EQE spectra measured from those aged cells (fig. S37), we did not observe a substantial change in the EQE onset energy. This finding suggested that insignificant or negligible compositional change occurred during aging. However, the reference cells suffered from more severe panchromatic deterioration in EQE than the AEAPTMS-treated cells, consistent with the more severe drop in J_{SC}. Notably, the dips in the EQE spectra appeared to result from some intermittent electronic failure of the device, such as sporadic "internal shunting" in the aged devices, manifesting as fluctuating impacts on the EQE at different wavelengths in each measurement (fig. S38).

Given the observed variations in cell performance during aging (Fig. 4, A and B, and fig. S31), we conducted PL imaging of cells to elucidate how the AEAPTMS passivation enhanced long-term stability (*56*). We present the PL-derived QFLS images (see the supplementary text) of the representative full-area 0.25-cm^2 AEAPTMS-based and reference cells at different aging stages in Fig. 4, C and D, and fig. S39. Intriguingly, even the reference cell maintained relatively high and stable QFLS maps, comparable to its initial state, for up to 300 hours. This stability was evidenced

by only 2.8% relative decay in the QFLS median (from 1.16 eV to 1.13 eV, Fig. 4G), as shown in the corresponding QFLS maps of the reference cells (fig. S39B).

Yet, after 600 hours of aging, distinguishable regions of lower and higher QFLS appeared in the maps (Fig. 4D and fig. S39B), indicating that the reference cells degraded heterogeneously on the 100 micrometer to millimeter length-scale. QFLS of the complete device, should closely correlate with V_{OC}. However, as we show in Fig. 4G and fig. S32, as the reference perovskite cells aged, the difference between QFLS and V_{OC} became progressively larger and reached ~ 380 mV by the end of the ageing process. This result indicates that either (i) an energetic shift occurred at either one or both charge selective contacts, or (ii) the selectivity for electrons or holes of one of the contacts was reduced. For the reference cell, in addition to loss in V_{OC}, there were also appreciable losses in the other PV performance parameters (figs. S33 and S34).

Therefore, the QFLS images suggest that the perovskite absorber could remain relatively intact when subjected to rigorous 85 ℃ light soaking ageing conditions, whereas other parts of the cell may have undergone severe deterioration. Especially, during aging of the reference devices, substantial decay in all the PV parameters, as exemplified in figs. S32, S33, and S34, with the J-V curves shown in fig. S35, suggests a range of detrimental effects, such as poor charge extraction, elevated series resistance, and degraded contact properties. The AEAPTMS-treated cells, on the other hand, exhibited even less deterioration in QFLS and remained homogeneous throughout aging. Specifically, whereas the QFLS median was initially 1.23 eV at 0 hours, this value only dropped from 1.19 eV at 300 hours and to 1.17 eV at 1,200 hours (Fig. 4, C and G, and fig. S39A).

The QFLS maps did not appear to directly correlate with the sequence of degradation levels in cells (Fig. 4G). As a result, we turned to an alternative metric – the luminescence-derived "charge collection quality" (Q_{col}, see the supplementary text) – which should qualitatively scale with a cell's J_{SC} (*56*). Here, we determined the fraction of the PL, which is quenched at short-circuit, as compared to open-circuit, and assume that all of the quenched PL at short-circuit resulted from charge extraction. Figure 4, E and F, shows the Q_{col} maps for the fresh and 600-hour aged devices, and in fig. S40, we present our complete dataset of Q_{col} throughout the aging process. Consistent with the macroscopic device J-V measurements, the reference cell showed a substantial reduction in Q_{col} after aging (Fig. 4F). The median dropped from 0.96 in its initial state to 0.42 after aging for 600 hours (see Fig. 4H), indicating a decay of > 56%. Notably, the regions of lower Q_{col} mostly correlated with the same regions of lower QFLS. Interestingly, even for the reference cells, quite large regions of high Q_{col} remained after aging for 300 hours (fig. S40B), indicating the degradation originated from certain defective areas rather than being homogeneous across the entire device (Fig. 4F and fig. S40B). In contrast, the AEAPTMS-treated cells exhibited an even higher initial median Q_{col} (0.99, Fig. 4H), which only dropped to 0.91 (see Fig. 4H) and remained relatively homogeneous after 1,200 hours of aging (Fig. 4E and fig. S40A).

We note that although our most stable devices exhibited an approximately linear decay during our stress testing, for both the reference and AEAPTMS-treated devices, we observed that some cells experienced positive light-soaking (i.e., performance gain) or burn-in (i.e., early decay) during ageing (Fig. 4B and fig. S31B). However, the origin of these differences is not clear and beyond the scope of the current work.

Discussion

Our findings have demonstrated that amino-silane molecules, with varying primary-, secondary-, and tertiary-amine functional groups, significantly impact the PLQY, crystalline order, and charge-carrier mobility of metal halide perovskites. In our study, AEAPTMS emerges as an exceptional surface passivator, establishing a strong bonding affinity with the perovskite surface. Notably, the AEAPTMS treatment substantially elevates the PLQY of perovskites with bandgaps ranging from 1.6 to 1.8 eV, propelling their radiative performance closer to the theoretical thermodynamic limits. More importantly, AEAPTMS-treated perovskite solar cells exhibit state-of-the-art long-term stability under strenuous elevated temperature light-soaking aging conditions, highlighting the potential of our passivation strategy in advancing highly durable and efficient perovskite PV technologies.

References and Notes

1. R. E. Brandt, J. R. Poindexter, P. Gorai, R. C. Kurchin, R. L. Z. Hoye, L. Nienhaus, M. W. B. Wilson, J. A. Polizzotti, R. Sereika, R. Žaltauskas, L. C. Lee, J. L. MacManus-Driscoll, M. Bawendi, V. Stevanović, T. Buonassisi, Searching for "Defect-Tolerant" Photovoltaic Materials: Combined Theoretical and Experimental Screening. *Chem. Mater.* **29**, 4667-4674 (2017).
2. Y. Zhou, I. Poli, D. Meggiolaro, F. De Angelis, A. Petrozza, Defect activity in metal halide perovskites with wide and narrow bandgap. *Nat. Rev. Mater.*, (2021).
3. S. Yu, Z. Xiong, H. Zhou, Q. Zhang, Z. Wang, F. Ma, Z. Qu, Y. Zhao, X. Chu, X. Zhang, J. You, Homogenized NiO(x) nanoparticles for improved hole transport in inverted perovskite solar cells. *Science* **0**, eadj8858 (2023).
4. S. M. Park, M. Wei, N. Lempesis, W. Yu, T. Hossain, L. Agosta, V. Carnevali, H. R. Atapattu, P. Serles, F. T. Eickemeyer, H. Shin, M. Vafaie, D. Choi, K. Darabi, E. D. Jung, Y. Yang, D. B. Kim, S. M. Zakeeruddin, B. Chen, A. Amassian, T. Filleter, M. G. Kanatzidis, K. R. Graham, L. Xiao, U. Rothlisberger, M. Grätzel, E. H. Sargent, Low-loss contacts on textured substrates for inverted perovskite solar cells. *Nature*, (2023).
5. N. K. Noel, A. Abate, S. D. Stranks, E. S. Parrott, V. M. Burlakov, A. Goriely, H. J. Snaith, Enhanced Photoluminescence and Solar Cell Performance via Lewis Base Passivation of Organic–Inorganic Lead Halide Perovskites. *ACS Nano* **8**, 9815-9821 (2014).
6. Q. Jiang, Y. Zhao, X. Zhang, X. Yang, Y. Chen, Z. Chu, Q. Ye, X. Li, Z. Yin, J. You, Surface passivation of perovskite film for efficient solar cells. *Nat. Photon.* **13**, 460-466 (2019).
7. J. Park, J. Kim, H. S. Yun, M. J. Paik, E. Noh, H. J. Mun, M. G. Kim, T. J. Shin, S. I. Seok, Controlled growth of perovskite layers with volatile alkylammonium chlorides. *Nature* **616**, 724-730 (2023).
8. H. Tsai, W. Nie, J.-C. Blancon, C. C. Stoumpos, R. Asadpour, B. Harutyunyan, A. J. Neukirch, R. Verduzco, J. J. Crochet, S. Tretiak, L. Pedesseau, J. Even, M. A. Alam, G. Gupta, J. Lou, P. M. Ajayan, M. J. Bedzyk, M. G. Kanatzidis, A. D. Mohite, High-efficiency two-dimensional Ruddlesden–Popper perovskite solar cells. *Nature* **536**, 312-316 (2016).
9. S. M. Park, M. Wei, J. Xu, H. R. Atapattu, F. T. Eickemeyer, K. Darabi, L. Grater, Y. Yang, C. Liu, S. Teale, B. Chen, H. Chen, T. Wang, L. Zeng, A. Maxwell, Z. Wang, K. R. Rao, Z. Cai, S. M. Zakeeruddin, J. T. Pham, C. M. Risko, A. Amassian, M. G. Kanatzidis,

K. R. Graham, M. Grätzel, E. H. Sargent, Engineering ligand reactivity enables high-temperature operation of stable perovskite solar cells. *Science* **381**, 209-215 (2023).
10. B. Guo, R. Lai, S. Jiang, L. Zhou, Z. Ren, Y. Lian, P. Li, X. Cao, S. Xing, Y. Wang, W. Li, C. Zou, M. Chen, Z. Hong, C. Li, B. Zhao, D. Di, Ultrastable near-infrared perovskite light-emitting diodes. *Nat. Photon.*, (2022).
11. Y. Yuan, G. Yan, C. Dreessen, T. Rudolph, M. Hülsbeck, B. Klingebiel, J. Ye, U. Rau, T. Kirchartz, Shallow defects and variable photoluminescence decay times up to 280 µs in triple-cation perovskites. *Nat. Mater.*, (2024).
12. R. J. E. Westbrook, T. J. Macdonald, W. Xu, L. Lanzetta, J. M. Marin-Beloqui, T. M. Clarke, S. A. Haque, Lewis Base Passivation Mediates Charge Transfer at Perovskite Heterojunctions. *J. Am. Chem. Soc.* **143**, 12230-12243 (2021).
13. S. You, H. Zeng, Y. Liu, B. Han, M. Li, L. Li, X. Zheng, R. Guo, L. Luo, Z. Li, C. Zhang, R. Liu, Y. Zhao, S. Zhang, Q. Peng, T. Wang, Q. Chen, F. T. Eickemeyer, B. Carlsen, S. M. Zakeeruddin, L. Mai, Y. Rong, M. Grätzel, X. Li, Radical polymeric p-doping and grain modulation for stable, efficient perovskite solar modules. *Science* **379**, 288-294 (2023).
14. L. Wu, Q. Zhong, D. Yang, M. Chen, H. Hu, Q. Pan, H. Liu, M. Cao, Y. Xu, B. Sun, Q. Zhang, Improving the Stability and Size Tunability of Cesium Lead Halide Perovskite Nanocrystals Using Trioctylphosphine Oxide as the Capping Ligand. *Langmuir* **33**, 12689-12696 (2017).
15. Y. Hassan, J. H. Park, M. L. Crawford, A. Sadhanala, J. Lee, J. C. Sadighian, E. Mosconi, R. Shivanna, E. Radicchi, M. Jeong, C. Yang, H. Choi, S. H. Park, M. H. Song, F. De Angelis, C. Y. Wong, R. H. Friend, B. R. Lee, H. J. Snaith, Ligand-engineered bandgap stability in mixed-halide perovskite LEDs. *Nature* **591**, 72-77 (2021).
16. I. L. Braly, D. W. deQuilettes, L. M. Pazos-Outón, S. Burke, M. E. Ziffer, D. S. Ginger, H. W. Hillhouse, Hybrid perovskite films approaching the radiative limit with over 90% photoluminescence quantum efficiency. *Nat. Photon.*, (2018).
17. Z. Iqbal, F. Zu, A. Musiienko, E. Gutierrez-Partida, H. Köbler, T. W. Gries, G. V. Sannino, L. Canil, N. Koch, M. Stolterfoht, D. Neher, M. Pavone, A. B. Muñoz-García, A. Abate, Q. Wang, Interface Modification for Energy Level Alignment and Charge Extraction in CsPbI3 Perovskite Solar Cells. *ACS Energy Lett.* **8**, 4304-4314 (2023).
18. S. Jariwala, S. Burke, S. Dunfield, R. C. Shallcross, M. Taddei, J. Wang, G. E. Eperon, N. R. Armstrong, J. J. Berry, D. S. Ginger, Reducing Surface Recombination Velocity of Methylammonium-Free Mixed-Cation Mixed-Halide Perovskites via Surface Passivation. *Chem. Mater.* **33**, 5035-5044 (2021).
19. J. Pothoof, R. J. E. Westbrook, R. Giridharagopal, M. D. Breshears, D. S. Ginger, Surface Passivation Suppresses Local Ion Motion in Halide Perovskites. *J. Phys. Chem. Lett.* **14**, 6092-6098 (2023).
20. Y. Shi, E. Rojas-Gatjens, J. Wang, J. Pothoof, R. Giridharagopal, K. Ho, F. Jiang, M. Taddei, Z. Yang, E. M. Sanehira, M. D. Irwin, C. Silva-Acuña, D. S. Ginger, (3-Aminopropyl)trimethoxysilane Surface Passivation Improves Perovskite Solar Cell Performance by Reducing Surface Recombination Velocity. *ACS Energy Lett.* **7**, 4081-4088 (2022).
21. C. Li, X. Wang, E. Bi, F. Jiang, S. M. Park, Y. Li, L. Chen, Z. Wang, L. Zeng, H. Chen, Y. Liu, C. R. Grice, A. Abudulimu, J. Chung, Y. Xian, T. Zhu, H. Lai, B. Chen, R. J. Ellingson, F. Fu, D. S. Ginger, Z. Song, E. H. Sargent, Y. Yan, Rational design of Lewis

base molecules for stable and efficient inverted perovskite solar cells. *Science* **379**, 690-694 (2023).
22. A. J. Ramadan, R. D. J. Oliver, M. B. Johnston, H. J. Snaith, Methylammonium-free wide-bandgap metal halide perovskites for tandem photovoltaics. *Nat. Rev. Mater.* **8**, 822-838 (2023).
23. C. Liu, Y. Yang, H. Chen, J. Xu, A. Liu, A. S. R. Bati, H. Zhu, L. Grater, S. S. Hadke, C. Huang, V. K. Sangwan, T. Cai, D. Shin, L. X. Chen, M. C. Hersam, C. A. Mirkin, B. Chen, M. G. Kanatzidis, E. H. Sargent, Bimolecularly passivated interface enables efficient and stable inverted perovskite solar cells. *Science* **382**, 810-815 (2023).
24. Q. Jiang, J. Tong, Y. Xian, R. A. Kerner, S. P. Dunfield, C. Xiao, R. A. Scheidt, D. Kuciauskas, X. Wang, M. P. Hautzinger, R. Tirawat, M. C. Beard, D. P. Fenning, J. J. Berry, B. W. Larson, Y. Yan, K. Zhu, Surface reaction for efficient and stable inverted perovskite solar cells. *Nature* **611**, 278-283 (2022).
25. Z. Wang, L. Zeng, T. Zhu, H. Chen, B. Chen, D. J. Kubicki, A. Balvanz, C. Li, A. Maxwell, E. Ugur, R. Dos Reis, M. Cheng, G. Yang, B. Subedi, D. Luo, J. Hu, J. Wang, S. Teale, S. Mahesh, S. Wang, S. Hu, E. D. Jung, M. Wei, S. M. Park, L. Grater, E. Aydin, Z. Song, N. J. Podraza, Z. H. Lu, J. Huang, V. P. Dravid, S. De Wolf, Y. Yan, M. Gratzel, M. G. Kanatzidis, E. H. Sargent, Suppressed phase segregation for triple-junction perovskite solar cells. *Nature* **618**, 74-79 (2023).
26. Y. H. Lin, H. Faber, S. Rossbauer, T. D. Anthopoulos, Solution-processed ZnO nanoparticle-based transistors via a room-temperature photochemical conversion process. *Appl. Phys. Lett.* **102**, 193516 (2013).
27. R. D. J. Oliver, P. Caprioglio, F. Peña-Camargo, L. R. V. Buizza, F. Zu, A. J. Ramadan, S. G. Motti, S. Mahesh, M. M. McCarthy, J. H. Warby, Y.-H. Lin, N. Koch, S. Albrecht, L. M. Herz, M. B. Johnston, D. Neher, M. Stolterfoht, H. J. Snaith, Understanding and suppressing non-radiative losses in methylammonium-free wide-bandgap perovskite solar cells. *Energy Environ. Sci.* **15**, 714-726 (2022).
28. R. Lin, Y. Wang, Q. Lu, B. Tang, J. Li, H. Gao, Y. Gao, H. Li, C. Ding, J. Wen, P. Wu, C. Liu, S. Zhao, K. Xiao, Z. Liu, C. Ma, Y. Deng, L. Li, F. Fan, H. Tan, All-perovskite tandem solar cells with 3D/3D bilayer perovskite heterojunction. *Nature* **620**, 994-1000 (2023).
29. S. Zhou, S. Fu, C. Wang, W. Meng, J. Zhou, Y. Zou, Q. Lin, L. Huang, W. Zhang, G. Zeng, D. Pu, H. Guan, C. Wang, K. Dong, H. Cui, S. Wang, T. Wang, G. Fang, W. Ke, Aspartate all-in-one doping strategy enables efficient all-perovskite tandems. *Nature* **624**, 69-73 (2023).
30. R. He, W. Wang, Z. Yi, F. Lang, C. Chen, J. Luo, J. Zhu, J. Thiesbrummel, S. Shah, K. Wei, Y. Luo, C. Wang, H. Lai, H. Huang, J. Zhou, B. Zou, X. Yin, S. Ren, X. Hao, L. Wu, J. Zhang, J. Zhang, M. Stolterfoht, F. Fu, W. Tang, D. Zhao, All-perovskite tandem 1 cm2 cells with improved interface quality. *Nature*, (2023).
31. P. K. Nayak, S. Mahesh, H. J. Snaith, D. Cahen, Photovoltaic solar cell technologies: analysing the state of the art. *Nat. Rev. Mater.* **4**, 269-285 (2019).
32. P. Caprioglio, J. A. Smith, R. D. J. Oliver, A. Dasgupta, S. Choudhary, M. D. Farrar, A. J. Ramadan, Y.-H. Lin, M. G. Christoforo, J. M. Ball, J. Diekmann, J. Thiesbrummel, K.-A. Zaininger, X. Shen, M. B. Johnston, D. Neher, M. Stolterfoht, H. J. Snaith, Open-circuit and short-circuit loss management in wide-gap perovskite p-i-n solar cells. *Nat. Commun.* **14**, 932 (2023).

33. L. M. Herz, Charge-Carrier Mobilities in Metal Halide Perovskites: Fundamental Mechanisms and Limits. *ACS Energy Lett.* **2**, 1539-1548 (2017).
34. S. Jariwala, H. Sun, G. W. P. Adhyaksa, A. Lof, L. A. Muscarella, B. Ehrler, E. C. Garnett, D. S. Ginger, Local Crystal Misorientation Influences Non-radiative Recombination in Halide Perovskites. *Joule* **3**, 3048-3060 (2019).
35. L. Zhao, P. Tang, D. Luo, M. I. Dar, F. T. Eickemeyer, N. Arora, Q. Hu, J. Luo, Y. Liu, S. M. Zakeeruddin, A. Hagfeldt, J. Arbiol, W. Huang, Q. Gong, T. P. Russell, R. H. Friend, M. Grätzel, R. Zhu, Enabling full-scale grain boundary mitigation in polycrystalline perovskite solids. *Sci. Adv.* **8**, eabo3733 (2022).
36. A. J. Knight, J. Borchert, R. D. J. Oliver, J. B. Patel, P. G. Radaelli, H. J. Snaith, M. B. Johnston, L. M. Herz, Halide Segregation in Mixed-Halide Perovskites: Influence of A-Site Cations. *ACS Energy Lett.* **6**, 799-808 (2021).
37. S. G. Motti, F. Krieg, A. J. Ramadan, J. B. Patel, H. J. Snaith, M. V. Kovalenko, M. B. Johnston, L. M. Herz, CsPbBr3 Nanocrystal Films: Deviations from Bulk Vibrational and Optoelectronic Properties. *Adv. Funct. Mater.* **30**, 1909904 (2020).
38. N. K. Noel, S. N. Habisreutinger, B. Wenger, M. T. Klug, M. T. Hörantner, M. B. Johnston, R. J. Nicholas, D. T. Moore, H. J. Snaith, A low viscosity, low boiling point, clean solvent system for the rapid crystallisation of highly specular perovskite films. *Energy Environ. Sci.* **10**, 145-152 (2017).
39. Z. Zhou, Z. Wang, Y. Zhou, S. Pang, D. Wang, H. Xu, Z. Liu, N. P. Padture, G. Cui, Methylamine-Gas-Induced Defect-Healing Behavior of CH3NH3PbI3 Thin Films for Perovskite Solar Cells. *Angew. Chem. Int. Ed.* **54**, 9705-9709 (2015).
40. C. Eames, J. M. Frost, P. R. F. Barnes, B. C. O'Regan, A. Walsh, M. S. Islam, Ionic transport in hybrid lead iodide perovskite solar cells. *Nat. Commun.* **6**, 7497 (2015).
41. J. M. Azpiroz, E. Mosconi, J. Bisquert, F. De Angelis, Defect migration in methylammonium lead iodide and its role in perovskite solar cell operation. *Energy Environ. Sci.* **8**, 2118-2127 (2015).
42. D. Ghosh, A. Aziz, J. A. Dawson, A. B. Walker, M. S. Islam, Putting the Squeeze on Lead Iodide Perovskites: Pressure-Induced Effects To Tune Their Structural and Optoelectronic Behavior. *Chem. Mater.* **31**, 4063-4071 (2019).
43. J. M. Ball, A. Petrozza, Defects in perovskite-halides and their effects in solar cells. *Nat. Energy* **1**, 16149 (2016).
44. M. B. Johnston, L. M. Herz, Hybrid Perovskites for Photovoltaics: Charge-Carrier Recombination, Diffusion, and Radiative Efficiencies. *Acc. Chem. Res.* **49**, 146-154 (2016).
45. J. Xue, R. Wang, Y. Yang, The surface of halide perovskites from nano to bulk. *Nat. Rev. Mater.* **5**, 809-827 (2020).
46. C. Ma, F. T. Eickemeyer, S.-H. Lee, D.-H. Kang, S. J. Kwon, M. Grätzel, N.-G. Park, Unveiling facet-dependent degradation and facet engineering for stable perovskite solar cells. *Science* **379**, 173-178 (2023).
47. M. V. Khenkin, E. A. Katz, A. Abate, G. Bardizza, J. J. Berry, C. Brabec, F. Brunetti, V. Bulović, Q. Burlingame, A. Di Carlo, R. Cheacharoen, Y.-B. Cheng, A. Colsmann, S. Cros, K. Domanski, M. Dusza, C. J. Fell, S. R. Forrest, Y. Galagan, D. Di Girolamo, M. Grätzel, A. Hagfeldt, E. von Hauff, H. Hoppe, J. Kettle, H. Köbler, M. S. Leite, S. Liu, Y.-L. Loo, J. M. Luther, C.-Q. Ma, M. Madsen, M. Manceau, M. Matheron, M. McGehee, R. Meitzner, M. K. Nazeeruddin, A. F. Nogueira, Ç. Odabaşı, A. Osherov, N.-G. Park, M. O. Reese, F. De Rossi, M. Saliba, U. S. Schubert, H. J. Snaith, S. D. Stranks, W. Tress, P. A. Troshin, V.

Turkovic, S. Veenstra, I. Visoly-Fisher, A. Walsh, T. Watson, H. Xie, R. Yıldırım, S. M. Zakeeruddin, K. Zhu, M. Lira-Cantu, Consensus statement for stability assessment and reporting for perovskite photovoltaics based on ISOS procedures. *Nat. Energy* **5**, 35-49 (2020).

48. H. Chen, S. Teale, B. Chen, Y. Hou, L. Grater, T. Zhu, K. Bertens, S. M. Park, H. R. Atapattu, Y. J. Gao, M. Y. Wei, A. K. Johnston, Q. L. Zhou, K. M. Xu, D. N. Yu, C. C. Han, T. Cui, E. H. Jung, C. Zhou, W. J. Zhou, A. H. Proppe, S. Hoogland, F. Laquai, T. Filleter, K. R. Graham, Z. J. Ning, E. H. Sargent, Quantum-size-tuned heterostructures enable efficient and stable inverted perovskite solar cells. *Nat. Photon.* **16**, 352-358 (2022).
49. D. P. McMeekin, P. Holzhey, S. O. Furer, S. P. Harvey, L. T. Schelhas, J. M. Ball, S. Mahesh, S. Seo, N. Hawkins, J. Lu, M. B. Johnston, J. J. Berry, U. Bach, H. J. Snaith, Intermediate-phase engineering via dimethylammonium cation additive for stable perovskite solar cells. *Nat. Mater.* **22**, 73-83 (2023).
50. M. Wang, Z. Shi, C. Fei, Z. J. D. Deng, G. Yang, S. P. Dunfield, D. P. Fenning, J. Huang, Ammonium cations with high pKa in perovskite solar cells for improved high-temperature photostability. *Nat. Energy* **8**, 1229-1239 (2023).
51. P. Shi, Y. Ding, B. Ding, Q. Xing, T. Kodalle, C. M. Sutter-Fella, I. Yavuz, C. Yao, W. Fan, J. Xu, Y. Tian, D. Gu, K. Zhao, S. Tan, X. Zhang, L. Yao, P. J. Dyson, J. L. Slack, D. Yang, J. Xue, M. K. Nazeeruddin, Y. Yang, R. Wang, Oriented nucleation in formamidinium perovskite for photovoltaics. *Nature* **620**, 323-327 (2023).
52. Y.-H. Lin, N. Sakai, P. Da, J. Wu, H. C. Sansom, A. J. Ramadan, S. Mahesh, J. Liu, R. D. J. Oliver, J. Lim, L. Aspitarte, K. Sharma, P. K. Madhu, A. B. Morales-Vilches, P. K. Nayak, S. Bai, F. Gao, C. R. M. Grovenor, M. B. Johnston, J. G. Labram, J. R. Durrant, J. M. Ball, B. Wenger, B. Stannowski, H. J. Snaith, A piperidinium salt stabilizes efficient metal-halide perovskite solar cells. *Science* **369**, 96-102 (2020).
53. K. Domanski, E. A. Alharbi, A. Hagfeldt, M. Grätzel, W. Tress, Systematic investigation of the impact of operation conditions on the degradation behaviour of perovskite solar cells. *Nat. Energy* **3**, 61-67 (2018).
54. S. Yang, S. Chen, E. Mosconi, Y. Fang, X. Xiao, C. Wang, Y. Zhou, Z. Yu, J. Zhao, Y. Gao, F. De Angelis, J. Huang, Stabilizing halide perovskite surfaces for solar cell operation with wide-bandgap lead oxysalts. *Science* **365**, 473-478 (2019).
55. F. Fu, S. Pisoni, Q. Jeangros, J. Sastre-Pellicer, M. Kawecki, A. Paracchino, T. Moser, J. Werner, C. Andres, L. Duchêne, P. Fiala, M. Rawlence, S. Nicolay, C. Ballif, A. N. Tiwari, S. Buecheler, I2 vapor-induced degradation of formamidinium lead iodide based perovskite solar cells under heat–light soaking conditions. *Energy Environ. Sci.* **12**, 3074-3088 (2019).
56. A. Dasgupta, S. Mahesh, P. Caprioglio, Y.-H. Lin, K.-A. Zaininger, R. D. J. Oliver, P. Holzhey, S. Zhou, M. M. McCarthy, J. A. Smith, M. Frenzel, M. G. Christoforo, J. M. Ball, B. Wenger, H. J. Snaith, Visualizing Macroscopic Inhomogeneities in Perovskite Solar Cells. *ACS Energy Lett.* **7**, 2311-2322 (2022).
57. J. C. de Mello, H. F. Wittmann, R. H. Friend, An improved experimental determination of external photoluminescence quantum efficiency. *Adv. Mater.* **9**, 230-232 (1997).
58. T. Kirchartz, J. A. Márquez, M. Stolterfoht, T. Unold, Photoluminescence-Based Characterization of Halide Perovskites for Photovoltaics. *Adv. Energy Mater.* **10**, 1904134 (2020).

59. A. M. Ulatowski, M. D. Farrar, H. J. Snaith, M. B. Johnston, L. M. Herz, Revealing Ultrafast Charge-Carrier Thermalization in Tin-Iodide Perovskites through Novel Pump–Push–Probe Terahertz Spectroscopy. *ACS Photonics* **8**, 2509-2518 (2021).
60. C. Wehrenfennig, M. Liu, H. J. Snaith, M. B. Johnston, L. M. Herz, Charge-carrier dynamics in vapour-deposited films of the organolead halide perovskite CH3NH3PbI3−xClx. *Energy Environ. Sci.* **7**, 2269-2275 (2014).
61. G. Ashiotis, A. Deschildre, Z. Nawaz, J. P. Wright, D. Karkoulis, F. E. Picca, J. Kieffer, The fast azimuthal integration Python library: pyFAI. *J. Appl. Crystallogr.* **48**, 510-519 (2015).
62. G. Kresse, J. Hafner, Ab initio molecular dynamics for liquid metals. *Phys. Rev. B* **47**, 558-561 (1993).
63. G. Kresse, J. Furthmüller, Efficient iterative schemes for ab initio total-energy calculations using a plane-wave basis set. *Phys. Rev. B* **54**, 11169-11186 (1996).
64. G. Kresse, J. Furthmüller, Efficiency of ab-initio total energy calculations for metals and semiconductors using a plane-wave basis set. *Comput. Mater. Sci.* **6**, 15-50 (1996).
65. P. E. Blöchl, Projector augmented-wave method. *Phys. Rev. B* **50**, 17953-17979 (1994).
66. J. P. Perdew, A. Ruzsinszky, G. I. Csonka, O. A. Vydrov, G. E. Scuseria, L. A. Constantin, X. Zhou, K. Burke, Restoring the Density-Gradient Expansion for Exchange in Solids and Surfaces. *Phys. Rev. Lett.* **100**, 136406 (2008).
67. S. Grimme, J. Antony, S. Ehrlich, H. Krieg, A consistent and accurate ab initio parametrization of density functional dispersion correction (DFT-D) for the 94 elements H-Pu. *J Chem Phys* **132**, 154104 (2010).
68. C. L. Davies, J. B. Patel, C. Q. Xia, L. M. Herz, M. B. Johnston, Temperature-Dependent Refractive Index of Quartz at Terahertz Frequencies. *J. Infrared Millim. Terahertz Waves* **39**, 1236-1248 (2018).
69. K. Galkowski, A. Mitioglu, A. Miyata, P. Plochocka, O. Portugall, G. E. Eperon, J. T.-W. Wang, T. Stergiopoulos, S. D. Stranks, H. J. Snaith, R. J. Nicholas, Determination of the exciton binding energy and effective masses for methylammonium and formamidinium lead tri-halide perovskite semiconductors. *Energy Environ. Sci.* **9**, 962-970 (2016).
70. A. Miyata, A. Mitioglu, P. Plochocka, O. Portugall, J. T.-W. Wang, S. D. Stranks, H. J. Snaith, R. J. Nicholas, Direct measurement of the exciton binding energy and effective masses for charge carriers in organic–inorganic tri-halide perovskites. *Nat. Phys.* **11**, 582-587 (2015).
71. V. D'Innocenzo, G. Grancini, M. J. P. Alcocer, A. R. S. Kandada, S. D. Stranks, M. M. Lee, G. Lanzani, H. J. Snaith, A. Petrozza, Excitons versus free charges in organo-lead tri-halide perovskites. *Nat. Commun.* **5**, 3586 (2014).
72. B. L. Henke, E. M. Gullikson, J. C. Davis, X-Ray Interactions: Photoabsorption, Scattering, Transmission, and Reflection at E = 50-30,000 eV, Z = 1-92. *At. Data Nucl. Data Tables* **54**, 181-342 (1993).
73. O. J. Weber, D. Ghosh, S. Gaines, P. F. Henry, A. B. Walker, M. S. Islam, M. T. Weller, Phase Behavior and Polymorphism of Formamidinium Lead Iodide. *Chem. Mater.* **30**, 3768-3778 (2018).
74. D. B. Mitzi, Synthesis, Crystal Structure, and Optical and Thermal Properties of (C4H9NH3)2MI4 (M = Ge, Sn, Pb). *Chem. Mater.* **8**, 791-800 (1996).
75. T. J. Jacobsson, A. Hultqvist, A. García-Fernández, A. Anand, A. Al-Ashouri, A. Hagfeldt, A. Crovetto, A. Abate, A. G. Ricciardulli, A. Vijayan, A. Kulkarni, A. Y. Anderson, B. P.

Darwich, B. W. Yang, B. L. Coles, C. A. R. Perini, C. Rehermann, D. Ramirez, D. Fairen-Jimenez, D. Di Girolamo, D. L. Jia, E. Avila, E. J. Juarez-Perez, F. Baumann, F. Mathies, G. S. A. González, G. Boschloo, G. Nasti, G. Paramasivam, G. Martínez-Denegri, H. Näsström, H. Michaels, H. Köbler, H. Wu, I. Benesperi, M. I. Dar, I. B. Pehlivan, I. E. Gould, J. N. Vagott, J. Dagar, J. Kettle, J. Yang, J. Z. Li, J. A. Smith, J. Pascual, J. J. Jerónimo-Rendón, J. F. Montoya, J. P. Correa-Baena, J. M. Qiu, J. X. Wang, K. Sveinbjörnsson, K. Hirselandt, K. Dey, K. Frohna, L. Mathies, L. A. Castriotta, M. H. Aldamasy, M. Vasquez-Montoya, M. A. Ruiz-Preciado, M. A. Flatken, M. V. Khenkin, M. Grischek, M. Kedia, M. Saliba, M. Anaya, M. Veldhoen, N. Arora, O. Shargaieva, O. Maus, O. S. Game, O. Yudilevich, P. Fassl, Q. S. Zhou, R. Betancur, R. Munir, R. Patidar, S. D. Stranks, S. Alam, S. Kar, T. Unold, T. Abzieher, T. Edvinsson, T. W. David, U. W. Paetzold, W. Zia, W. F. Fu, W. W. Zuo, V. R. F. Schröder, W. Tress, X. L. Zhang, Y. H. Chiang, Z. Iqbal, Z. Q. Xie, E. Unger, An open-access database and analysis tool for perovskite solar cells based on the FAIR data principles. *Nat. Energy* **7**, 107-115 (2022).

76. X. Zhao, T. Liu, Q. C. Burlingame, T. Liu, R. Holley, G. Cheng, N. Yao, F. Gao, Y.-L. Loo, Accelerated aging of all-inorganic, interface-stabilized perovskite solar cells. *Science* **0**, eabn5679 (2022).

77. S. Bai, P. Da, C. Li, Z. Wang, Z. Yuan, F. Fu, M. Kawecki, X. Liu, N. Sakai, J. T.-W. Wang, S. Huettner, S. Buecheler, M. Fahlman, F. Gao, H. J. Snaith, Planar perovskite solar cells with long-term stability using ionic liquid additives. *Nature* **571**, 245-250 (2019).

78. Y. Yang, S. Cheng, X. Zhu, S. Li, Z. Zheng, K. Zhao, L. Ji, R. Li, Y. Liu, C. Liu, Q. Lin, N. Yan, Z. Wang, Inverted perovskite solar cells with over 2,000 h operational stability at 85 °C using fixed charge passivation. *Nat. Energy*, (2023).

79. P. Chen, Y. Xiao, J. Hu, S. Li, D. Luo, R. Su, P. Caprioglio, P. Kaienburg, X. Jia, N. Chen, J. Wu, Y. Sui, P. Tang, H. Yan, T. Huang, M. Yu, Q. Li, L. Zhao, C.-H. Hou, Y.-W. You, J.-J. Shyue, D. Wang, X. Li, Q. Zhao, Q. Gong, Z.-H. Lu, H. J. Snaith, R. Zhu, Multifunctional ytterbium oxide buffer for perovskite solar cells. *Nature* **625**, 516-522 (2024).

80. S. Wu, Z. Li, M.-Q. Li, Y. Diao, F. Lin, T. Liu, J. Zhang, P. Tieu, W. Gao, F. Qi, X. Pan, Z. Xu, Z. Zhu, A. K. Y. Jen, 2D metal–organic framework for stable perovskite solar cells with minimized lead leakage. *Nat. Nano.* **15**, 934-940 (2020).

Acknowledgments: YHL, XLC, and FSYY acknowledge the support of the Early Career Scheme (No. 26210623) from the Hong Kong Research Grant Council (RGC). MSI and V acknowledge the Department of Materials at the University of Oxford and the Engineering and Physical Sciences Research Council (EPSRC) Programme Grant (EP/X038777/1) for the postdoctoral fellowship and are grateful to the UK's HEC Materials Chemistry Consortium (EP/X035859/1) for the use of the ARCHER2 high-performance computing facilities. RDJO and AD gratefully acknowledge the Penrose Scholarship for funding their studentships. QY acknowledges the support of Rank Prize through a Return to Research grant. XMaS is a UK national research facility supported by the EPSRC. FY is grateful to all the ESRF beamline team staff for their support. MBJ thanks the EPSRC for an Established Career Fellowship EP/T025077/1.

Author contributions: YHL and HJS conceived the ideas. HJS supervised the project and progress. YHL developed methodologies, fabricated perovskite samples, conducted current-voltage and stability characterizations on perovskite devices, and coordinated collaborations. V and MSI conducted and analyzed the computer simulations on molecule-surface interactions. AD conducted photoluminescence imaging measurements. FY conducted x-ray diffraction and grazing-incidence wide-angle x-ray scattering measurements and their analyses. RDJO conducted photoluminescence quantum yield, external quantum efficiency, and electroluminescence quantum efficiency measurements and helped mechanistic analyses. XLC conducted time-of-flight secondary ion mass spectrometry measurements and performed X-ray diffraction pattern analyses. AMU conducted terahertz photoconductivity measurements and early X-ray and photoluminescence analyses. MMM conducted scanning electron microscopy measurements and helped optimize methodologies. XS conducted radiative efficiencies analyses and literature comparison. QY conducted evaporated electron transport layer optimization. MGC set up solar characterization facilities. FSYY, MBJ, NKN, and LMH assisted with characterization analyses and supervised their group members who contributed to this work. YHL, V, FY, XLC, MSI, and HJS wrote the first draft of the manuscript. All the authors discussed the results and contributed to the writing of the manuscript.

Competing interests: HJS is a founder and CSO of Oxford Photovoltaics Ltd. MGC is a director and co-owner of Ark Metrica Ltd. Oxford University has filed patents related to the content of this work. All the other authors declare no competing interests.

Data and materials availability: All data are available in the main text or the supplementary materials.

Supplementary Materials

Materials and Methods

Supplementary Text

Figs. S1 to S40

Tables S1 to S3

References (57–80)

Movies S1 to S7

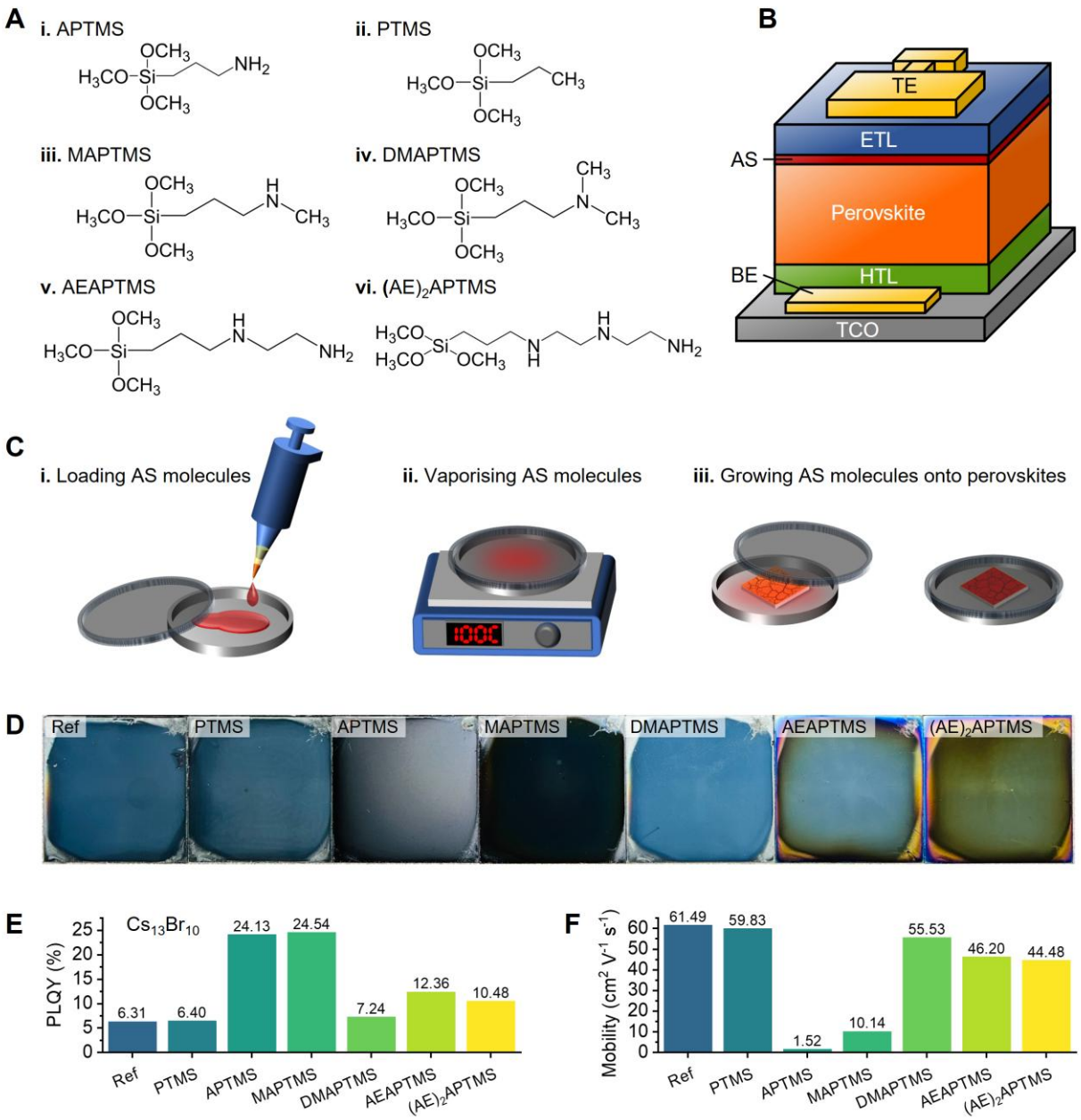

Fig. 1. Amino-silane molecules and their fabrication and optoelectronic properties. (**A**) Structures of amino-silane (AS) molecules, (3-aminopropyl)trimethoxysilane (APTMS), trimethoxy(propyl)silane (PTMS), trimethoxy[3-(methylamino)propyl]silane (MAPTMS), (N, N-Dimethylaminopropyl)trimethoxysilane (DMAPTMS), [3-(2-aminoethylamino)propyl]trimethoxysilane (AEAPTMS) and 3-[2-(2-aminoethylamino)ethylamino]propyltrimethoxysilane [$(AE)_2$APTMS]. (**B**) Schematic of a positive-intrinsic-negative solar cell architecture, where ETL is electron transport layer, HTL is hole transport layer, TE is top electrode, BE is bottom electrode, and TCO is transparent conductive oxide. (**C**) Illustration of the vapor-based deposition adopted for passivation molecules: (i) loading an AS molecule chosen from Fig. 1A in a petri dish; (ii) heating the passivation molecule containing petri dish at 100 °C for a few minutes until all the molecules are vaporized; and (iii) placing an as-grown perovskite film sample inside the petri dish for tens of seconds to a

couple of minutes (see fig. S5 for the optimal AEAPTMS exposure time). (**D**) Photos of perovskite films made on ITO glass substrates and treated with the molecules shown in Fig. 1A and without any treatment (Ref, i.e., reference). (**E**) Photoluminescence quantum yield (PLQY) and (**F**) THz mobility of $Cs_{13}Br_{10}$ perovskite films treated with molecules shown in Fig. 1A and without any treatments (i.e., Ref).

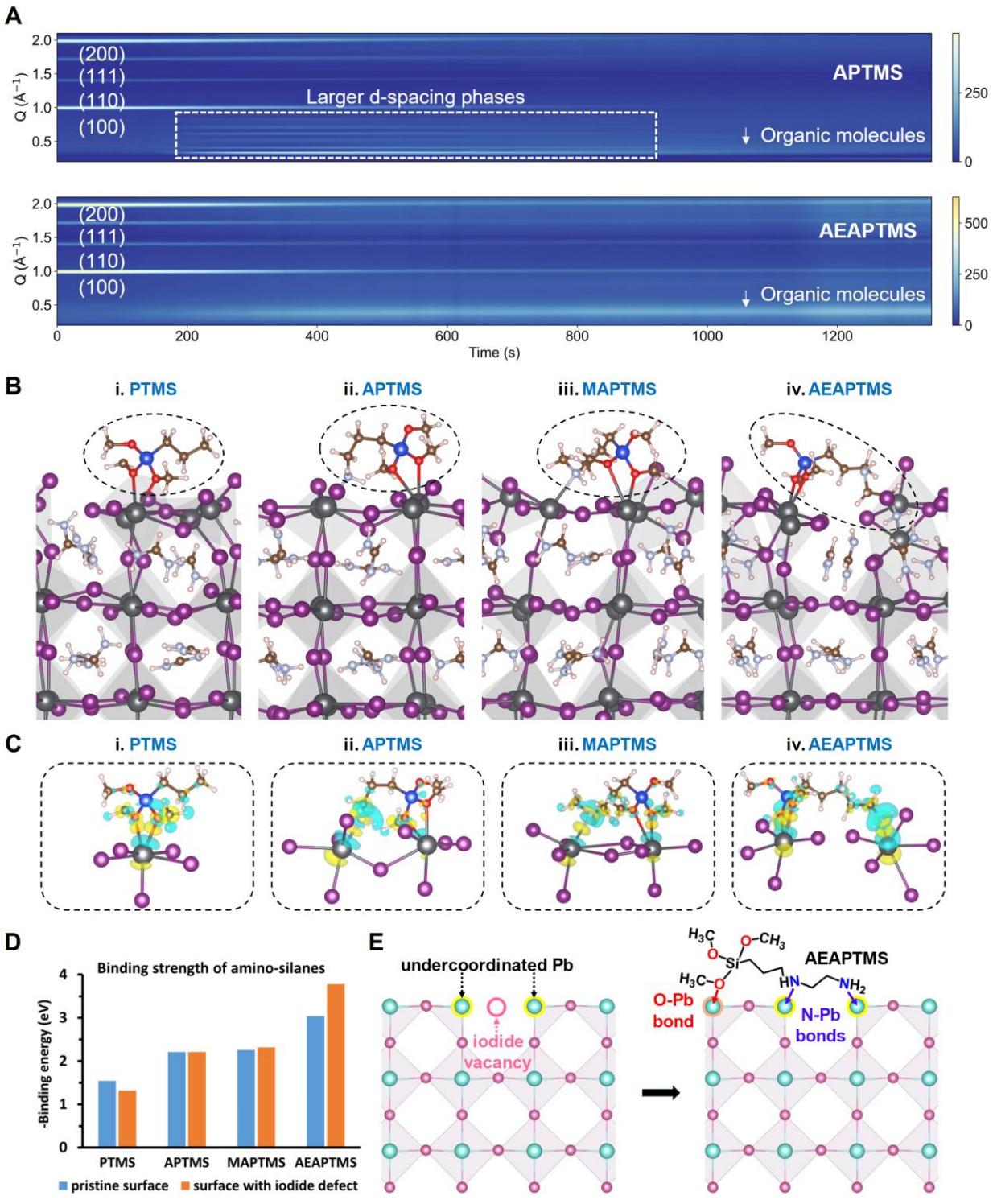

Fig. 2. Structural analysis of the amino-silane surface interactions. (**A**) Time-dependent GIWAXS patterns measured at incident angles of 1° for the vapor-based treatment with APTMS (top) and AEAPTMS (bottom) on $I_{0.9}Br_{0.1}$ perovskite films, with the background signals from air scattering, Kapton-taped window, glass, and ITO removed. The slight tilt observed in all of the signals acquired with time was caused by the thermal extension of the sample stage, which caused

a partial loss of alignment. (**B**) Side views of the simulated structures using DFT and AIMD techniques of the interactions of the amino-silanes PTMS, APTMS, MAPTMS and AEAPTMS with the Pb/I terminated (001) $FAPbI_3$ surface. PbI_6 octahedra are highlighted to show that the major structural relaxation is found mostly in the uppermost layer. (**C**) Changes in the charge density profile around all of the species involved in the silane-surface binding; the prominent charge accumulation (yellow) and depletion (blue) regions show N-Pb and O-Pb interactions. (**D**) Binding energies of amino-silanes on the pristine surface and on the iodide vacancy defect surface. (**E**) Schematic diagram showing the perovskite surface with undercoordinated Pb cations adjacent to an iodide vacancy, and the binding of an AEAPTMS molecule via N-Pb and O-Pb bonds. Here, FA^+ cations are omitted for clarity.

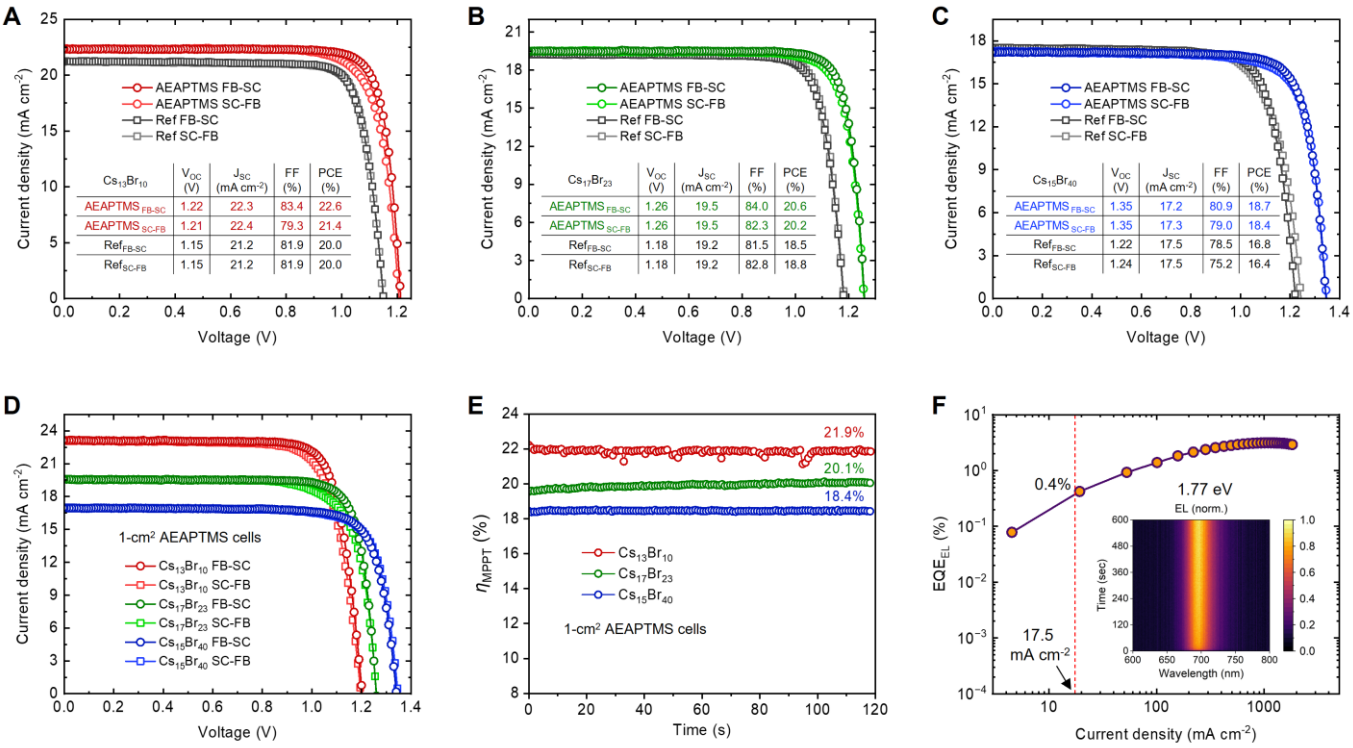

Fig. 3. Perovskite solar cell characterization. (**A** to **C**) Current density and voltage characteristics of the representative AEAPTMS-treated perovskite solar cells with an aperture size of 0.25 cm^2 using an absorber composition of $Cs_{13}Br_{10}$ (A) $Cs_{17}Br_{23}$ (B) $Cs_{15}Br_{40}$ (C), where FB-SC indicates the scan direction from the forward bias (FB) to short circuit (SC) condition, and vice versa for SC-FB. Insets of (a-c) summarize critical PV performance parameters. (**D** and **E**) Current density and voltage characteristics of the representative large-area 1-cm^2 AEAPTMS-treated cells based on the compositions of $Cs_{13}Br_{10}$, $Cs_{17}Br_{23}$, and $Cs_{15}Br_{40}$ (D) while the corresponding maximum power point tracking (MPPT) efficiencies (η) for 120 seconds are shown in (E). (**F**) Electroluminescence quantum efficiency (EQE_{EL}) as a function of injection current densities, where the current density of 17.5 mA cm^{-2} results in an EQE_{EL} of 0.4%. The EQE_{EL} data were obtained under the operation of a voltage sweep between 0 and 4 V (fig. S30C) for an AEAPTMS-treated $Cs_{15}Br_{40}$-based perovskite solar cell (fig. S30, A and B). The inset shows the normalized EL spectrum under a current injection of 17 mA cm^{-2} over the course of 600 s, whereas the EQE_{EL} data tracked over 600 s are shown in fig. S30D.

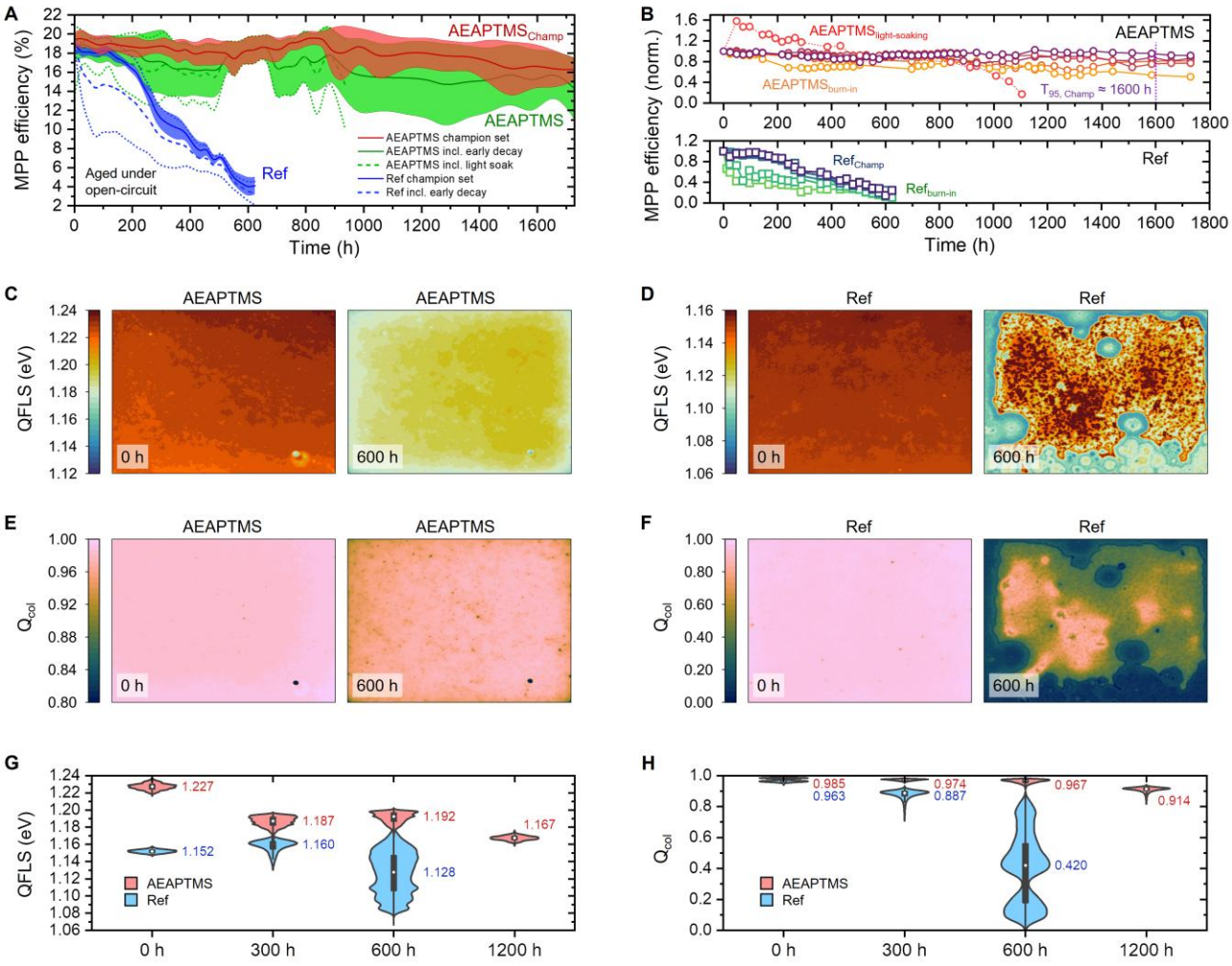

Fig. 4. Operational stability and aging characterization. (**A**) Evolution of mean MPP efficiency (with the corresponding standard deviations in a band plot) of encapsulated AEAPTMS-treated and reference (Ref) $Cs_{13}Br_{10}$ cells (including six AEAPTMS-based and five reference cells) aged under an open-circuit condition and full-spectrum simulated sunlight at 85 °C (as measured and set with a black standard thermometer) in ambient air with a relative humidity in the laboratory of 50 to 60%. MPP was tracked for 120 s for each cell at different aging stages. The datasets including some solar cells with distinct degradation pathways, i.e., light-soaking and burn-in, are explicitly indicated. (**B**) Evolution of normalized MPP efficiency for individual cells used and recorded for (A). For the champion cell, the time taken to reach 95% of its initial MPP ($T_{95, Champ}$) is approximately 1,600 hours. (**C** and **D**) PL-derived QFLS maps of the full-area 0.25-cm^2 AEAPTMS-treated (C) and ref $Cs_{13}Br_{10}$ (D) cells before ageing (0 h) and after ageing under the condition as described in (A), for 600 hours. (**E** and **F**) Charge collection quality (Q_{col}) maps for AEAPTMS-treated (E) and reference (F) cells calculated corresponding to (C) and (D), respectively. (**G** and **H**) Statistical results of QFLS (G) and Q_{col} (H) shown in a violin plot, where the median, interquartile range and 1.5× interquartile range are indicated as a dot, a box, and a line, respectively, for all of the cells recorded in (B). Each QFLS and Q_{col} map represents an area of 5.38 mm by 4.67 mm.

Science
AAAS

Supplementary Materials for

Bandgap-universal passivation enables stable perovskite solar cells with low photovoltage loss

Yen-Hung Lin, Vikram, Fengning Yang, Xue-Li Cao, Akash Dasgupta, Robert D. J. Oliver, Aleksander M. Ulatowski, Melissa M. McCarthy, Xinyi Shen, Qimu Yuan, M. Greyson Christoforo, Fion Sze Yan Yeung, Michael B. Johnston, Nakita K. Noel, Laura M. Herz, M. Saiful Islam, Henry J. Snaith

Corresponding author: yh.lin@ust.hk , henry.snaith@physics.ox.ac.uk

The PDF file includes:

Other Supplementary Materials for this manuscript include the following:

Materials and Methods

Precursor material preparation

Lead iodide (PbI_2, 99.99%), lead bromide ($PbBr_2$, > 98.0%) and [4-(3,6-Dimethyl-9H-carbazol-9-yl)butyl]phosphonic acid (Me-4PACz, > 99.0%) were purchased from TCI. Formamidinium iodide (FAI, > 99.99%) was purchased from Dyenamo. [6,6]-phenyl-C_{61}-butyric acid methyl ester ($PC_{61}BM$, > 99.5%) was purchased from Solenne BV. Bathocuproine (BCP, 98%) for solution process and cesium iodide (CsI, 99.9%) were purchased from Alfa Aesar. For solar cells based on an evaporated ETL, C_{60} (99.9%) and BCP (99.5%) were purchased from Acros Organics and Sigma-Aldrich, respectively. Aluminum oxide nanoparticle dispersion (20 wt. % in isopropanol, IPA) was purchased from Sigma-Aldrich. Unless stated otherwise, all other materials and solvents were purchased from Sigma-Aldrich. In this work, all the materials were used as received without further purification. To form the mixed-cation lead mixed-anion perovskite precursor solutions, CsI, FAI, PbI_2, and $PbBr_2$ were prepared in the way corresponding to the exact stoichiometry for the hybrid perovskite composition [i.e. $Cs_xFA_{1-x}Pb(I_{1-y}Br_y)_3$; (i) for 1.6 eV cells, x = 0.13 and y = 0.10; (ii) for 1.67 eV cells, x = 0.17 and y = 0.23; (ii) for 1.77 eV cells, x = 0.15 and y = 0.4] in a mixed organic solvent system comprising N, N-dimethylformamide (DMF) and dimethyl sulfoxide (DMSO) at the volume ratio of DMF:DMSO = 4:1. The perovskite precursor concentrations were 1.41 M and 1.39 M for 1.6 eV cells and 1.67/1.77 eV cells, respectively. The perovskite precursor solutions were stirred overnight in a nitrogen-filled glovebox and used without any further treatment.

Film deposition, surface passivation, and solar cell fabrication

Indium tin oxide (ITO) coated glass substrates were cleaned in a series of ultrasonic cleaning baths using various solutions and solvents in the following sequence: 1) deionized water with 2% v/v solution of Decon 90 cleaning detergent; 2) deionized water; 3) acetone and 4) isopropanol (each step for ~ 10 minutes). After ultrasonic cleaning, substrates were dried with compressed nitrogen and then treated with UV-Ozone for 20 minutes before use. After the substrate cleaning procedure, Me-4PACz (0.5 mg mL^{-1} in ethanol) was deposited by dispensing the as-prepared organic solution onto a spinning substrate at 3,000 rpm for 20 seconds, followed by thermal annealing at 130 ℃ for 5 min in ambient air. Next, aluminum oxide nanoparticle dispersion (1:150 vol% in IPA) were spin coated dynamically after the Me-4PACz deposition at 2000 rpm for 30 seconds as a wetting agent. The deposition of the perovskite layers was carried out using a spin coater in a nitrogen-filled glovebox with the following processing parameters: starting at 1,000 rpm for 5 seconds (ramping time of 5 seconds from stationary status) and then 5,000 rpm (ramping time of 5 seconds from 1,000 rpm) for 30 seconds. Before the end of the spinning process, a solvent-quenching method was used by dropping anisole of 200 μL onto the spinning substrates at 35 seconds after the start of the spin-coating process. The thermal annealing process (100 ℃ for 50 minutes) was then carried out for the formation of the perovskite layer. To carry out surface passivation using amino-silane treatments on perovskite, we first loaded one type of amino-silane molecules chosen from Fig. 1A in a petri dish. We then heated the molecule containing petri dish at 100 ℃ for a few minutes until all the molecules are vaporized. Lastly, we placed an as-grown perovskite film sample inside the petri dish for tens of seconds to a couple of minutes. The optimal deposition time for the best performing amino-silane treated perovskite solar cells was around 100 ± 20 seconds (fig. S5) when using a petri dish with a dimension of Ø 100 × 20 mm. For $PC_{61}BM$-based cells, the as-prepared $PC_{61}BM$ solution (20 mg mL^{-1} in a mixed solvent of chlorobenzene, CB, and 1,2-dichlorobenzene, o-DCB, at the volume ratio of CB : o-DCB = 3:1) was dynamically

spun onto the treated or untreated perovskite layers at a speed of 2,000 rpm for 20 seconds. The samples were then annealed at 100 ℃ for 5 minutes. After cooling. down to room temperature, the as-prepared BCP solution (0.5 mg mL^{-1} in isopropanol) was dynamically spun onto the $PC_{61}BM$ layer at a speed of 4000 rpm for 20 seconds, followed by a brief thermal annealing process at 100 ℃ for ~ 1 minute. Both $PC_{61}BM$ and BCP layers were processed inside the nitrogen-filled glovebox. For C_{60}-based devices, the evaporation chamber was pumped down to a base pressure between 8×10^{-7} and 2×10^{-6} mbar for both the 20-nm C_{60} and 2-nm BCP depositions. The walls of the chamber were maintained at 17 ℃ and the rotating substrate at 20 ℃ through two separate chillers. The solar cells were completed by thermal evaporation of Cr (3.5 nm) and Au electrodes (100 nm) through shadow masks under high vacuum (5×10^{-6} mbar) using a thermal evaporator (Nano 36, Kurt J. Lesker) placed in the ambient environment.

Solar cell characterisation and stability test

Current-voltage and maximum power point measurements were measured using two Keithley 2400 series source meters in the ambient environment under both simulated sunlight (AM 1.5 irradiance generated by a Wavelabs SINUS-220 simulator) and in the dark. The active area of the solar cell was masked with a black-anodized metal aperture to either 0.25 or 1 cm^2, within a light-tight holder. The current-voltage characteristics were taken from a "reverse" scan (i.e., from "forward bias" to "short circuit") followed by a forward scan (i.e., from short circuit to forward bias) at a scan rate of 245 mV s^{-1}. Subsequently, active maximum power point tracking measurements using a gradient descent algorithm were performed for 120 seconds to obtain the maximum power point tracked efficiency. The intensity of the solar simulator was set periodically such that the short-circuit current density from a KG3-filtered Si reference photodiode (Fraunhofer ISE) matched its 1-sun certified value. A local measurement of the intensity before each batch of solar cell measurements were performed, was made by integrating the spectrum obtained from the solar simulator's internal spectrometer. By taking the ratio of this internal intensity measurement to one obtained at the time of calibration we determined the equivalent irradiance at the time of measurement. The mismatch factor estimated for the test cells, calibration cells and simulator was estimated to be less than 1% and was hence not applied.

The perovskite solar cells were first covered by a thin layer of CYTOP™ (CTL-809M, AGC Chemicals), which was dried under vacuum, followed by an encapsulation process using a cover glass (28.0 mm × 21.5 mm × 1.1 mm for the glass and 25 mm × 18.5 mm × 0.5 mm for the cavity, AMG) and UV adhesive (LT-U001, Lumtec) in a nitrogen-filled glovebox. All the encapsulated devices were aged using an Atlas SUNTEST CPS+ (1,500 W air-cooled Xenon lamp) light-soaking chamber under simulated full-spectrum AM1.5 sunlight with ~ 77 mW cm^{-2} irradiance and without applying any UV filters. All the aging tests performed in this work were conducted in open-circuit conditions. To carry out current-voltage characterizations, the samples were taken out from the chamber and tested at different ageing times, following the measurement protocol as described above. The ageing chamber for storing the encapsulated samples was air-cooled with the temperature controlled at 85 ℃ (measured using a black standard temperature control unit positioned next to the test cells). During the ageing period, the relative humidity in the laboratory (at ~ 21°C) was monitored in the range of 50 ~ 60%.

Photoluminescence quantum yield

Photoluminescence quantum yield (PLQY) measurements were conducted using the de Mello method (*57*). A 532 nm CW laser diode (ThorLabs DJ532-10), coupled into an optical fiber and

into an integrating sphere, was used to photoexcite the samples. The intensity of the laser was adjusted to provide a 1-sun equivalent photon flux, taking into account the excitation wavelength and the bandgaps of the absorbing materials studied in this work (*58*). A second optical fiber was used from the output of the integrating sphere to a QEPro spectrometer (OceanOptics). The system was calibrated by using a calibrated halogen lamp with specified spectral irradiance (HL-3P-INT-CAL, OceanInsight), which was shone into to integrating sphere. A spectral correction factor was established to match the spectral output of the detector to the calibrated spectral irradiance of the lamp.

External quantum efficiency

We measured the external quantum efficiency (EQE) of our devices using a home-built Fourier transform photocurrent spectroscopy system based on a Bruker Vertex 80v Fourier transform interferometer. The solar cells were masked with a metal aperture such that the whole active area was illuminated by a tungsten halogen lamp. To determine the EQE, the photocurrent spectrum of the device under test was divided by that of a calibrated Si reference cell (Newport) of a known EQE. The acquisition time for each photocurrent spectrum was ~ 60 s and was conducted in ambient conditions. To determine the equivalent short-circuit current density under 1 sun irradiance from the EQE measurements, the overlap integral of the AM1.5 photon flux ($\varphi_{\mathrm{AM1.5}}$) spectrum with the EQE was calculated. Explicitly, this is given by

$$J_{\mathrm{sc}} = \int_0^{\infty} \varphi_{\mathrm{AM1.5}}(\lambda) EQE(\lambda)\, \mathrm{d}\lambda$$

where q is the elementary charge and λ is the wavelength.

For the comparison between fresh and aged perovskite solar cells, the EQE measurements were carried out by illuminating cells with a 250 W quartz-tungsten halogen lamp. The light illumination first goes through a monochromator (Princeton Instruments SP2150) with a filter wheel (Princeton Instruments FA2448) and is followed by being chopped with an optical chopper (Thorlabs MC2000B) at 280Hz and focused onto the measured cell with a smaller spot size than the solar cell area (as defined by the metallic top contact). The amplitude of the resulting AC signal was measured with a lock-in amplifier (Stanford Research Systems SR830) as the voltage drop across a 50-Ω resistor connected in series with the solar cell under measurement.

Electroluminescence quantum efficiency

Electroluminescence quantum efficiency ($\mathrm{EQE_{EL}}$) were performed in an integrating sphere with perovskite solar cells placed in a home-made holder mounted to one side of the sphere. The emission spectrum and intensity were simultaneously measured by an OceanOptics QEPro calibrated grating spectrometer. The current density-voltage characteristics were obtained using a source meter (Keithley 2400).

Terahertz photoconductivity

The photoinduced, time-resolved conductivity was measured using the optical-pump terahertz (THz)-probe technique as described in our previous works (*59, 60*). The thin films were photoexcited with laser pulses from a Ti:Sapphire laser system (35-fs pulse duration, 800-nm central wavelength, 5-kHz repetition rate; a Spectra Physics MaiTai-Ascend-Spitfire regenerative amplifier). The pulses were then frequency-doubled to 400 nm central wavelength using a BBO crystal. The excitation fluence was controlled with a neutral density filter wheel. The time delay

between the optical pump pulse and the probing THz pulse was adjusted with optical delay stages. THz radiation was generated using a spintronic emitter (2 nm tungsten, 1.8 nm $Co_{40}Fe_{40}B_{20}$, 2 nm platinum on quartz substrates). The transmitted THz radiation was measured using electro-optic sampling in a 1-mm thick ZnTe (110) crystal with an 800 nm-wavelength gate beam originating from the same laser system mentioned above. The polarization of the gate beam was measured using a quarter-wave plate, Wollaston prism, and a balanced photodiode detector. The details of the THz photoconductivity analysis are described in the supplementary text.

Photoluminescence imaging

The photoluminescence (PL) images taken for this work employed the same setup our previous report (*56*). The sample is excited optically with a 440-nm LED light, and electronically contacted by a source meter (Keithley 2636). The excitation intensity was controlled by controlling the current draw of the LED. The intensity of the LED which corresponds to an equivalent 1 sun illumination was determined by measuring the current at the short-circuit condition and varying the intensity till this current matched that measured on the solar simulator. The spatially resolved photoluminescence maps were obtained using a scientific CMOS camera sensor (Andor Zyla 4.2, Oxford Instruments). A long pass filter was used to stop the excitation light from entering the camera, so that only the PL was incident on the sensor.

X-ray diffraction

X-ray diffraction (XRD) patterns were measured at room temperature using a PANalytical X'Pert PRO diffractometer equipped with a Cu line focus X-ray tube run at 45 kV with a tube current of 40 mA (Cu Kα radiation, $\lambda = 1.506$ Å). In a Bragg-Brentano geometry setup, the 1D detector collected data from each sample, with a typical collection time of 60 minutes per sample. The alignment was calibrated using ITO, avoiding any shifts in peaks due to the sample tilting. The lattice parameters are calculated using the TOPAS software.

Ex-situ grazing-incidence wide-angle X-ray scattering

The ex-situ grazing-incidence wide-angle X-ray scattering (GIWAXS) data were recorded with a Rigaku SmartLab diffractometer, equipped with a HyPix-3000 hybrid pixel-array 2D detector and a rotating 3 kW Cu Kα source (operating at 40 kV, 45 mA). X-ray photons with energy of 8.048 keV and CBO-f optics were incident on an aligned sample surface, held at grazing incidence angles of 0.5° and 1.5°. The samples were mounted on a 2D-XRD attachment stage with a beam stop for the direct beam, which was positioned 65 mm away from the detector. Detector images were integrated and resampled into Q-space and were combined using scripts based on the PyFAI and pygix libraries. These libraries were also used for azimuthally integrated 1D profiles (*61*). For variable-angle GIWAXS measurements ($\alpha i = 0.5°-1.5°$), samples were measured using a different 2D-XRD aperture slit configuration with parallel-beam optics, a 0.5° in-plane parallel-slit collimator, a 0.1 mm incident slit, and a 10 mm length-limiting slit at a single detector position, before processing as described above.

In-situ grazing-incidence wide-angle X-ray scattering

In-situ GIWAXS measurements were conducted at the XMaS beamline at the European Synchrotron Radiation Facility (ESRF). Perovskite films were put into a homemade cell to carry out the in-situ vapor treatment process (see fig. S14) at temperatures rising from 50 to 80 °C using a built-in hotplate. The characterizations were carried out with a constant flow of nitrogen to create

an inert gas environment. The synchrotron beam with an energy of 12.4 keV (λ = 0.9998 Å) and a diameter of ~ 100 µm was incident at an angle of 1°. Scattering signals were collected using a Pilatus 1M hybrid photon counting detector at a distance of 279.3 mm and 1-second increments, with the geometry calibrated using lanthanum hexaboride as the calibrant. All the in-situ GIWAXS data was acquired during the experiment session A28-1-1380 at the beamline BM28 (DOI: 10.15151/ESRF-ES-1352731648). Detector images were then resampled into the Q-space and azimuthally integrated using scripts based on PyFAI and pygix libraries.

Scanning electron microscopy

Scanning electron microscopy (SEM) samples were prepared following the perovskite solar cell fabrication process till the perovskite layer and treated with different amino-silane molecules afterward. Top-down SEM images were taken on an FEI Quanta 600 FEG at an accelerating voltage of 3 kV. The SEM chamber was pumped down to high vacuum of $< 2 \times 10^{-4}$ mbar.

Time-of-flight secondary ion mass spectrometry

Perovskite samples for time-of-flight secondary ion mass spectrometry (ToF-SIMS) measurements were prepared following the same procedure used for solar cells. Measurements were conducted using a TOF.SIMS 5 instrument (IONTOF GmbH), which was equipped with a bismuth primary ion source and an O_2^+ sputter source to probe the positive atomic and/or fragment ions. The 3D ToF-SIMS data were acquired over an area of 100 × 100 µm using a 30 keV Bi^+ primary ion beam. This was followed by a sputtering process, with each cycle lasting for 1.5 seconds. During each sputtering cycle, a 350 × 350 µm area of the sample was bombarded with 1 keV O_2^+ ion beams in an interlaced mode. The sample holder, containing the samples, was sealed in a container filled with argon gas and was transferred into the instrument immediately before testing.

Computational modelling

First-principles simulations were performed within the framework of density functional theory (DFT) as implemented in Vienna Ab-initio Simulation Package (VASP) (*62-64*) using a projector augmented-wave (PAW) basis (*65*). The generalized gradient approximation (GGA) exchange-correlation functional of Perdew Burke-Ernzerhof (PBE) modified for solids (PBEsol) was used for all the bulk and surface structures (*66*). VASP-recommended PAW pseudopotentials were used for all the atomic species (C:$2s^2 2p^2$, N:$2s^2 2p^3$, H:$1s^1$, Pb:$5d^{10} 6s^2 6p^2$, I:$5s^2 5p^5$, O:$2s^2 2p^4$, and Si:$3s^2 3p^2$). Grimme's DFT-D3 dispersion correction was considered due to the presence of organic molecules (*67*). A plane wave energy cut-off of 500 eV and a Brillouin zone (BZ) sampling using Γ-centred k-mesh are done for all the calculations. A k-point grid of 4 × 4 × 1 was used to calculate finer proper-ties for the surface slabs, such as the density of states (DOS), charge density difference, and binding energies. Gaussian smearing of 0.1 is used for all the structure optimizations and 0.01 for calculating finer properties. The cell volume, shape, and atomic positions for the bulk structure and only the atomic positions for the surface slabs were fully relaxed using the conjugate gradient algorithm until the force on each atom converge below 0.01 eV $Å^{-1}$. Equivalently, an energy convergence criterion of 10^{-6} eV was used for the electronic degrees of freedom. Such DFT based methods have been applied successfully to other defect and surface studies of perovskite halides (*40-42*).

Supplementary Text

Terahertz photoconductivity analysis

The relative change of THz transmission through the photoexcited and un-excited thin film, ΔT , was measured by selectively blocking half of the pump pulses and half of THz pulses using two optical choppers and recording the resulting four different transmission signals (THz-on–pump-off, THz-off–pump-off, THz- on–pump-on, THz-off–pump-on) with a custom-made, FPGA-based data acquisition board. The photo-induced conductivity σ of a thin film can be expressed as (*60*):

$$\sigma = -\frac{\epsilon_0 c}{d}(1 + n_{sub})\frac{\Delta T}{T}$$

where d is the thickness of the thin film, n_{sub} is the refractive index of the quartz substrate [n_{sub} = 2.1 (*68*)], ΔT is the difference between the THz radiation transmitted through the photoexcited sample and the sample in the dark, and T is the electric field strength of the THz radiation transmitted through the sample in the dark. ϵ_0 and c are the permittivity of free space and speed of light, respectively.

The charge-carrier sum mobility, μ, was calculated from the onset of THz conductivity at t = 0, using the relation between photoinduced conductivity and photoexcited charge-carrier pair density n (*60*),

$$\sigma(t) = \mu n(t) e$$

where e is the electron charge. The number density of photoexcited charge carriers n (t =0) was estimated from the absorption spectra, assuming that all absorbed photons were converted to electron-hole pairs. This assumption is reasonable for lead-halide perovskites at room temperature given their low exciton binding energy (*69-71*).

X-ray diffraction pattern analysis

The X-ray diffraction (XRD) patterns of the $Cs_{0.13}FA_{0.87}Pb(I_{0.9}Br_{0.1})_3$ perovskite film exhibit eight characteristic peaks at 13.89°, 19.71°, 24.24°, 28.09°, 31.50°, 34.61°, 40.19°, and 43.95°, assigned to planes of (100), (110), (111), (200), (210), (121), (220), and (221), respectively (*36*). The full width at half maximum (FWHM) of the films was calculated from the characteristic XRD peaks and was shown in the supplementary table S1. It is clear that the DMAPTMS, MAPTMS, and PTMS-treated perovskite films possess a similar level of crystallinity as the peak positions, intensity and FWHM values for their respective peaks are all similar to the reference sample. For the (100) crystal plane, the FWHM values were found to be 0.123°, 0.115°, and 0.111°, respectively, for DMAPTMS, MAPTMS and PTMS. For the (200) crystal plane, the corresponding FWHM values were measured as 0.05°, 0.057°, and 0.073° for DMAPTMS, MAPTMS and PTMS, respectively. These findings indicate that the three films exhibit a high degree of crystallinity with narrow peak widths, indicating well-defined crystal planes and minimal structural defects. The FWHM of perovskite films reflected a narrowing trend after being treated with AEAPTMS. For example, the FWHM of the (100) peak decreased from 0.113° to 0.103°. Moreover, the FWHM of the (200) diffraction peak narrows from 0.075° for the reference to 0.048°. It can be concluded that the introduction of AEAPTMS improves the crystal orientation and crystallization of the films, indicating a higher degree of film crystallinity, crystal size, and

orientation order. The FWHM values for the (100) peak were found to be 0.271° for the APTMS-treated films and 0.217° for the $(AE)_2$APTMS-treated films, whereas all other samples exhibited values smaller than 0.130°. Similarly, for the (200) crystal plane, the APTMS-treated films showed an FWHM of 0.289°, whilst the $(AE)_2$APTMS-treated films exhibited 0.138°, and all other samples had values smaller than 0.08°. It is demonstrated that APTMS has the most detrimental effects on the crystallization of perovskite films since the FWHM of diffraction peaks broaden the most when passivated with APTMS, indicating the existence of small-sized and randomly oriented perovskite crystals. On the other hand, despite possessing a similar molecular structure as that of AEAPTMS, the characteristic peaks (100) and (200) in the XRD pattern of the $(AE)_2$APTMS-treated perovskite film are broadened when compared with the rest of the amino-silane treated perovskite films. Meanwhile, its XRD diffraction spectrum shows undamaged perovskite characteristic peaks, indicating that $(AE)_2$APTMS-treated perovskite films have a small microstructure.

X-ray attenuation length calculation

To calculate the X-ray attenuation length, we use the following equation (*72*):

$$L_{atten} = \frac{1}{\mu'} = \frac{cos\theta}{(\mu/\rho)\rho}$$

where L_{atten} is the attenuation length, μ' is the effective linear attenuation coefficient, μ is the linear attenuation coefficient, (μ/ρ) is the mass attenuation coefficient, and ρ is the density of the material, θ is the grazing incidence angle. The mass attenuation coefficient depends on the X-ray energy and the chemical composition of the material. The density of the material is calculated to be 4.2 g cm^{-3}, based on the composition of $Cs_{13}Br_{10}$. At grazing incidence angles of 0.5° and 1.5°, the attenuation lengths are calculated to be 71.8 nm and 251.4 nm, respectively.

2D phases in MAPTMS-treated perovskites

For the MAPTMS sample, apart from the perovskite rings, a highly oriented 2D phase appears by fitting one-layer Ruddlesden-Popper (RP) phases (fig. S13). From the in-plane and out-of-plane 1D line cuts shown in fig. S12, it is evident that the orientation of most of the 2D phase perovskite is along the out-of-plane direction. Sharp diffraction peaks emerged at the scattering vector Q_{xy} = 0.43, 0.72, and 0.87 $Å^{-1}$ along the z-axis direction, which we indexed as the (002), (102), and (004) planes of the RP phase perovskite with a layer spacing of approximately 14.2 Å (figs. S11 to S13).

Computational modelling details

Modelling of the PbI_2 terminated (001) perovskite surface was carried out using the optimized α-$FAPbI_3$ bulk 2 × 2 × 2 supercell structure (*73*). The surface slab was taken to be 4 layers thick (23.73 Å) consisting of a total of 192 atoms (16 formula units). A vacuum thickness of, at least, the thickness of the slab and molecule was always maintained. Although (001) $FAPbI_3$ surface consists of alternating charge neutral FAI and PbI_2 layers, a dipole correction along the axis perpendicular to the slab was considered. In all surface calculations, the bottom layer of the slab was fixed to the bulk lattice parameters, allowing top three layers to optimize. Each amino-silane molecule was first optimized to get its preferred structure in a vacuum by placing it in a cubic box of ~ 20 Å to avoid the interaction of the periodic images. The optimized amino-silane molecules were then placed over the (001) $FAPbI_3$ surface on the top of surface Pb-cations as well as parallel to the surface to model the initial structures. All the structures were first optimized with DFT at 0

K before studying their time evolution using ab initio molecular dynamics AIMD at 300 K using a Γ-point mesh in the NVT ensemble. The final AIMD trajectories for amino-silanes over the pristine surface and surface with an iodide Frenkel defect were observed for a time scale of ~ 30 ps and ~ 10 ps, respectively. The binding energies for the silane-surface interaction was calculated as $E_{mol@s}$ - E_{mol} - E_s, where $E_{mol@s}$, E_{mol}, and E_s are the total DFT ground state energies of the molecule over the perovskite surface, isolated molecule, and isolated perovskite surface respectively.

Photoluminescence imaging analysis

The PLQY was estimated by imaging the excitation light incident on a high-reflectance reference plate ($BaSO_4$), placed on the focal plane of the camera, without filter. We use this as a dividing factor for the PLQE, taking into account the wavelength dependent response of the camera lenses and the image sensor itself. The QFLS maps may be obtained from the PLQE map via the relation:

$$\mathrm{QFLS} = \mathrm{QFLS}_{\mathrm{rad}} + kT\ln(\mathrm{PLQY}).$$

The Q_{col} maps were calculated by taking the PL at open circuit and short circuit under 1 sun equivalent illumination, and open circuit PL images as a function of intensity. The latter was used to generate a spatially resolved map of ideality factor, by fitting to the linear relation:

$$\ln(I_{suns}) + C = \frac{\mathrm{QFLS}(I_{suns})}{nkT},$$

where I_{suns} is the illumination intensity expressed as equivalent number of suns, C is a constant, k is the Boltzmann constant, T the temperature, and n the ideality factor. A map of Q_{col} can then be achieved using the expression:

$$Q_{col} = 1 - \left(\frac{\mathrm{PL_{SC}}}{\mathrm{PL_{OC}}}\right)^{\frac{1}{n}},$$

where PL_{OC} and PL_{SC} are the photoluminescence at the open-circuit and short-circuit conditions, respectively. For each measurement, the illumination was held for 30s before measurement to allow for the PL to stabilize.

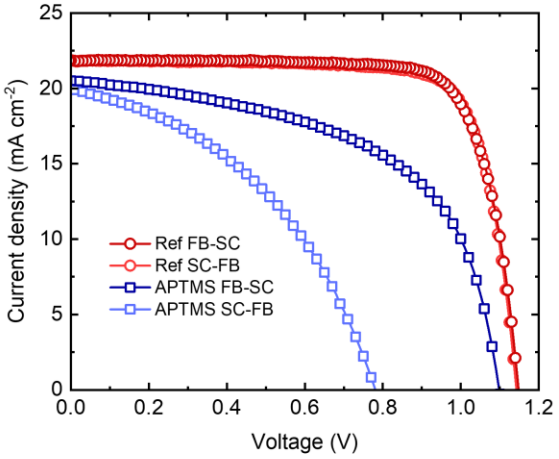

Surface treatment	V_{OC} (V)	J_{SC} (mA cm^{-2})	FF (%)	PCE (%)
Ref_{FB-SC}	1.15	21.9	77.7	19.5
Ref_{SC-FB}	1.14	21.9	77.9	19.5

Surface treatment	V_{OC} (V)	J_{SC} (mA cm^{-2})	FF (%)	PCE (%)
$APTMS_{FB-SC}$	1.10	20.5	55.4	12.5
$APTMS_{SC-FB}$	0.78	20.0	41.7	6.5

Fig. S1. Current density and voltage characteristics of a set of p-i-n perovskite solar cells with the APTMS treatment and without the treatment (i.e., Ref).

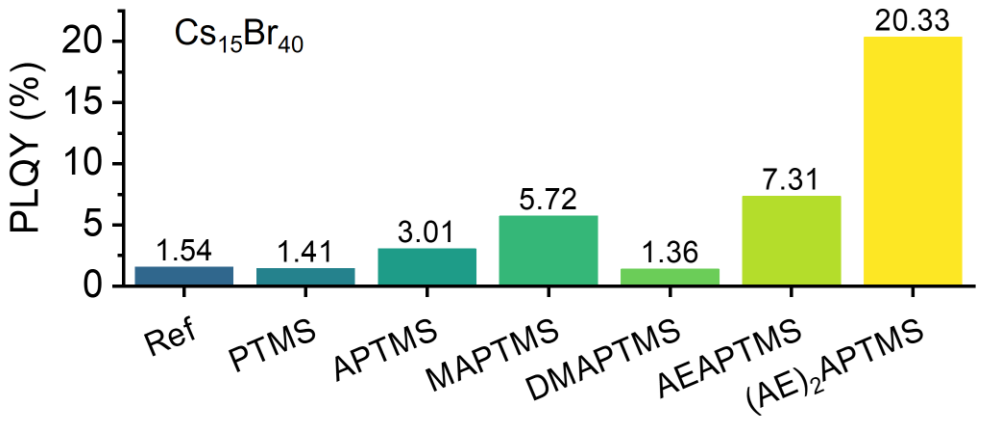

Fig. S2. PLQY for $Cs_{15}Br_{40}$ with amino-silane molecules and without any treatments (i.e., Ref).

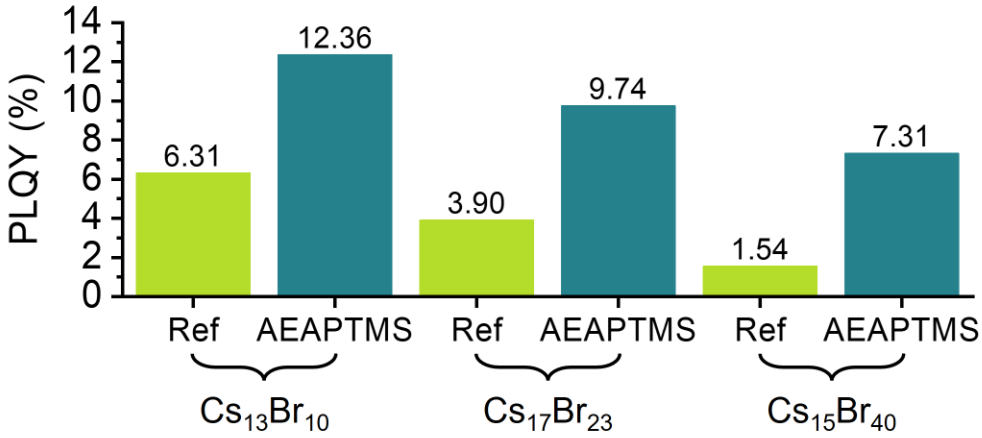

Fig. S3. PLQY for the perovskite compositions of $Cs_{13}Br_{10}$, $Cs_{17}Br_{23}$, and $Cs_{15}Br_{40}$ with and without the AEAPTMS treatment.

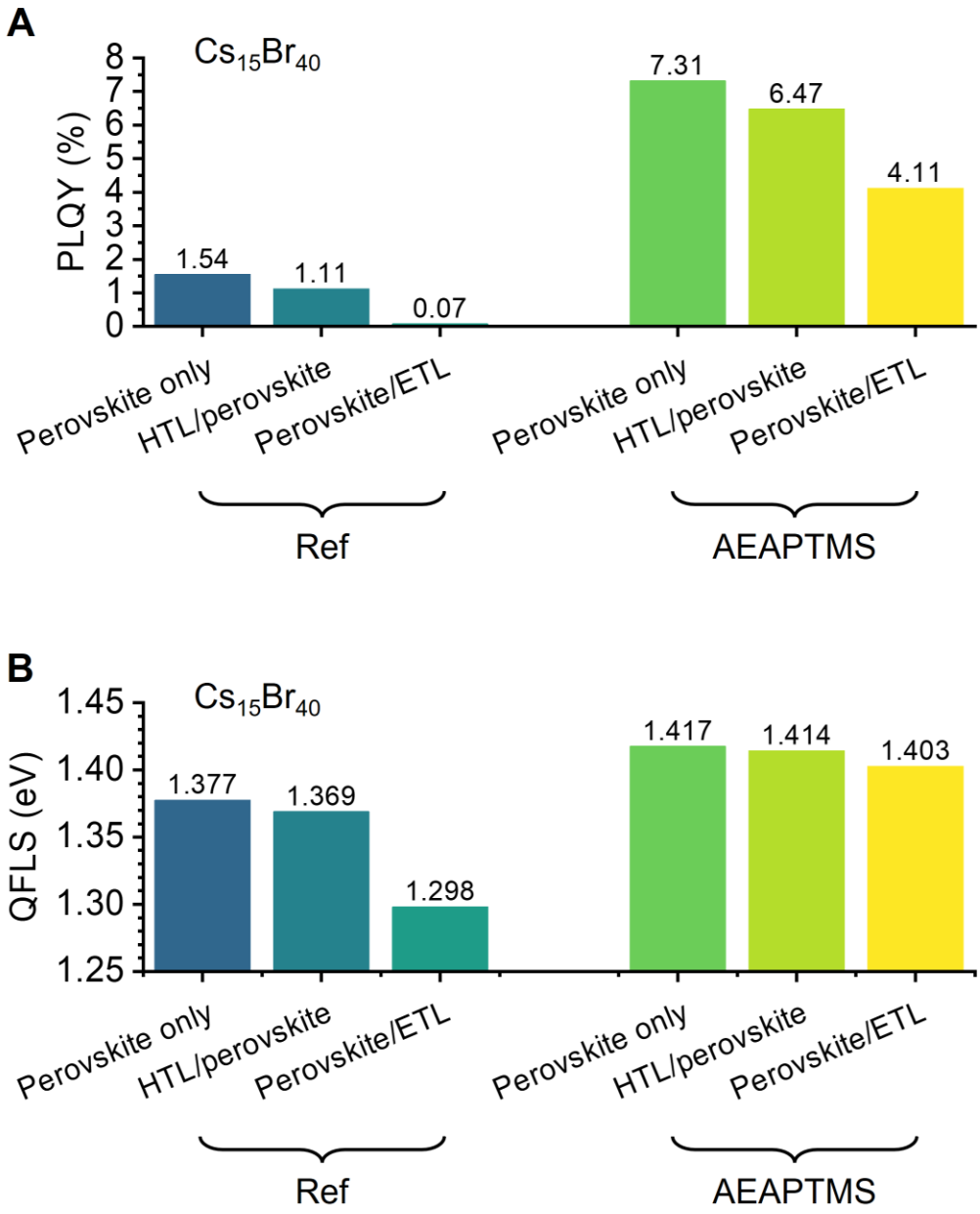

Fig. S4. (**A** and **B**) PLQY (A) and corresponding QFLS (*31*) (B) for $Cs_{15}Br_{40}$ with and without the AEAPTMS treatment processed on perovskite only, on top of the HTL/perovskite stack, or in-between perovskite and ETL (i.e., perovskite/ETL). All the treatments are processed on the top surface of perovskite.

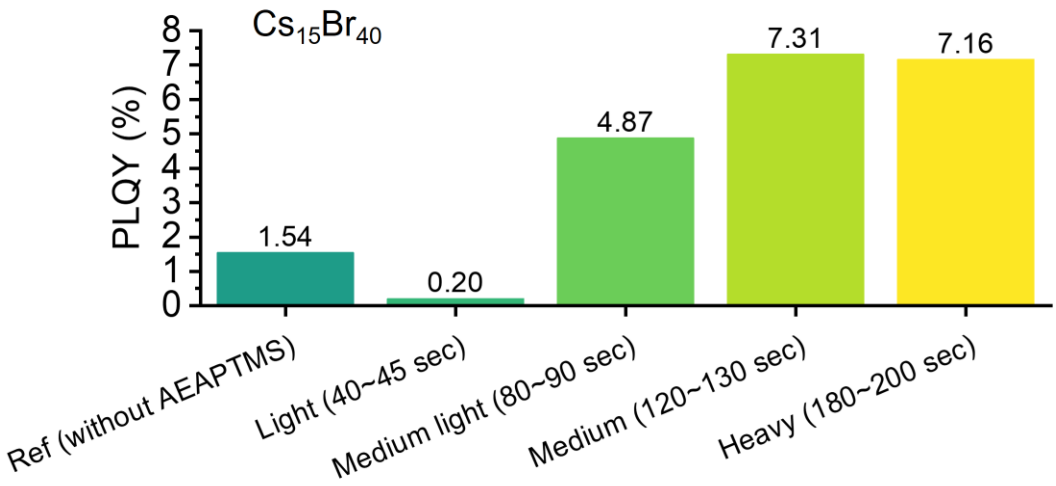

Fig. S5. PLQY measured for $Cs_{15}Br_{40}$ with and without the AEAPTMS treatment and processed for different treatment durations.

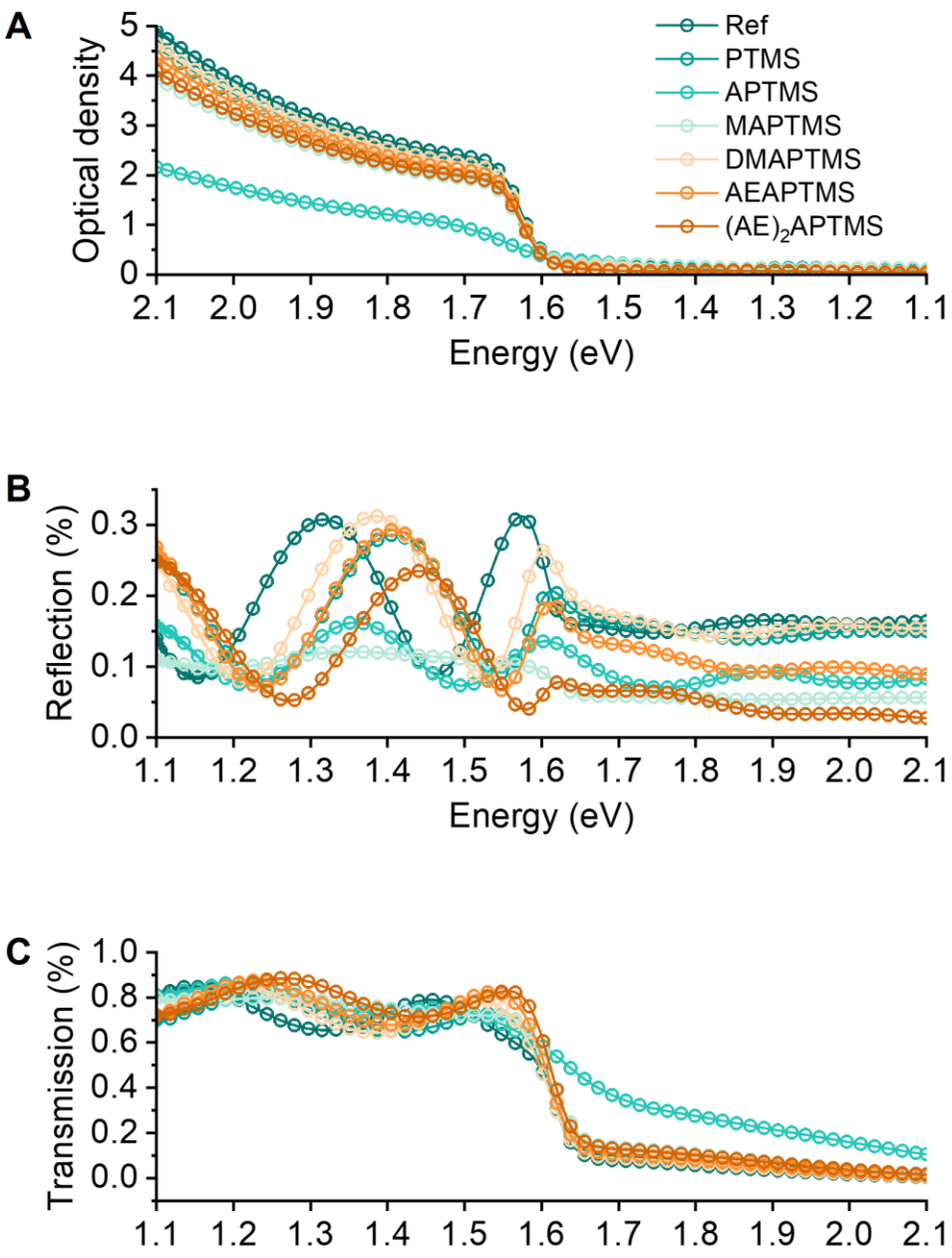

Fig. S6. (**A** to **C**) Optical density (A), reflection (B), and transmission (C) of $Cs_{13}Br_{10}$ treated with and without amino-silane molecules.

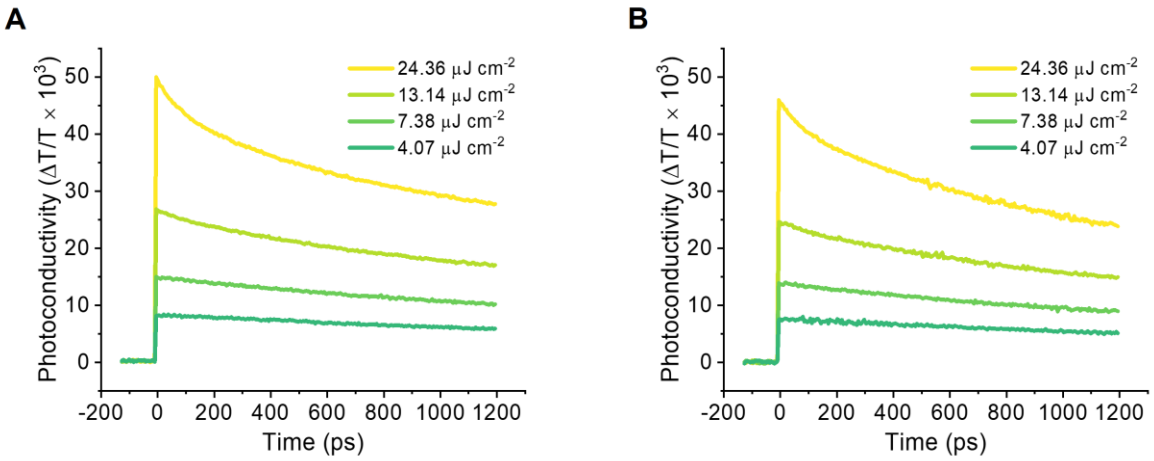

Fig. S7. (**A** and **B**) THz conductivity measurements conducted for two sets of reference $Cs_{13}Br_{10}$ films.

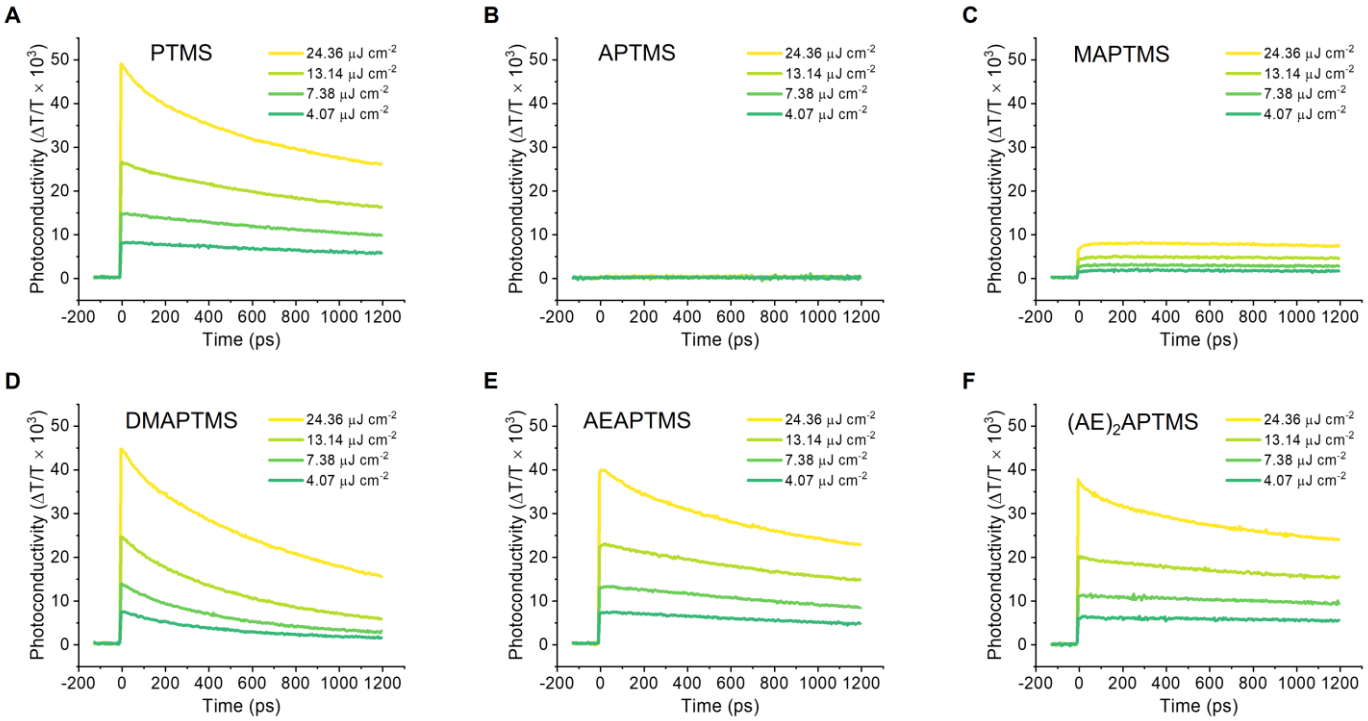

Fig. S8. THz conductivity measurements conducted for $Cs_{13}Br_{10}$ when treated with different amino-silane molecules and a silane molecule.

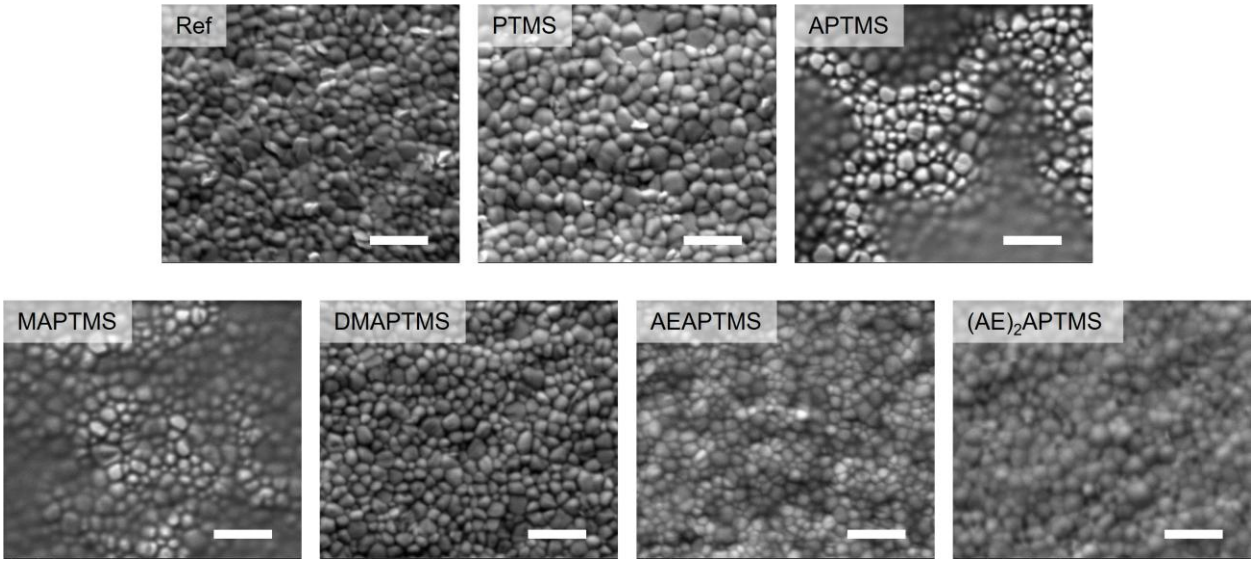

Fig. S9. SEM measurements conducted for $Cs_{13}Br_{10}$ with and without amino-silane molecule treatments. Scale bar = 1 µm.

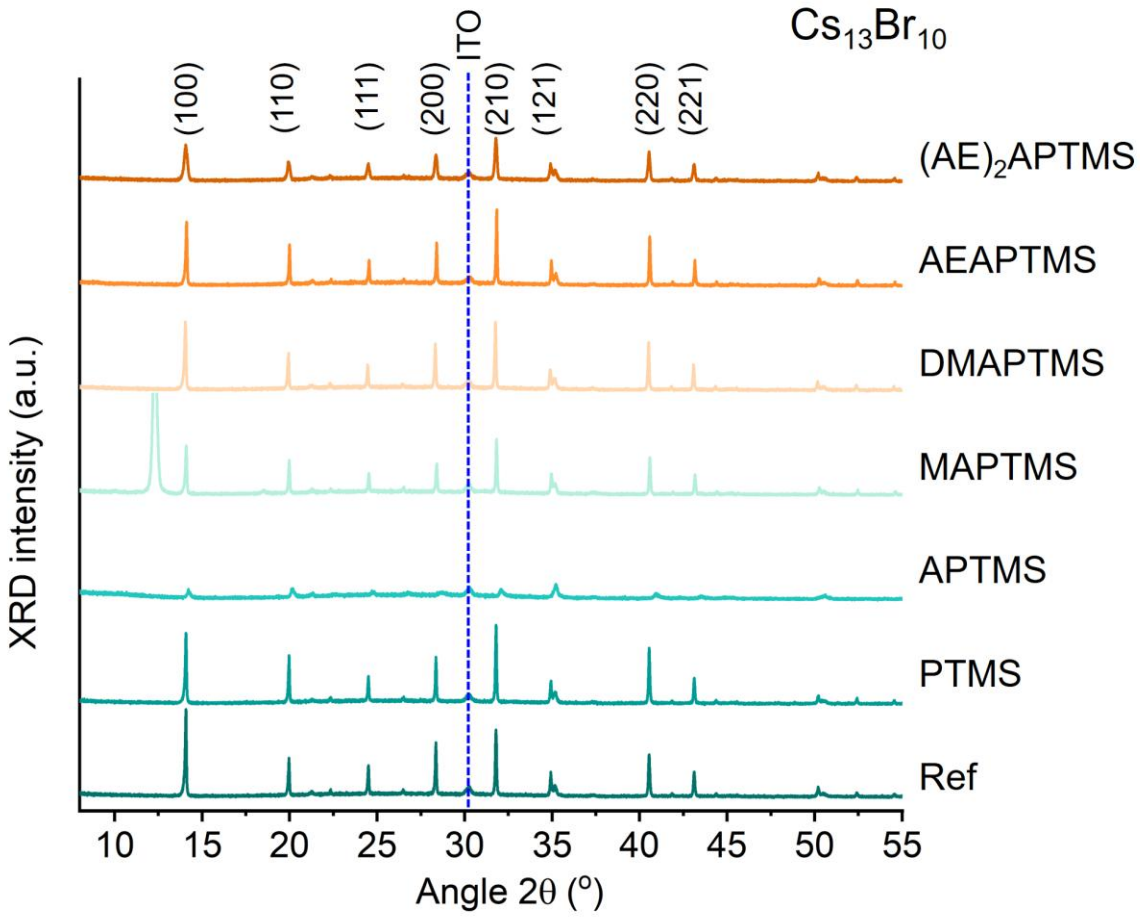

Fig. S10. XRD series for the ref and amino-silane molecule treated $Cs_{13}Br_{10}$ perovskite films, prepared on ITO glass substrates.

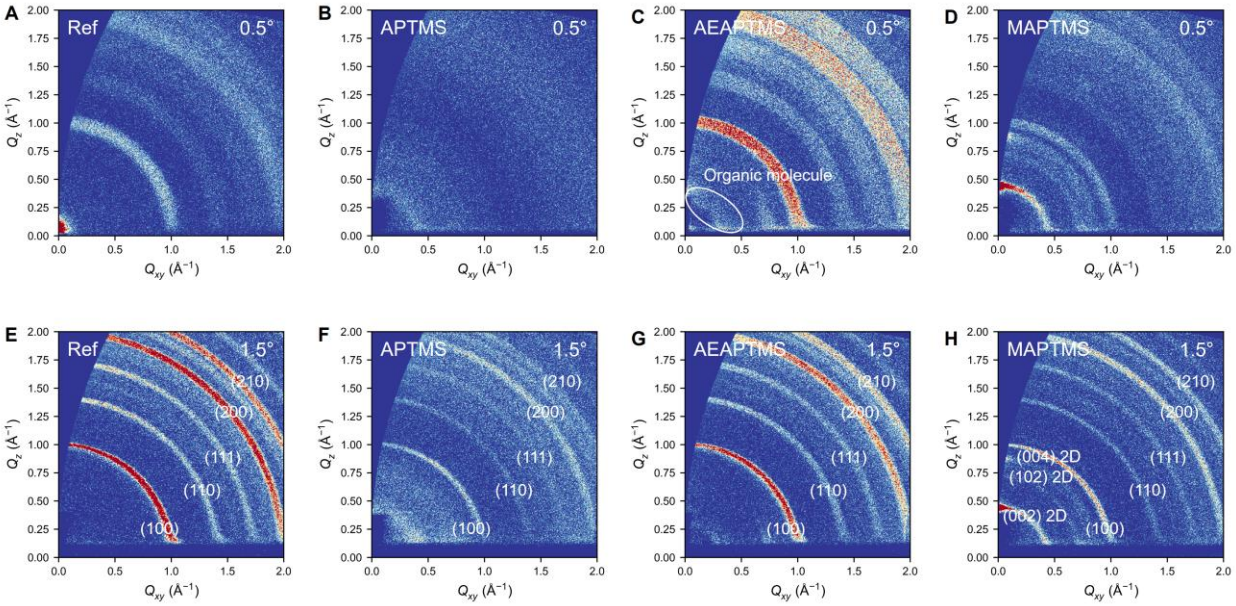

Fig. S11. (**A** to **H**) GIWAXS patterns of (A) reference, (B) APTMS, (C) AEAPTMS and (D) MAPTMS perovskite films obtained at incident angles of 0.5° while their corresponding GIWAXS patterns obtained at 1.5° are shown in (E), (F), (G), and (H), respectively.

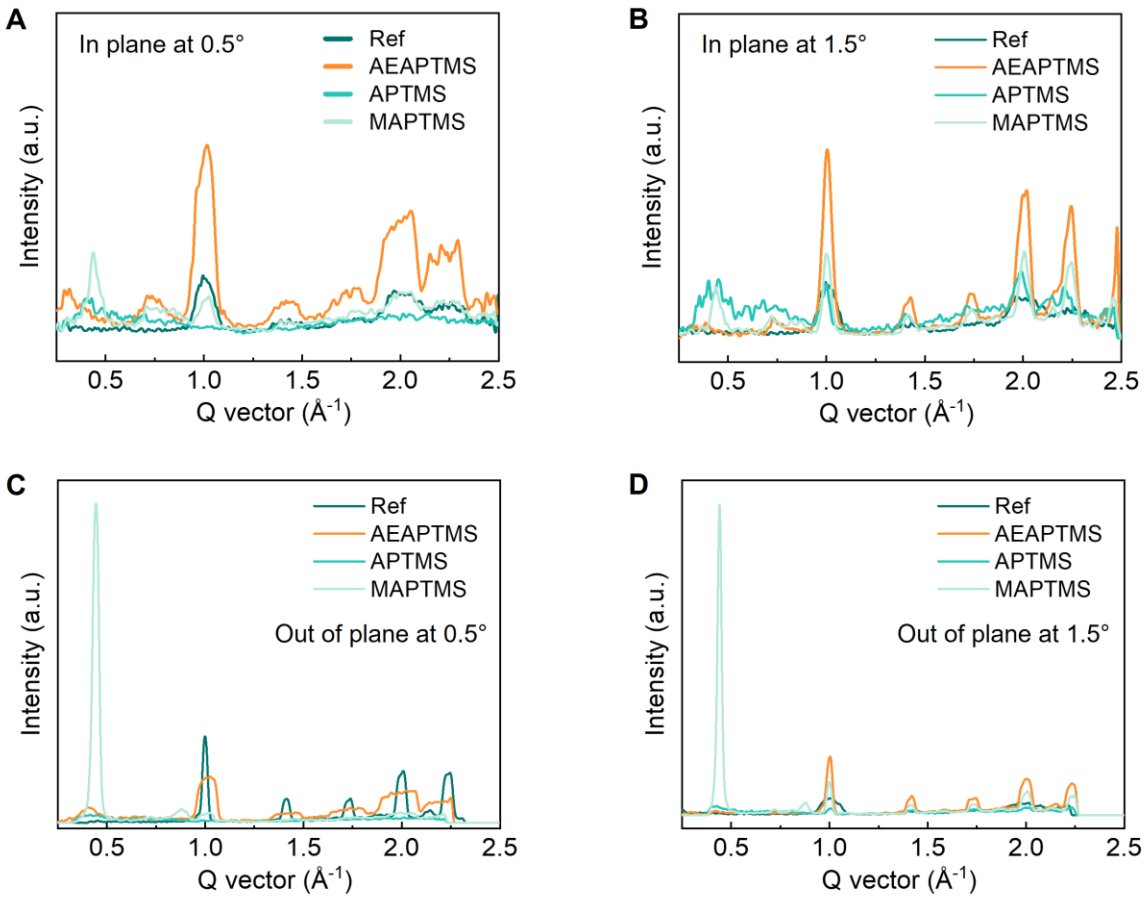

Fig. S12. (**A** to **D**) GIWAXS patterns corresponding to fig. S11. are presented in the in-plane and out-of-plane directions. (A) and (C) show the 1D integrated GIWAXS from the 2D patterns in the in-plane and out-of-plane directions, respectively, at the incident angle of 0.5°. The AEAPTMS treatment results in a change of the preferential orientation from the out-of-plane to in-plane directions, as compared to the reference sample. (B) and (D) are the results when a 1.5° incident angle was applied. The AEAPTMS-treated sample shows higher crystallinity in both directions. The APTMS-treated sample exhibits much weaker signals within the attenuation length (~ 250 nm). Strong 2D phase peaks appear in the MAPTMS-treated sample at both the 0.5° and 1.5° incident angles, whilst the 3D perovskite peaks show no traceable signals, indicating a transition from 3D to 2D phases occurred.

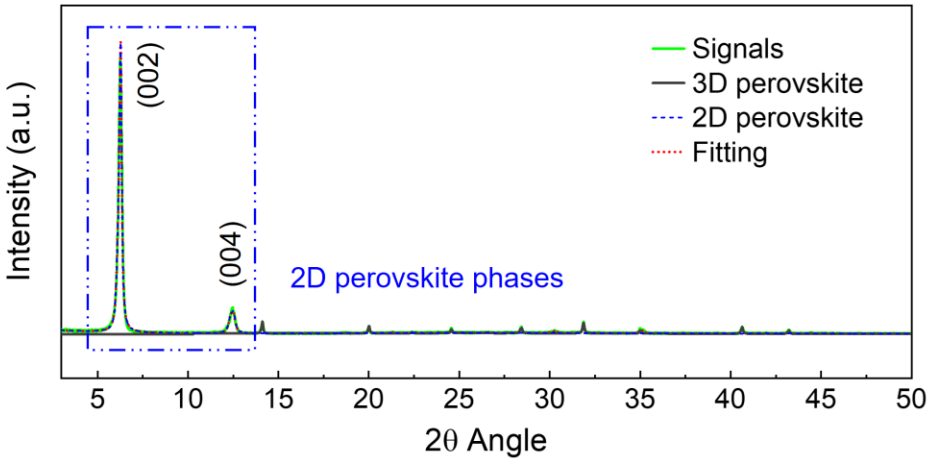

Fig. S13. 2D perovskite phases formed on $Cs_{13}Br_{10}$ when treated with the MAPTMS molecule. The fitting lattice parameter is based on one-layer Ruddlesden-Popper phases with Pbca space group (*74*). The fitting data shows these two peaks are from the (001) family face with high orientation based on the GIWAXS data from fig. S12.

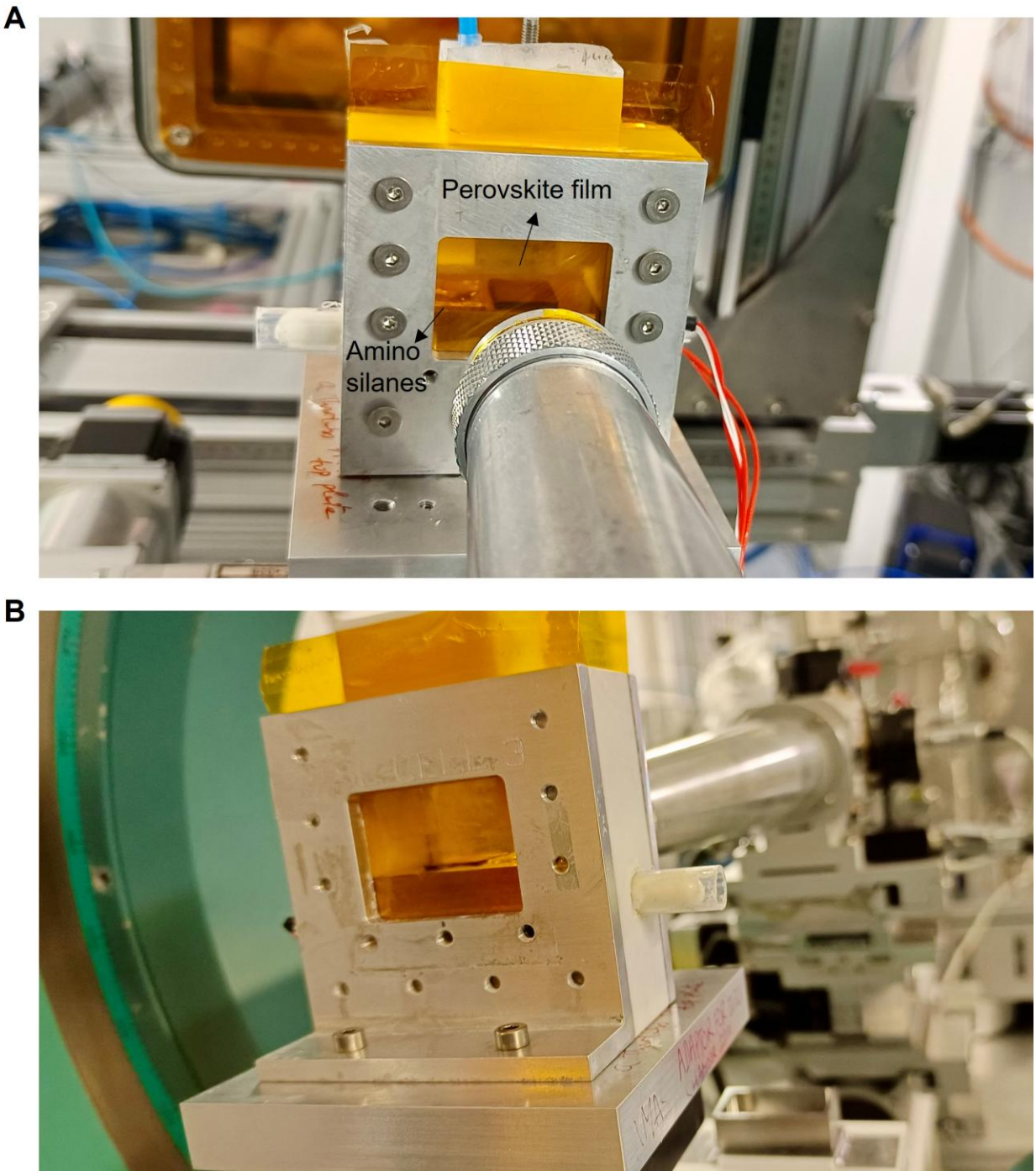

Fig. S14. (**A** and **B**) In-situ setup for monitoring the vapour-based amino-silane treatment on perovskite films at the European Synchrotron Radiation Facility (ESRF): front view (A) and rear view (B).

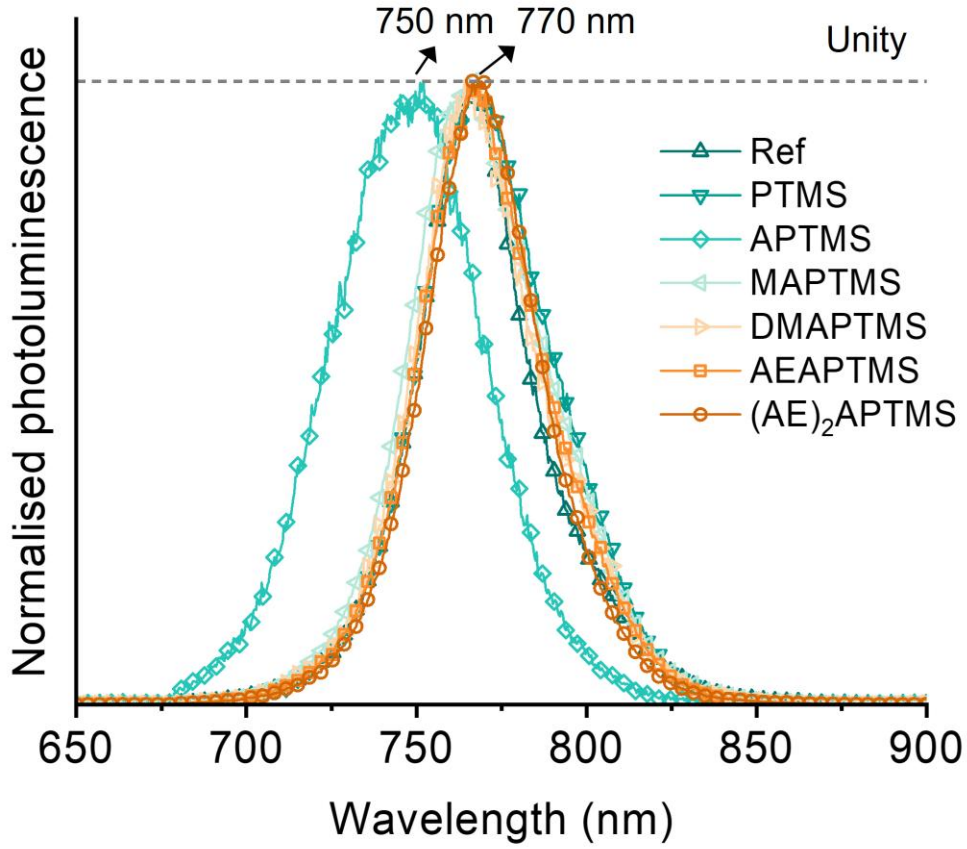

Fig. S15. Normalized photoluminescence measured from $Cs_{13}Br_{10}$ treated with and without amino-silane molecules different amino-silane molecules.

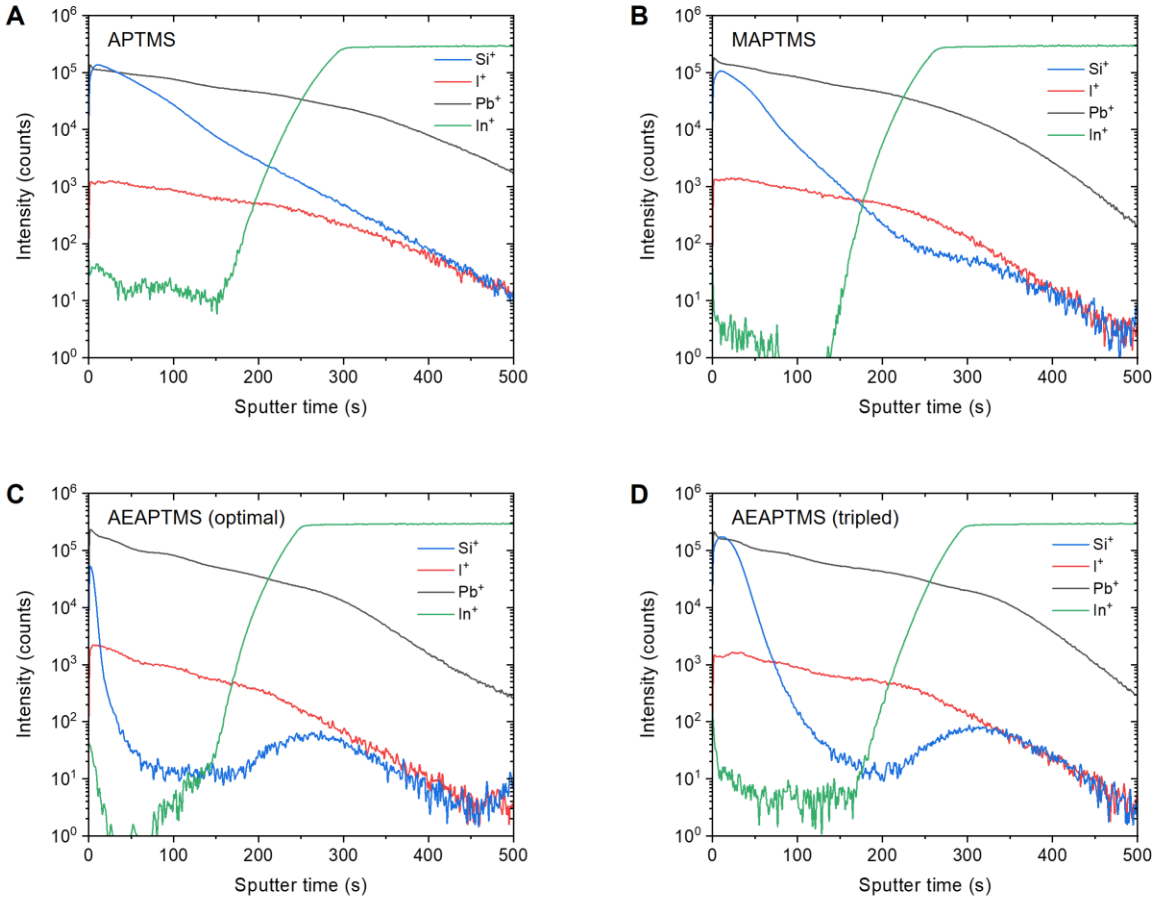

Fig. S16. (**A** to **D**) ToF-SIMS analyses for $Cs_{13}Br_{10}$ perovskites treated with APTMS (A), MAPTMS (B), AEAPTMS with the optimal duration (C), and AEAPTMS with a duration tripled relative to the optimal (D). The perovskite films were made on ITO-glass substrates.

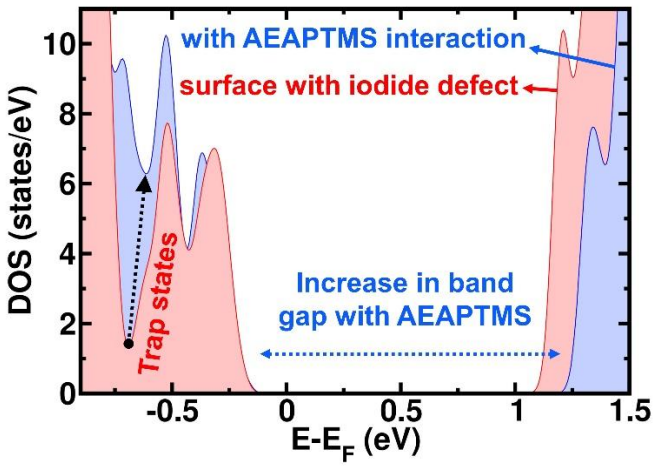

Fig. S17. Electronic density of states of the perovskite surface with an iodide vacancy defect before and after its interaction with the AEAPTMS molecule. A small increase in the band gap from 1.03 eV to 1.15 eV due to AEAPTMS-surface binding is found. Such broadening of the surface states signifies surface passivation effects. Trap like states below the valence band edge disappear upon interaction with AEAPTMS, again indicating the effective passivator role of AEAPTMS in eliminating these trap states and iodide vacancy defects through strong surface binding.

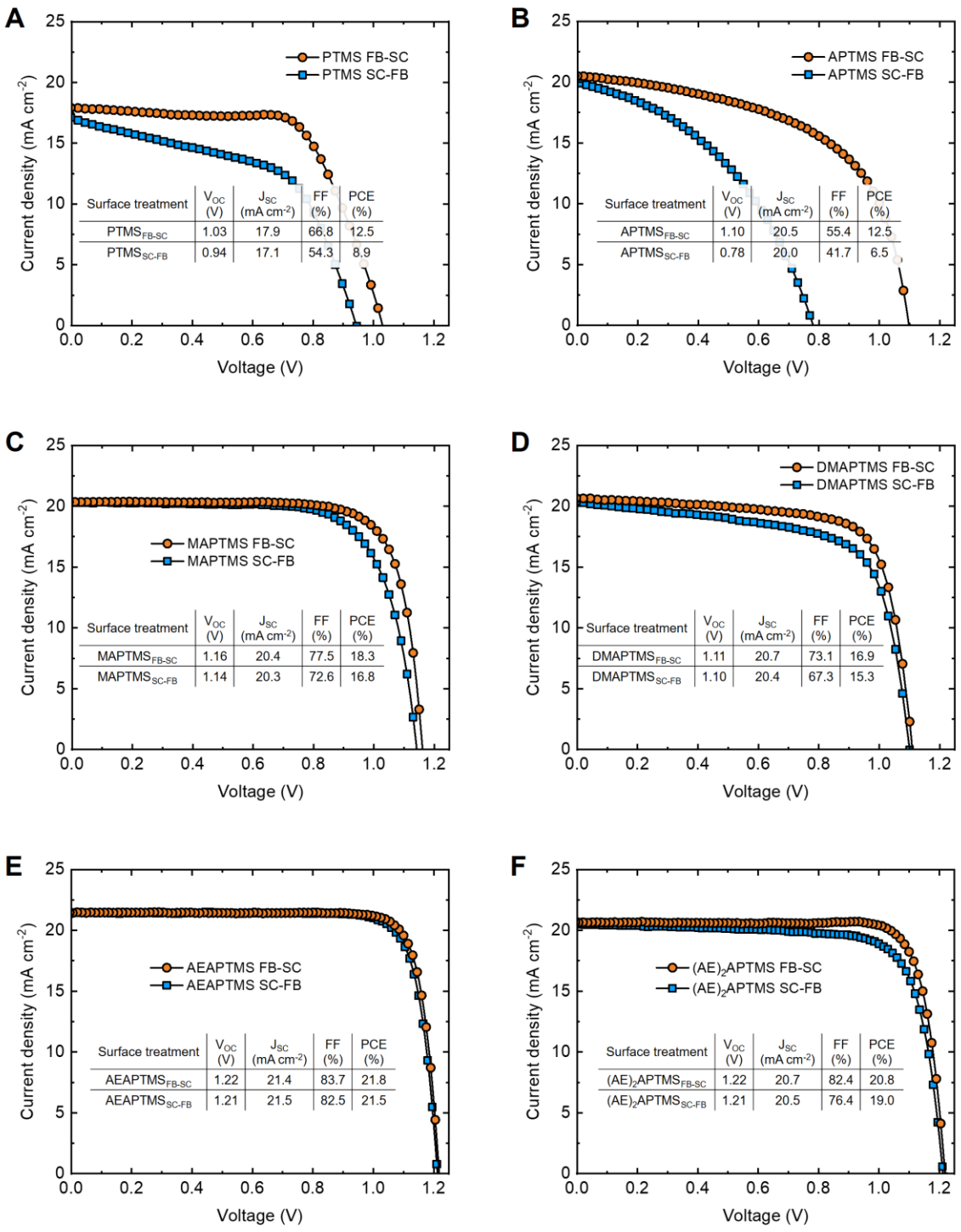

Fig. S18. (**A** to **F**) Current density and voltage characterizations conducted for $Cs_{13}Br_{10}$ with various amino-silane surface treatments: (A) PTMS, (B) APTMS, (C) MAPTMS, (D) DMAPTMS, (E) AEAPTMS, and (F) $(AE)_2$APTMS.

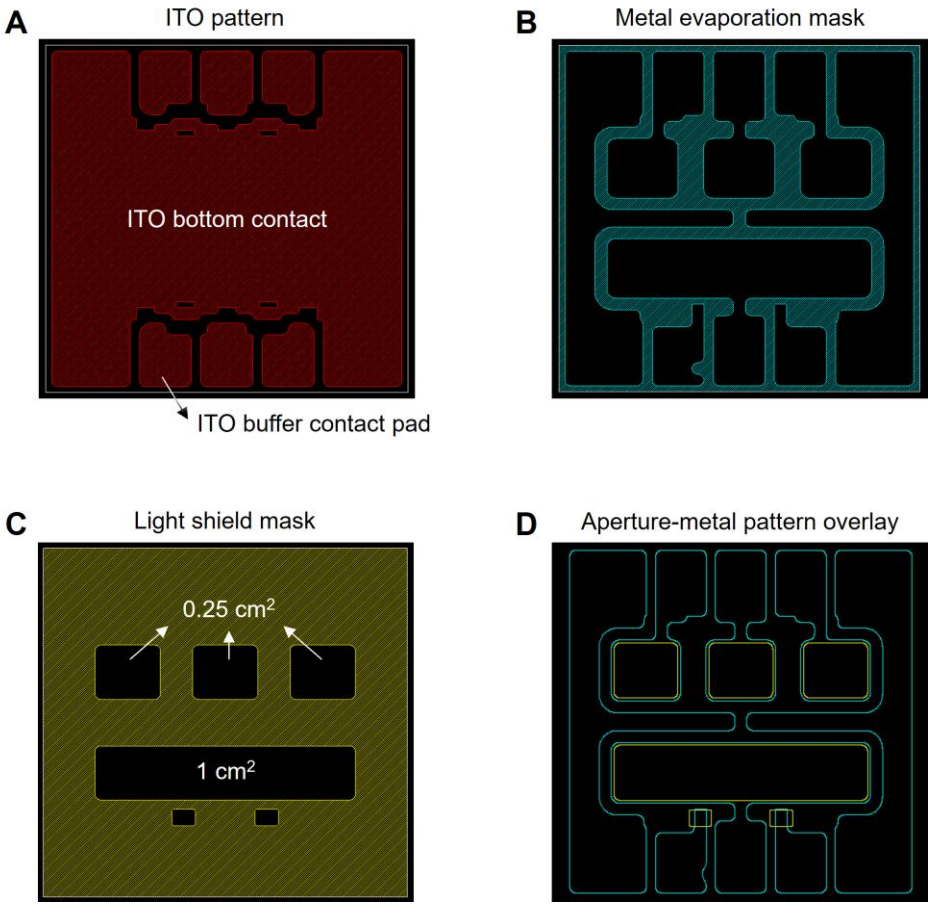

Fig. S19. (**A**) Illustration of the ITO pattern utilized in this study. The ITO bottom contact consists of a large, singular pad designed to interface with our p-i-n solar cell's hole transport layer. Each individual buffer contact pad is strategically placed to ensure reliable and consistent contact with the pogo pins that connect to the top metal contacts during long-term operational testing. (**B**) Metal evaporation mask used to define top metal contact geometry. (**C**) Light shield mask employed to delineate the apertures for the 0.25-cm^2 and 1-cm^2 cells. (**D**) Drawing of alignment of the aperture openings and top metal contact patterns. The dimensions of the top metal contact areas (excluding the connecting necks over active areas and the pogo pin contact points) measure 0.30 cm^2 and 1.13 cm^2 for the respective 0.25-cm^2 and 1-cm^2 aperture cells. These dimensions represent 113% and 120% overage relative to the corresponding aperture areas.

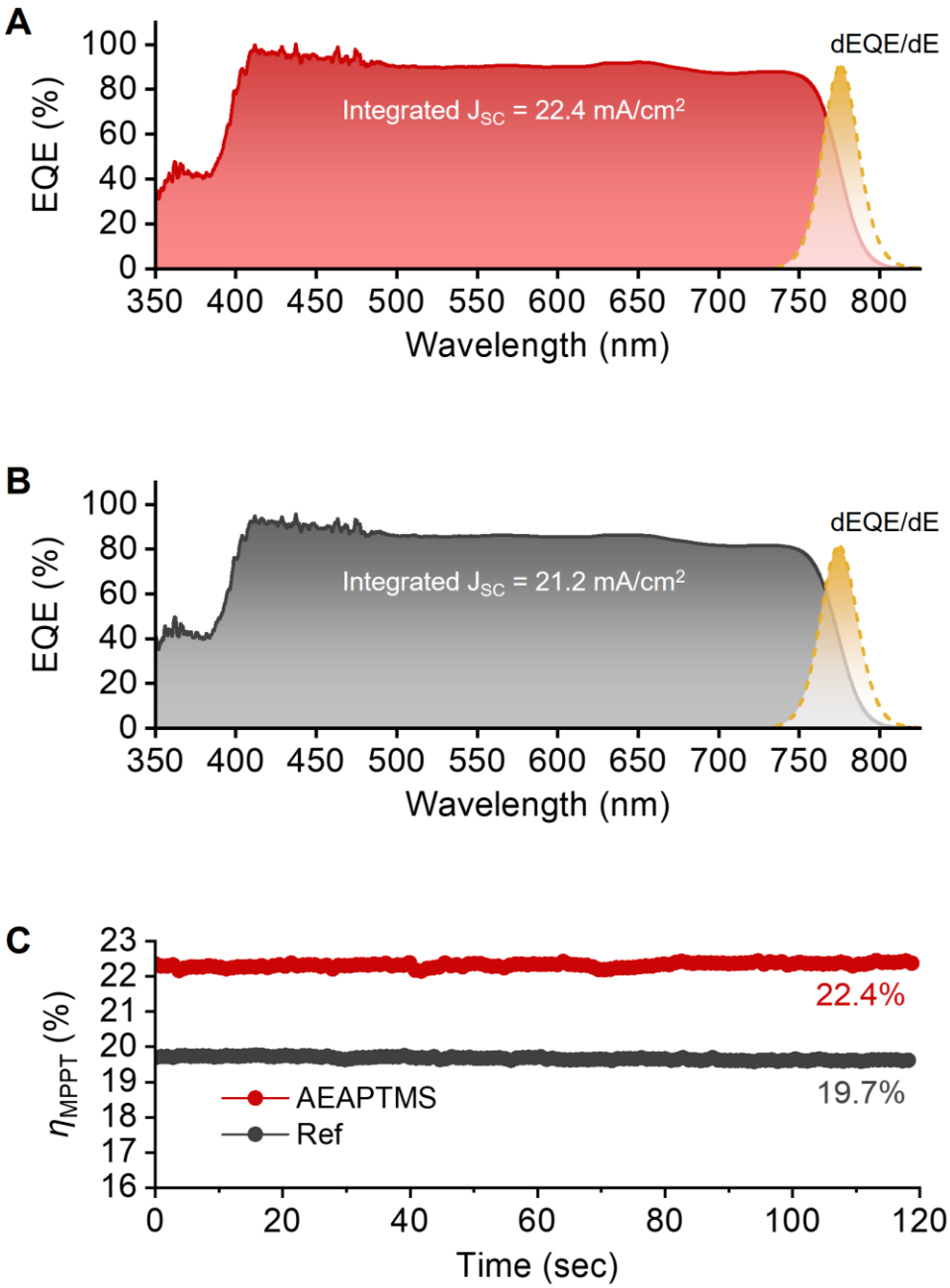

Fig. S20. (**A** and **B**) EQE spectra (solid line) with photocurrent integrated over the AM1.5 (100 mW cm^{-2}) solar spectrum and the first derivative of the corresponding EQE (dashed line, leading to an extracted bandgap value of 1.60 eV) for $Cs_{13}Br_{10}$ treated with the AEAPTMS molecule (A) and without the treatment (B), i.e., Ref. (**C**) Corresponding η_{MPPT} for AEAPTMS-based and reference cells measured over a time period of 120 seconds.

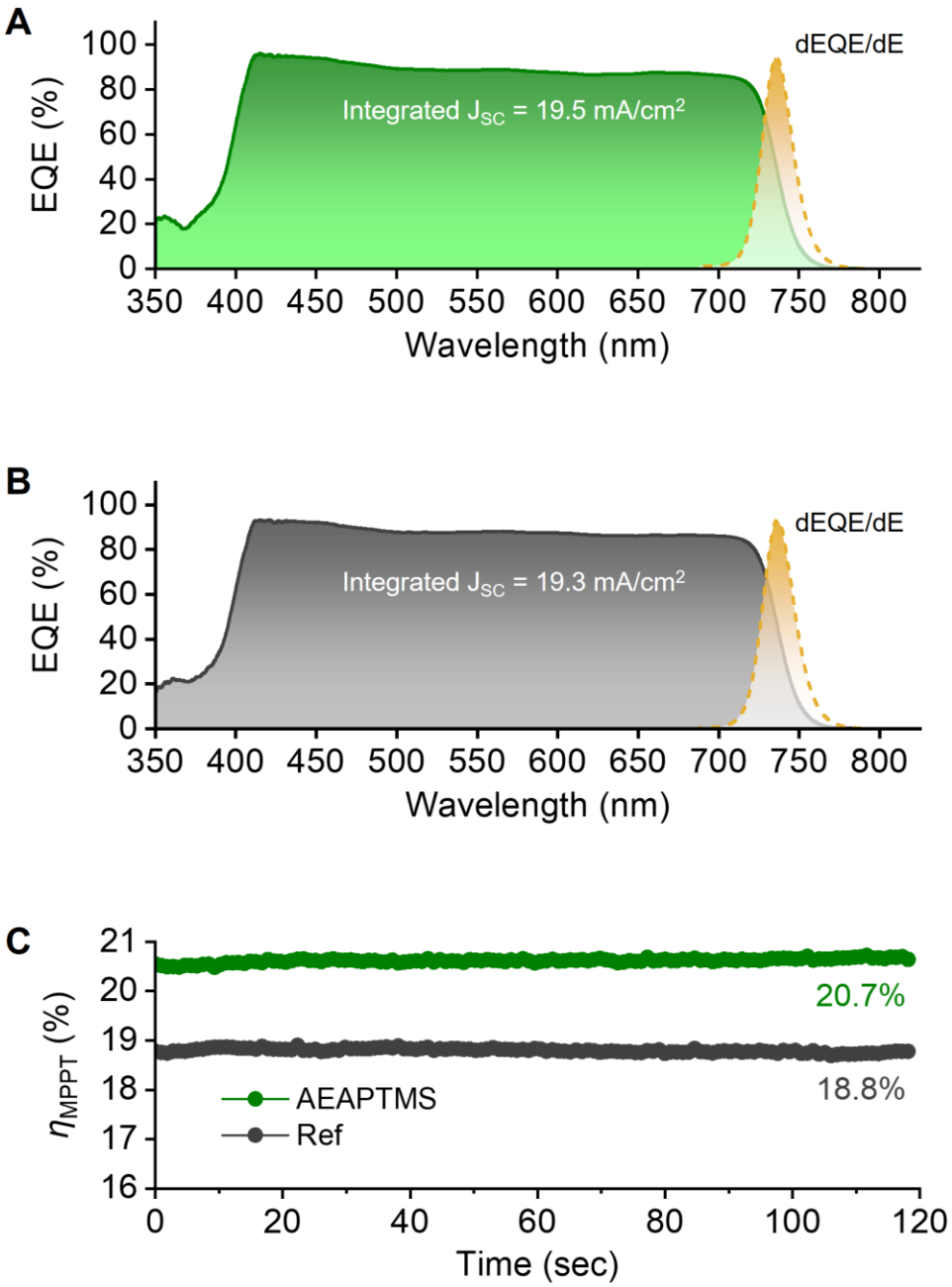

Fig. S21. (**A** and **B**) EQE spectra (solid line) with photocurrent integrated over the AM1.5 (100 mW cm^{-2}) solar spectrum and the first derivative of the corresponding EQE (dashed line, leading to an extracted bandgap value of 1.67 eV) for $Cs_{13}Br_{10}$ treated with the AEAPTMS molecule (A) and without the treatment (B), i.e., Ref. (**C**) Corresponding η_{MPPT} for AEAPTMS-based and reference cells measured over a time period of 120 seconds.

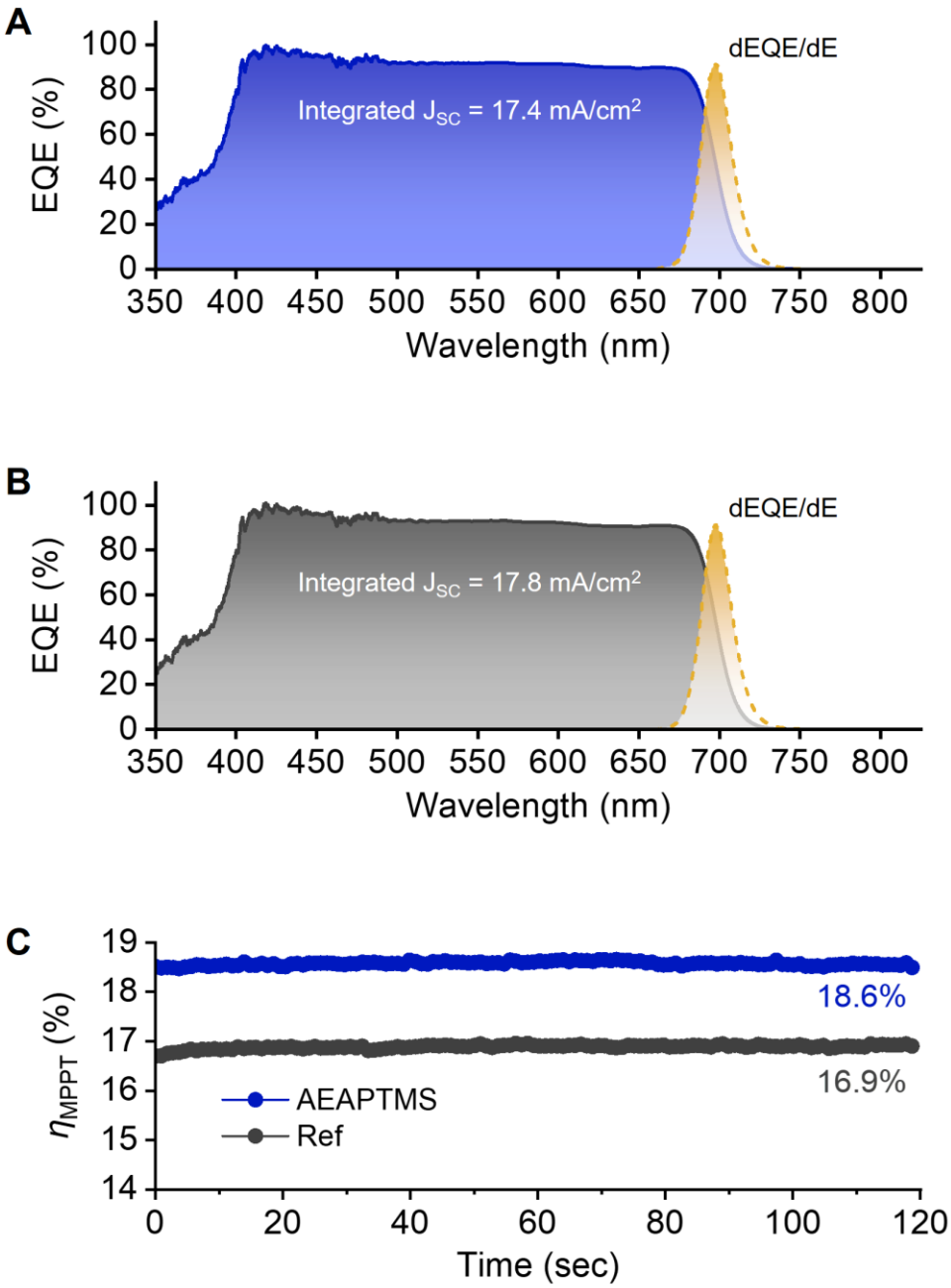

Fig. S22. (**A** and **B**) EQE spectra (solid line) with photocurrent integrated over the AM1.5 (100 mW cm^{-2}) solar spectrum and the first derivative of the corresponding EQE (dashed line, leading to an extracted bandgap value of 1.77 eV) for $Cs_{13}Br_{10}$ treated with the AEAPTMS molecule (A) and without the treatment (B), i.e., Ref. (**C**) Corresponding η_{MPPT} for AEAPTMS-based and reference cells measured over a time period of 120 seconds.

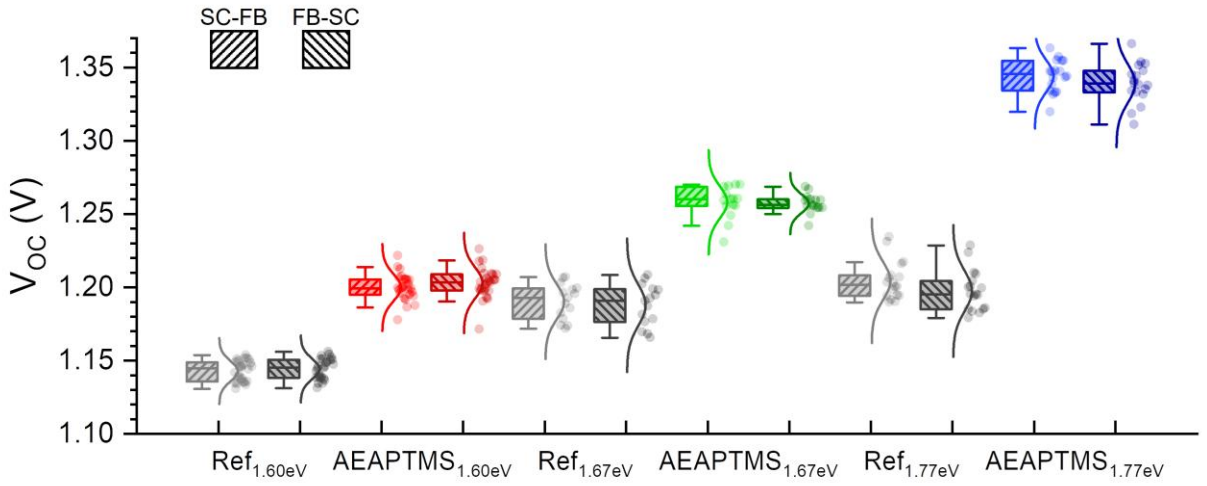

Fig. S23. Statistical results of V_{OC} obtained from SC-FB and FB-SC scans based on 0.25cm^2 solar cells using the perovskite compositions of $Cs_{13}Br_{10}$ (1.60 eV, 26 cells), $Cs_{17}Br_{23}$ (1.67 eV, 15 cells) and $Cs_{15}Br_{40}$ (1.77 eV, 18 cells) treated with the AEAPTMS molecule or without the treatment, i.e., Ref.

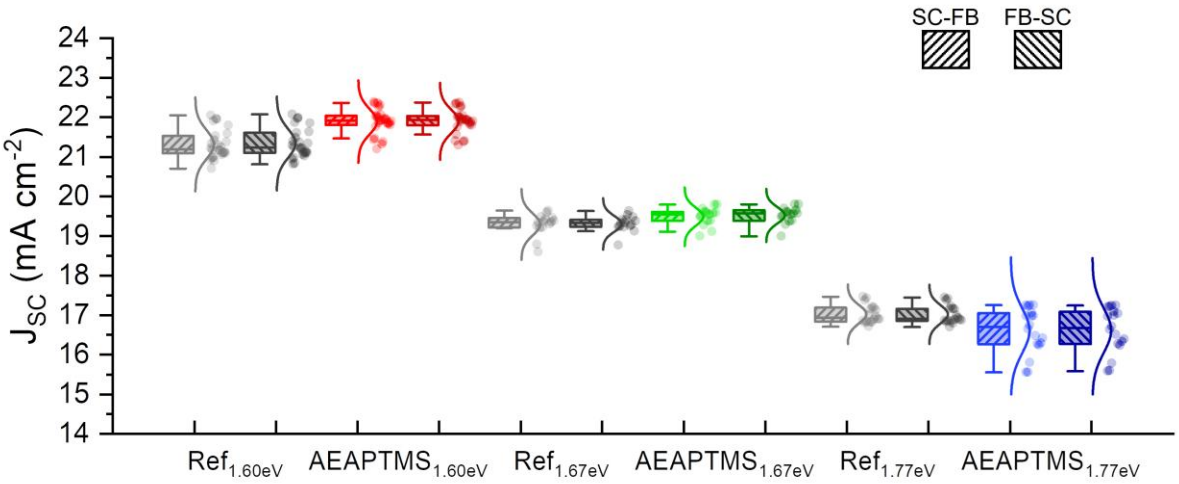

Fig. S24. Statistical results of J_{SC} obtained from SC-FB and FB-SC scans based on 0.25cm^2 solar cells using the perovskite compositions of $Cs_{13}Br_{10}$ (1.60 eV, 26 cells), $Cs_{17}Br_{23}$ (1.67 eV, 15 cells) and $Cs_{15}Br_{40}$ (1.77 eV, 18 cells) treated with the AEAPTMS molecule or without the treatment, i.e., Ref.

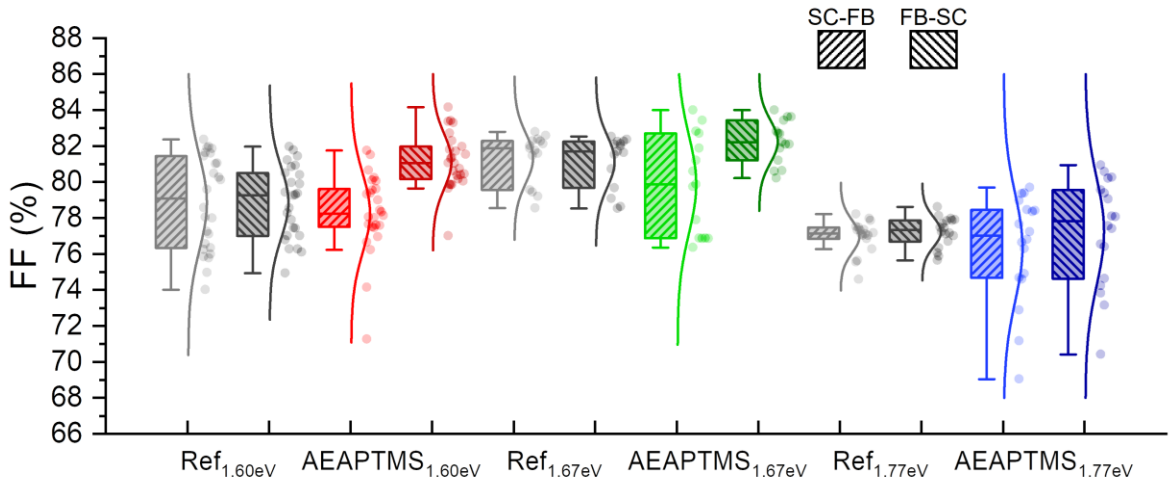

Fig. S25. Statistical results of FF obtained from SC-FB and FB-SC scans based on 0.25cm^2 solar cells using the perovskite compositions of $Cs_{13}Br_{10}$ (1.60 eV, 26 cells), $Cs_{17}Br_{23}$ (1.67 eV, 15 cells) and $Cs_{15}Br_{40}$ (1.77 eV, 18 cells) treated with the AEAPTMS molecule or without the treatment, i.e., Ref.

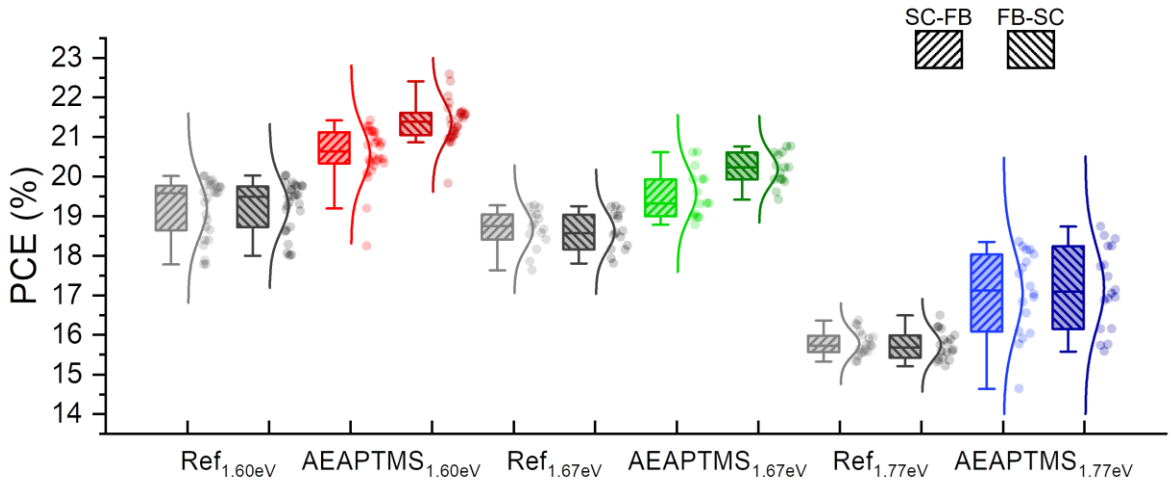

Fig. S26. Statistical results of PCE obtained from SC-FB and FB-SC scans based on 0.25cm^2 solar cells using the perovskite compositions of $Cs_{13}Br_{10}$ (1.60 eV, 26 cells), $Cs_{17}Br_{23}$ (1.67 eV, 15 cells) and $Cs_{15}Br_{40}$ (1.77 eV, 18 cells) treated with the AEAPTMS molecule or without the treatment, i.e., Ref.

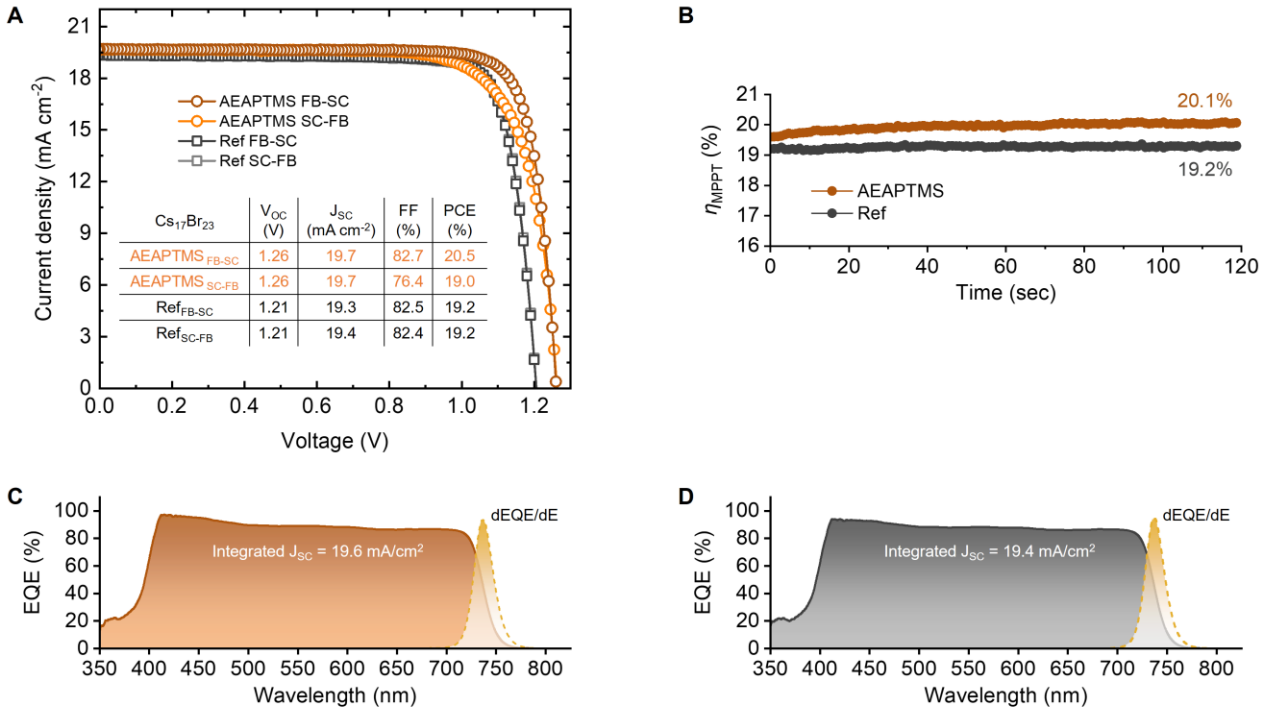

Fig. S27. (**A** to **D**) Current density and voltage characterisation (A) and corresponding η_{MPPT} for a time period of 120 seconds (B) conducted for 0.25-cm^2 $Cs_{13}Br_{10}$ solar cells using evaporated C_{60} and BCP and treated with and without the AEAPTMS molecule. EQE spectra (solid line) with photocurrent integrated over the AM1.5 (100 mW cm^{-2}) solar spectrum and the first derivative of the corresponding EQE (dashed line, leading to an extracted bandgap value of 1.67 eV) shown in (C) and (D) for cells with and without the AEAPTMS treatment, respectively

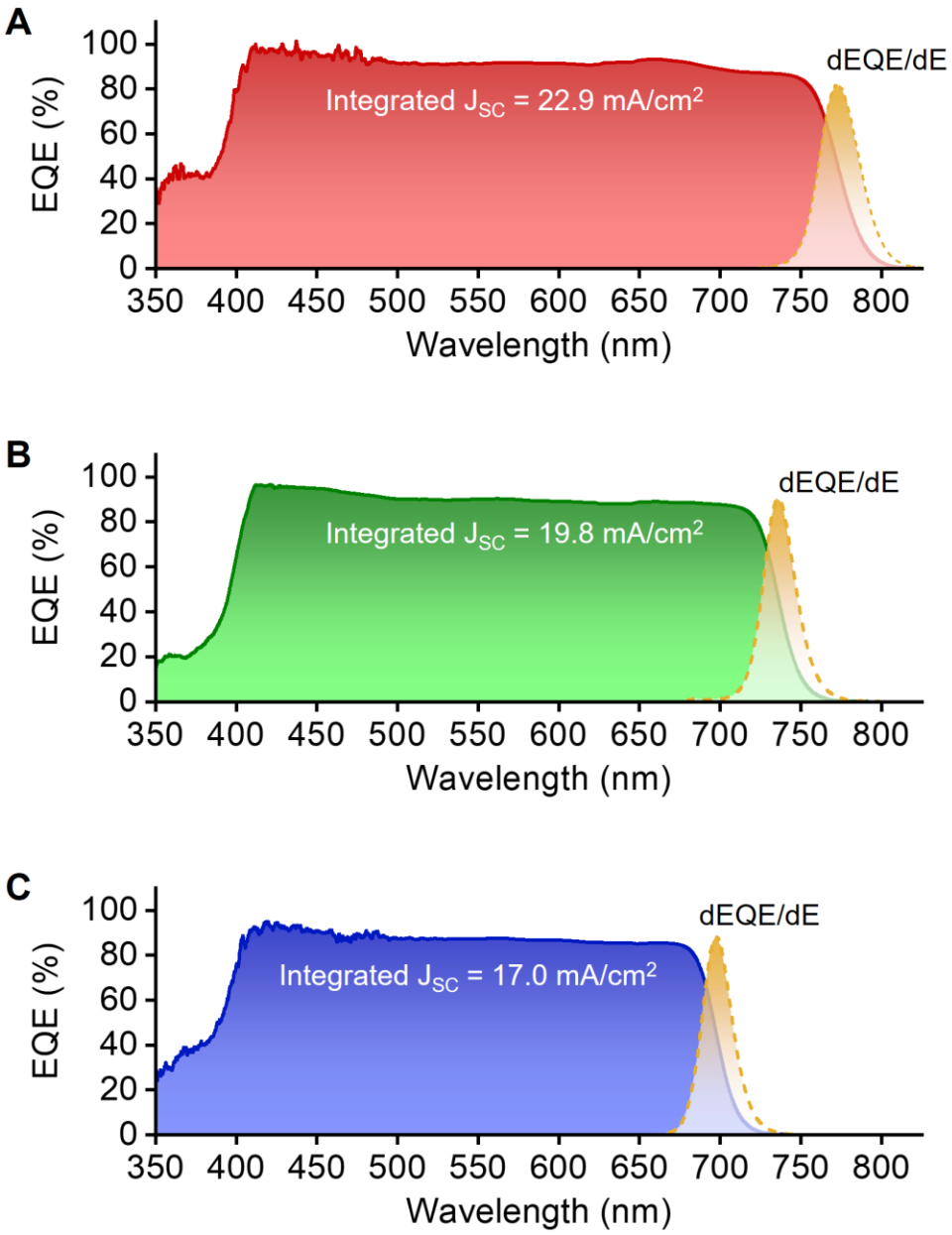

Fig. S28. (**A** to **C**) EQE spectra (solid line) with photocurrent integrated over the AM1.5 (100 mW cm^{-2}) solar spectrum and the first derivative of the corresponding EQE (dashed line), leading to an extracted bandgap value of 1.60 (A), 1.67 (B), and 1.77 eV (C) for 1-cm^2 cells treated with and without the AEAPTMS molecule.

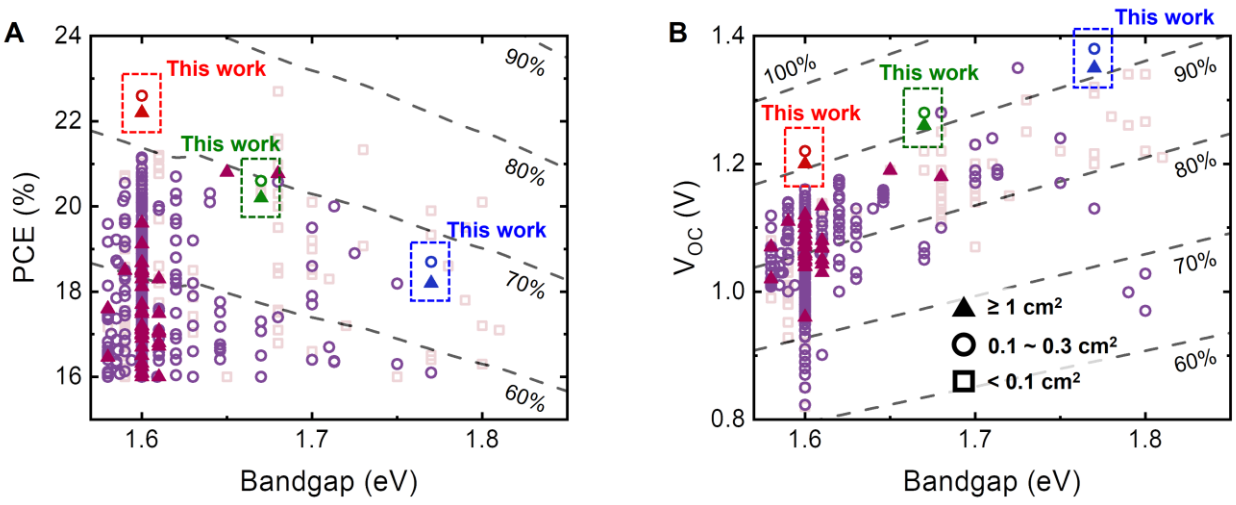

Fig. S29. PCE-bandgap and V_{OC}-bandgap literature data comparisons. Data points are presented with different symbols according to their active pixel areas: squares for pixel areas < 0.1 cm^2 (totaling 837 literature data points); circles for pixel areas between 0.1 and 0.3 cm^2 (totaling 802 literature data points); triangles for pixel areas ≥ 1.0 cm^2 (totaling 41 literature data points). Dashed lines indicate the percentages of the detailed balance limits (e.g., 90%, 80%, etc.). Our representative 0.25-cm^2 and 1-cm^2 cells with bandgaps of 1.6 eV, 1.67 eV, and 1.77 eV are marked as red, green, and blue, respectively, and are circled by dashed boxes. All the data were extracted from the reverse scans from the operation of their respective cells (in a p-i-n configuration), as reported in an open-access database (*75*) and manual literature searches as of January 2024.

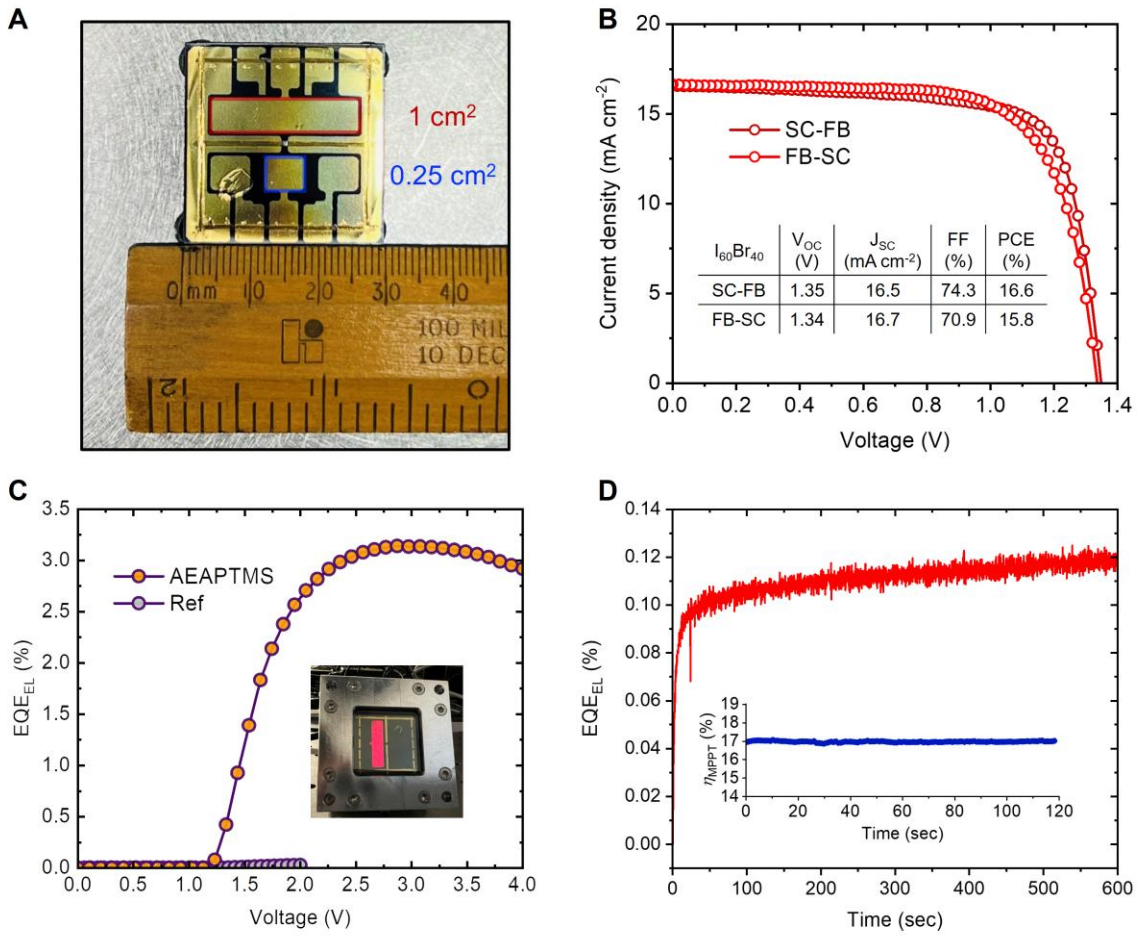

Fig. S30. (**A**) Photo of the solar cell design used in this study. (**B**) Corresponding current density and voltage characteristics of 1-cm^2 AEAPTMS-treated $Cs_{15}Br_{40}$ cell shown in (A). (**C** and **D**) Corresponding EQE_{EL} obtained (C) under the operation of a voltage sweep between 0 and 4 V and (D) recorded for 600 seconds, obtained by injecting the same cell (B) at the current density of 17 mA cm^{-2}. In (C), the EQE_{EL} of a reference solar cell (Ref) is also shown for comparison. Insets of (C) and (D) show the corresponding photo of the cell's illumination at the current density of 17 mA cm^{-2} and η_{MPPT} for 120 seconds, respectively.

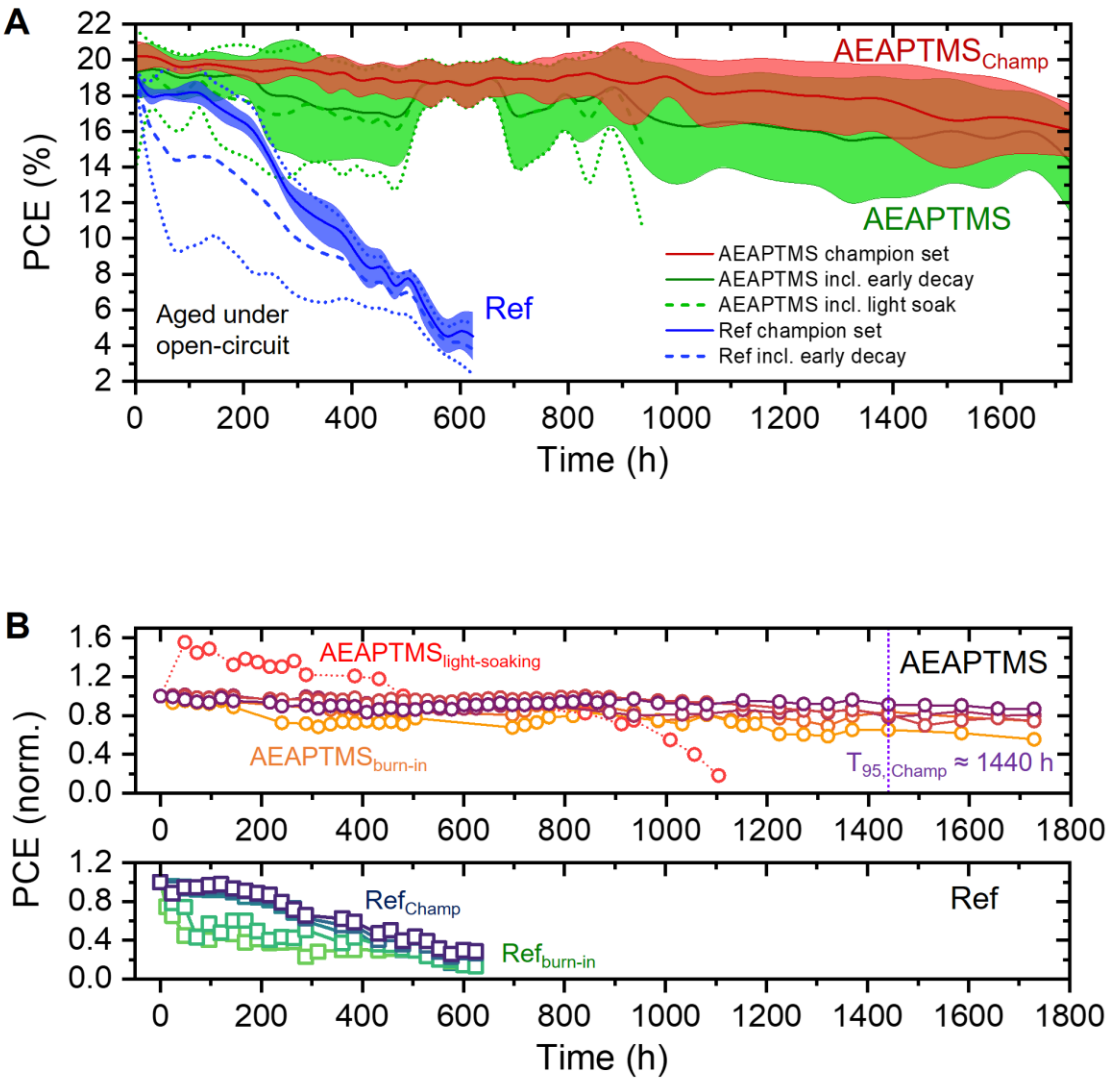

Fig. S31. (**A**) Evolution of mean PCE (with the corresponding standard deviations in a band plot) of encapsulated AEAPTMS-treated and reference $Cs_{13}Br_{10}$ cells (including six AEAPTMS-based and five reference cells) aged under the open-circuit condition and full-spectrum simulated sunlight at 85 °C in ambient air with relative humidity in the laboratory 50 ~ 60%. The datasets including some solar cells with distinct degradation pathways, i.e., light-soaking and burn-in, are explicitly indicated. (**B**) Evolution of normalised PCE for individual cells used and recorded for (A). For the champion AEAPTMS-treated cell, the time taken to reach 95% of its initial MPP ($T_{95,\ Champ}$) is approximately 1,440 hours.

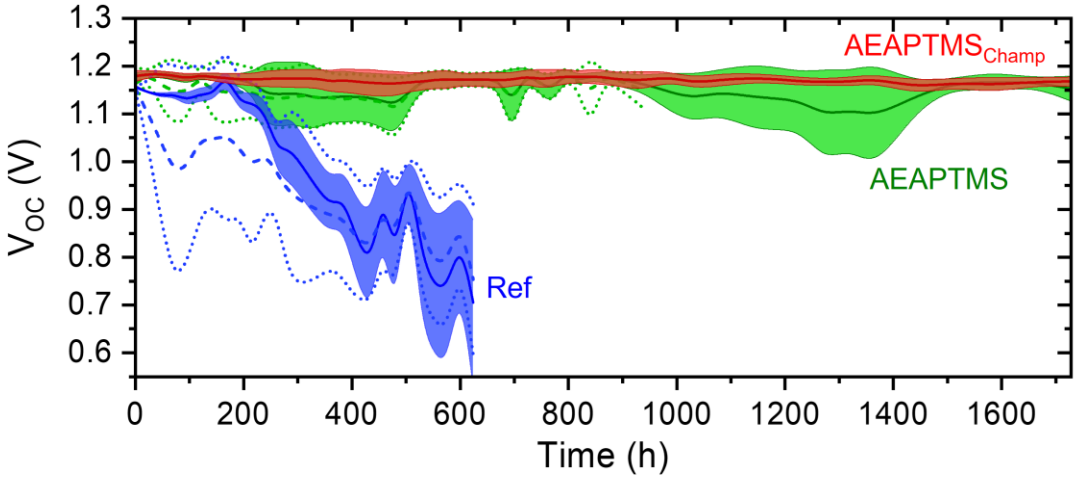

Fig. S32. Evolution of mean V_{OC} (with the corresponding standard deviations in a band plot) of encapsulated AEAPTMS-treated and reference $Cs_{13}Br_{10}$ cells (including six AEAPTMS-based and five reference cells) aged under the open-circuit condition and full-spectrum simulated sunlight at 85 ℃ in ambient air with relative humidity in the laboratory 50 ~ 60%.

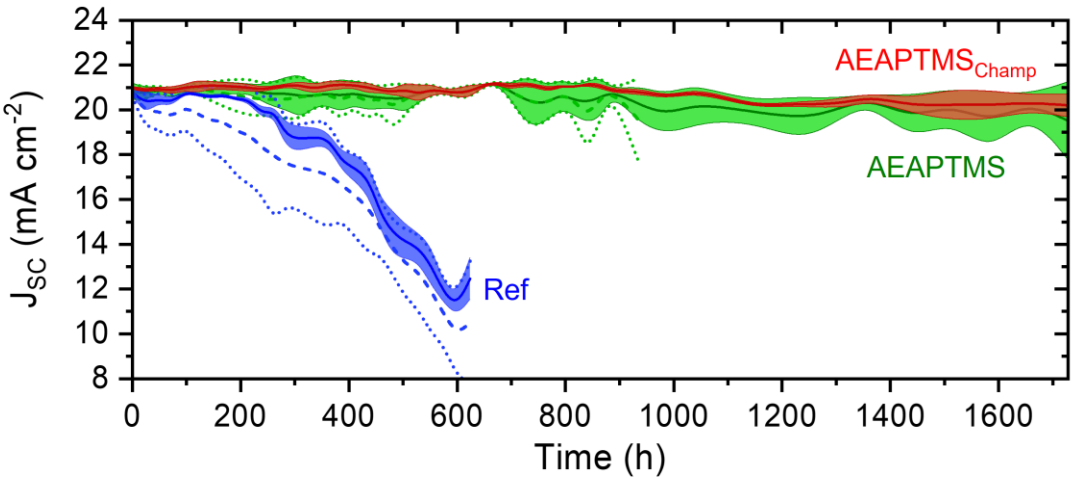

Fig. S33. Evolution of mean J_{SC} (with the corresponding standard deviations in a band plot) of encapsulated AEAPTMS-treated and reference $Cs_{13}Br_{10}$ cells (including six AEAPTMS-based and five reference cells) aged under the open-circuit condition and full-spectrum simulated sunlight at 85 ℃ in ambient air with relative humidity in the laboratory 50 ~ 60%.

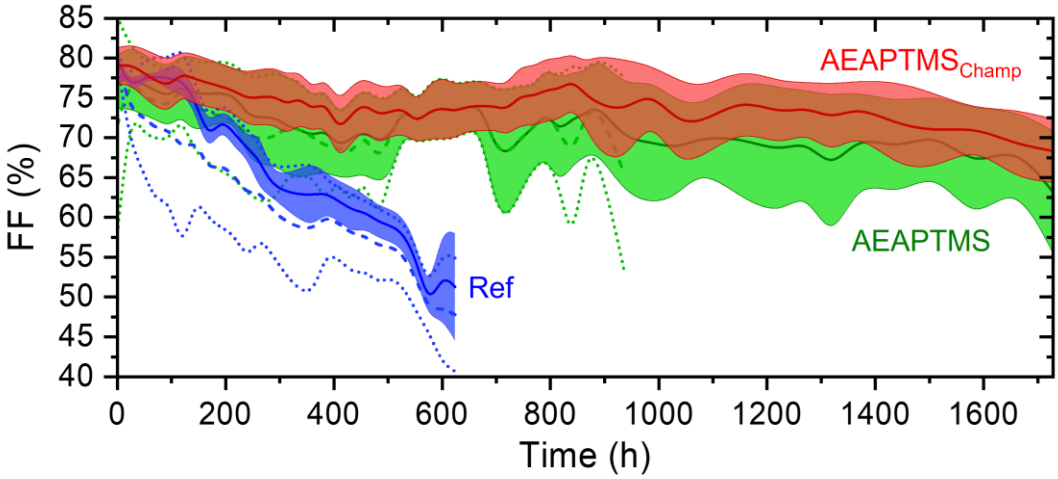

Fig. S34. Evolution of mean FF (with the corresponding standard deviations in a band plot) of encapsulated AEAPTMS-treated and reference $Cs_{13}Br_{10}$ cells (including six AEAPTMS-based and five reference cells) aged under the open-circuit condition and full-spectrum simulated sunlight at 85 ℃ in ambient air with relative humidity in the laboratory 50 ~ 60%.

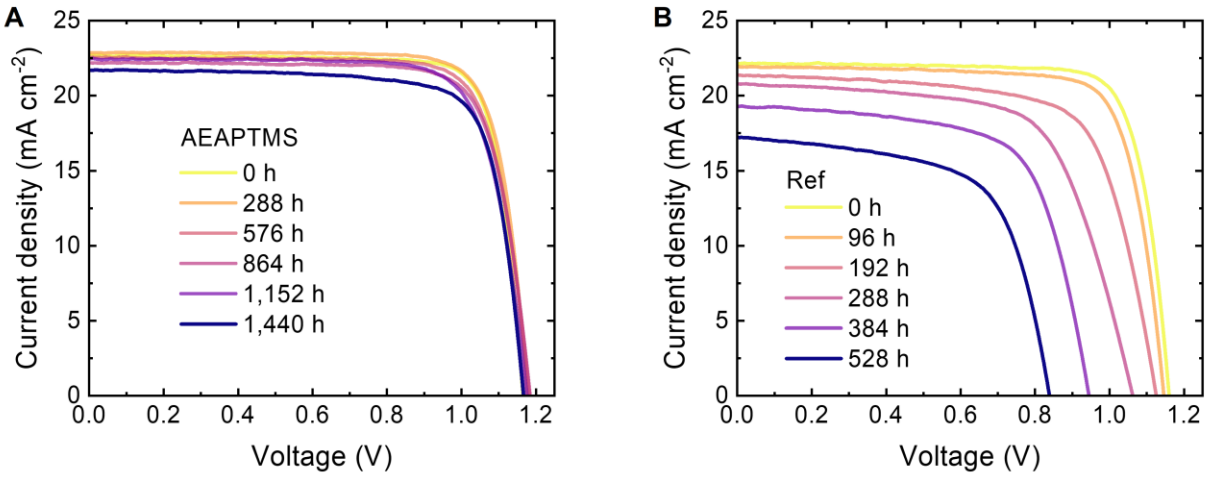

Fig. S35. (**A** and **B**) Representative current density and voltage characteristics of AEAPTMS-treated (A) and reference (B) $Cs_{13}Br_{10}$ cells obtained from FB-SC scans at various aging stages.

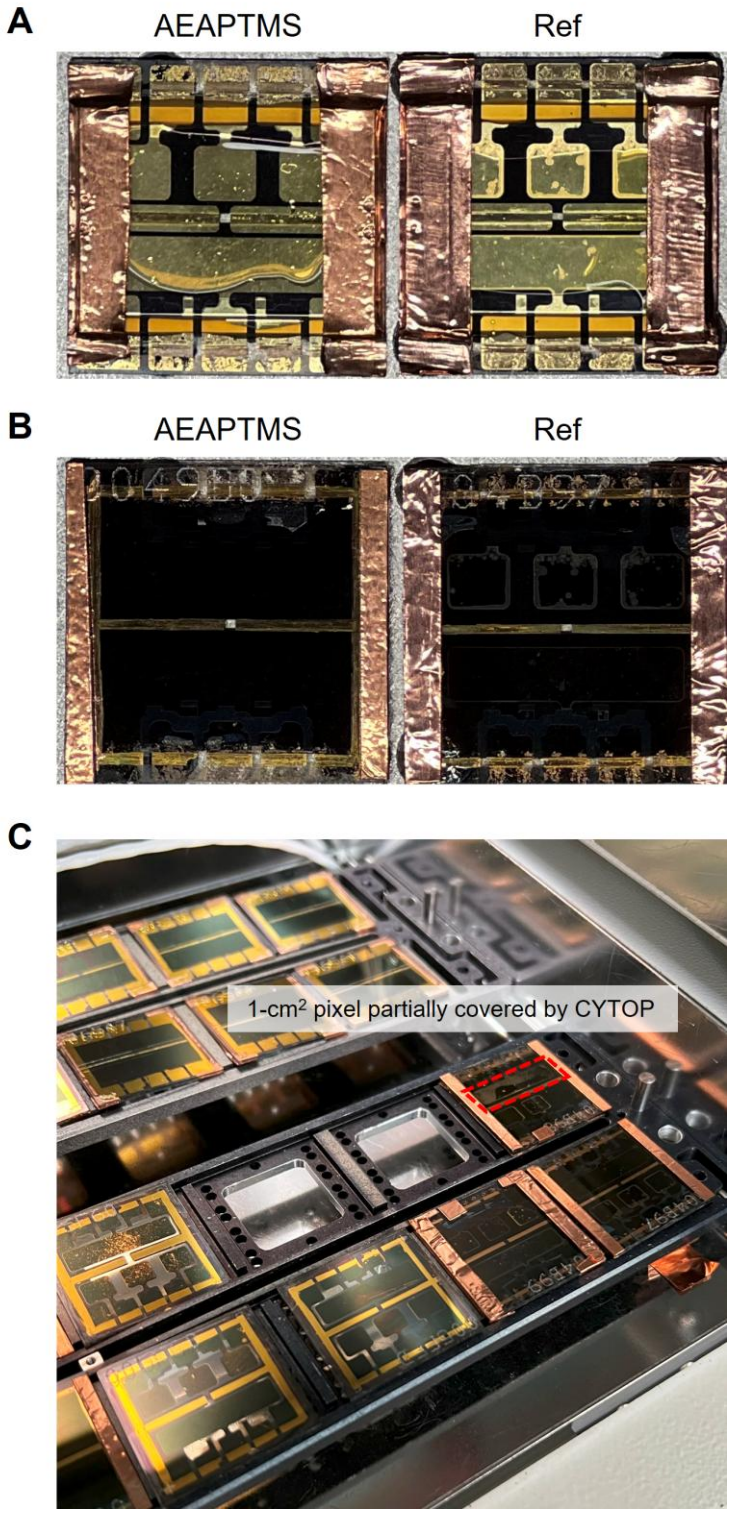

Fig. S36. (**A** and **B**) Photos of aged cells: (A) top electrode (Cr/Au) side; (B) bottom electrode (ITO) side. (**C**) Photo of cells in the ageing chamber, where a 1-cm^2 cell (indicated using a red box) exhibits discolouration in the non-CYTOP™ covered area

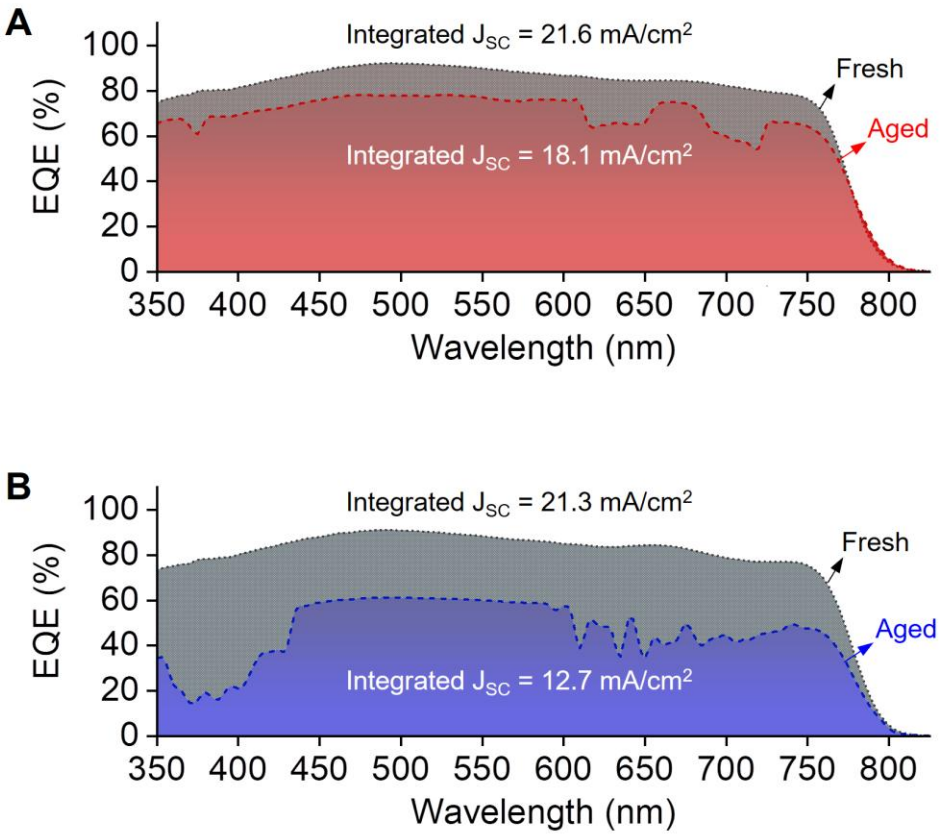

Fig. S37. (**A** and **B**) Evolution of EQE spectra before and after $Cs_{13}Br_{10}$ cells aged under an open-circuit condition and full-spectrum simulated sunlight at 85 ℃ in ambient air with relative humidity in the laboratory 50 ~ 60% with photocurrent integrated over the AM1.5 (100 mW cm^{-2}) solar spectrum and $Cs_{13}Br_{10}$ cells treated with (A) and without (B) the AEAPTMS molecule.

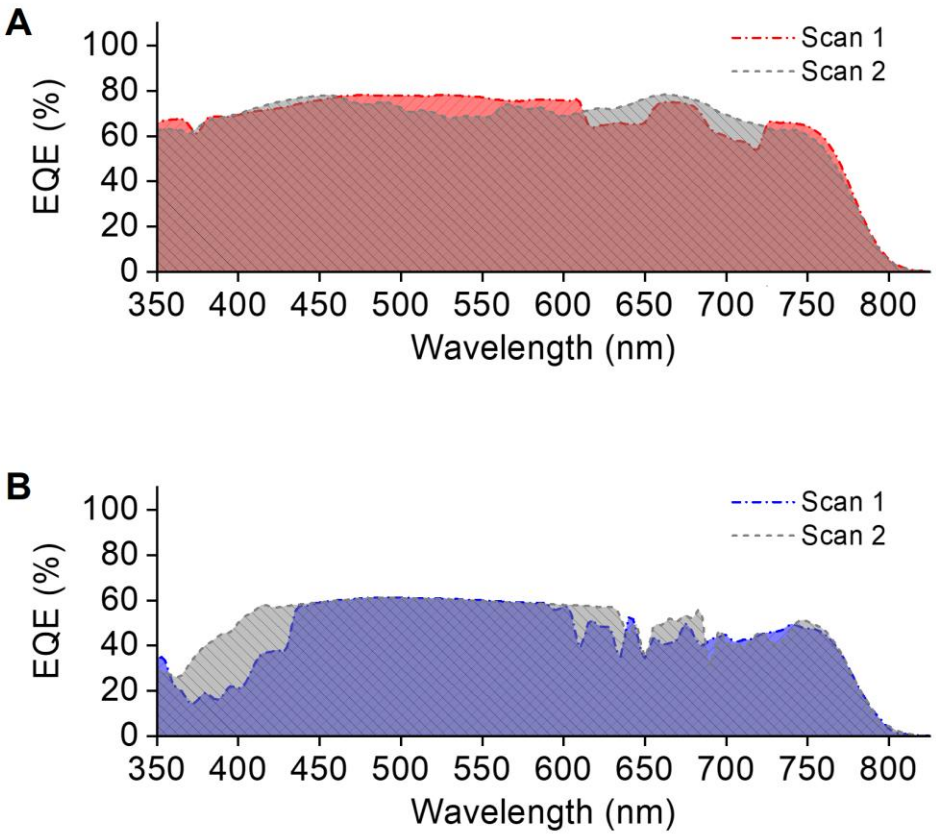

Fig. S38. (**A** and **B**) Successive EQE measurements for aged $C_{13}Br_{10}$ cells with (A) and without (B) AEAPTMS treatment, corresponding to fig. S37.

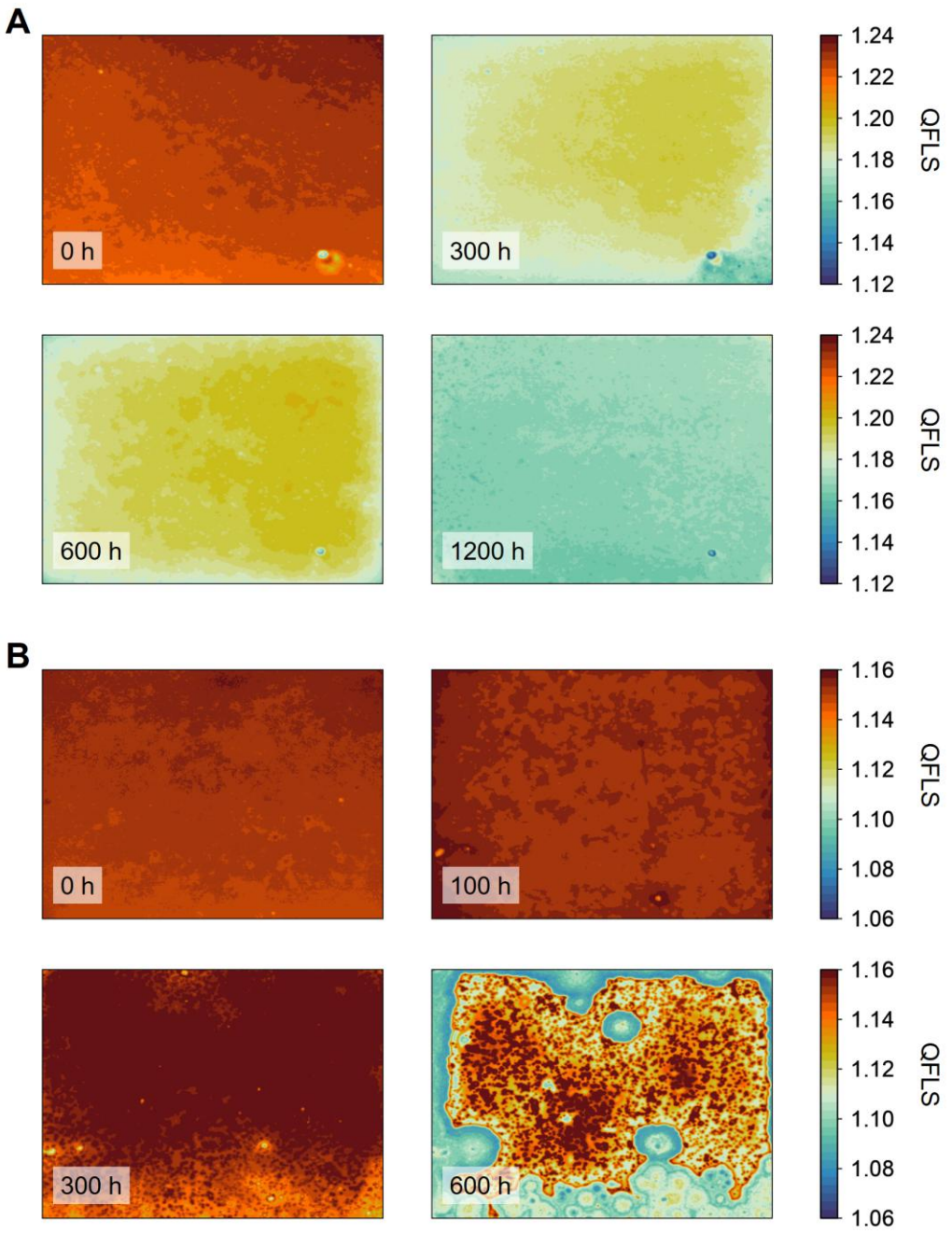

Fig. S39. (**A** and **B**) AEAPTMS-treated (a) and reference $Cs_{13}Br_{10}$ (b) cells before ageing (0 h) and after ageing for various periods of time. Each image represents an area of 5.38 mm × 4.67 mm.

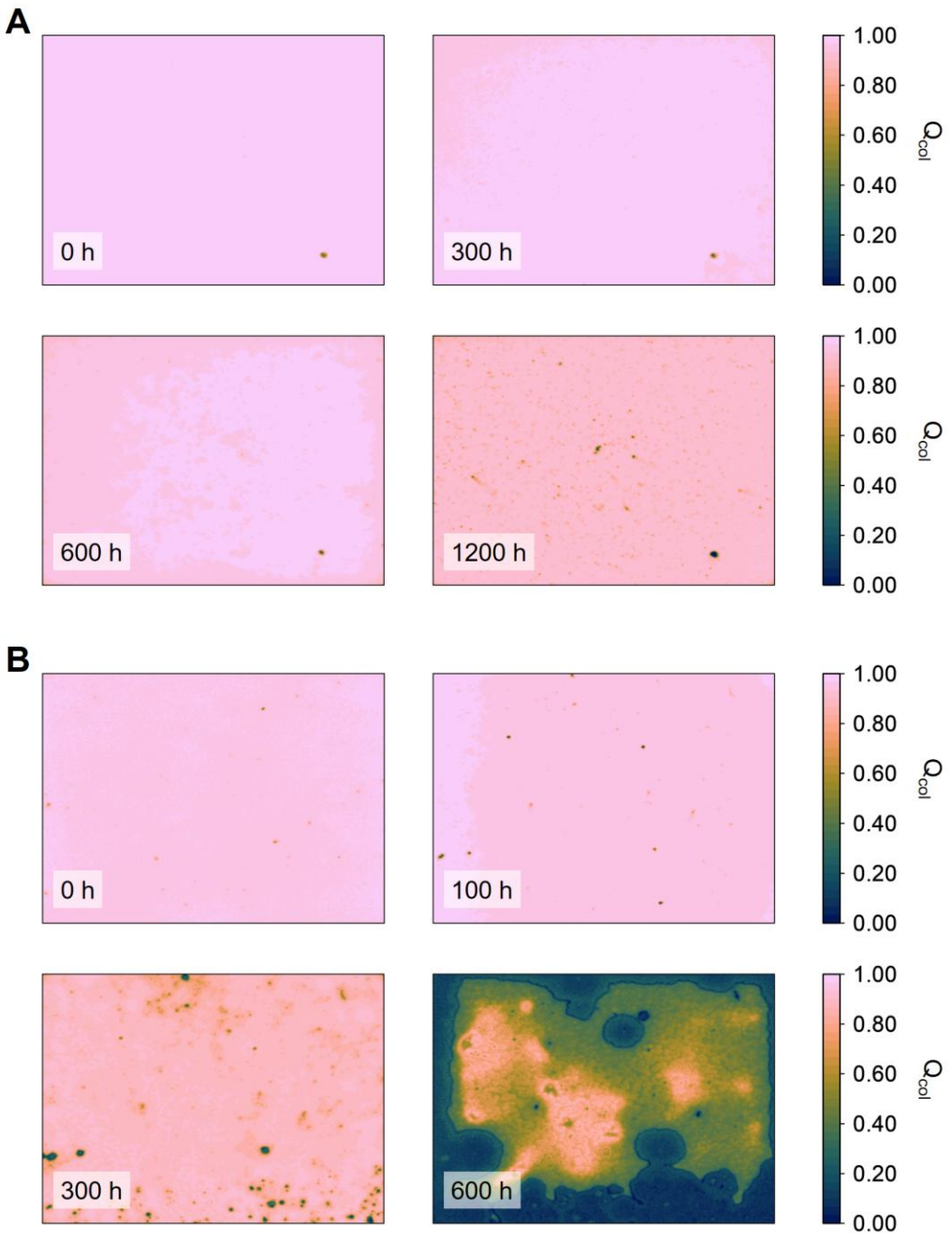

Fig. S40. (**A** and **B**) AEAPTMS-treated (A) and reference $Cs_{13}Br_{10}$ (B) cells before ageing (0 h) and after ageing for various periods of time. Each image represents an area of 5.38 mm × 4.67 mm.

Table S1. Full width at half maximum values for perovskite characteristic peaks.

2θ (°)	**Ref (°)**	**PTMS (°)**	**APTMS (°)**	**MAPTMS (°)**	**DMAPTMS (°)**	**AEAPTMS (°)**	**$(AE)_2$APTMS (°)**
13.891	0.113	0.111	0.271	0.115	0.123	0.103	0.217
19.709	0.084	0.080	0.214	0.081	0.098	0.079	0.161
24.236	0.076	0.075	0.179	0.087	0.085	0.084	0.144
28.086	0.075	0.073	0.289	0.057	0.050	0.048	0.138
31.501	0.078	0.074	0.239	0.065	0.081	0.074	0.133
34.607	0.082	0.083	0.232	0.084	0.098	0.077	0.124
40.187	0.082	0.075	0.273	0.082	0.081	0.077	0.115
43.953	0.089	0.068	0.225	0.082	0.093	0.078	0.137

Table S2. Corresponding PV performance parameters obtained for 1-cm^2 AEAPTMS-treated solar cells shown in Fig. 3D using $Cs_{13}Br_{10}$ (i.e., 1.60 eV), $Cs_{17}Br_{23}$ (i.e., 1.67 eV), and $Cs_{15}Br_{40}$ (i.e., 1.77 eV) as the light absorbers.

1-cm^2 cells	V_{OC} (V)	J_{SC} (mA cm^{-2})	FF (%)	PCE (%)	MPP (%)
1.60-eV AEAPTMS$_{FB-SC}$	1.20	23.01	80.4	22.2	21.9
1.60-eV AEAPTMS$_{SC-FB}$	1.20	23.00	77.2	21.3	
1.67-eV AEAPTMS$_{FB-SC}$	1.26	19.91	80.3	20.2	20.1
1.67-eV AEAPTMS$_{SC-FB}$	1.26	19.92	77.0	19.3	
1.77-eV AEAPTMS$_{FB-SC}$	1.34	16.96	80.2	18.2	18.4
1.77-eV AEAPTMS$_{SC-FB}$	1.35	16.97	79.4	18.1	

Table S3. Comparison of perovskite solar cells operational stability with representative literature works employing aging protocols closely follow the ISOS-L-3 standards (*47*).

Perovskite compositions	Device architecture	Aging conditions	Lifetime and efficiency at the end of aging	Ref.
Light source with full solar spectrum				
$Cs_{0.13}FA_{0.87}Pb(I_{0.90}Br_{0.10})_3$	**ITO/Me-4PACz/AlO_x/ PVSK/PCBM/BCP/Cr/Au (encapsulated)**	**Xenon lamp, open circuit, 85 °C, RH 50 ~ 60%, air**	**$T_{95\ for\ MPP,\ Champ\text{-}OC}$ = 1,600 hours MPP efficiency @ T_{95} = 19.4% $T_{95\ for\ PCE,\ Champ\text{-}OC}$ = 1,440 hours PCE @ T_{95} = 20.1%**	**This work**
$Cs_{0.05}MA_{0.05}FA_{0.90}PbI_3$	FTO/NiO_x/4PACz/PVSK/ DMDP/C_{60}/BCP/Ag (encapsulated)	LED solar simulator, MPP tracking, 65 °C, RH ~ 50%, air	$T_{96,\ Champ\text{-}MPP}$ = 2,000 hours MPP efficiency‡ @ T_{96} = 22%	(*23*)
$DMA_xCs_{0.17}FA_{0.83}Pb(I_{0.88}Br_{0.12})_3Cl_x$	FTO/PTAA/AlO_x/PVSK/ LiBr/C_{70}/Zr(acac)$_4$/Au (encapsulated)	Xenon lamp, open circuit, 85 °C, RH ~ 50%, air	$T_{80,\ Champ\text{-}OC}$ = 490 hours Steady-state PCE‡ @ T_{80} = 14%	(*49*)
$Cs_{0.17}FA_{0.83}Pb(I_{0.77}Br_{0.23})_3$	FTO/polyTPD/PVSK/ PCBM/BCP/Cr/Au (encapsulated)	Xenon lamp, open-circuit, 85 °C, RH ~ 50%, air	$T_{95,\ Average\text{-}OC}$ = 1,200 hours‡ Steady-state PCE @ T_{95}= 11.8%	(*52*)
$Cs_{0.05}MA_{0.14}FA_{0.81}PbI_{2.55}Br_{0.45}$	ITO/PTAA/PVSK/ $PbSO_4$/C_{60}/BCP/Cu (encapsulated)	Plasma lamp, MPP tracking, 65 °C, RH 60 ± 10%, air	$T_{96,\ Champ\text{-}MPP}$ = 1,200 hours MPP efficiency‡ @ T_{96} = 18%	(*54*)
$CsPbI_3$	FTO/TiO_2/Al_2O_3/PVSK/ $Cs_2PbI_2Cl_2$/CuSCN/Cr/Au (encapsulated)	Metal-halide lamp, MPP tracking, 85 °C, RH ~ 65%, air	$T_{85,\ Champ\text{-}MPP}$ = 4,000 hours‡ MPP efficiency‡ @ T_{85} = 14%	(*76*)
$Cs_{0.05}(MA_{0.17}FA_{0.83})_{0.95}Pb(I_{0.9}Br_{0.1})_3$	FTO/NiO_x/PVSK/PCBM/ BCP/Cr_2O_3/Cr/Au (encapsulated)	Xenon lamp, open circuit, ~ 75 °C, RH 40 ~ 50%, air	$T_{95,\ Average\text{-}OC}$ = 360 hours‡,‡ Steady-state PCE‡ @ T_{95} = 18%	(*77*)
Light source without full solar spectrum				
$Cs_{0.05}MA_{0.10}FA_{0.85}PbI_3$	FTO/2PACz:3-MPA/PVSK/ 345FAn/C_{60}/SnO_2/Ag (encapsulated)	White LED, MPP tracking, 65 °C, RH ~ 50%, air	$T_{95,\ Champ\text{-}MPP}$ = 1,075 hours MPP efficiency @ T_{95}= 21.9%	(*4*)
$Cs_{0.05}MA_{0.05}FA_{0.90}Pb(I_{0.95}Br_{0.05})_3$	FTO/2PACz/PVSK/ 345FAn/C_{60}/SnO_2/Ag (encapsulated)	White LED, MPP tracking, 85 °C, RH ~ 50%, air	$T_{85,\ Champ\text{-}MPP}$ = 1,560 hours MPP efficiency @ T_{85}= 16.8%	(*9*)
$Cs_{0.05}FA_{0.95}PbI_3$	FTO/NiO_x/Me-4PACz/DPPP/ PVSK/PEAI/C_{60}/SnO_2/Cr-Cu (encapsulated)	White LED*, open circuit, 85 °C, RH ~ 65%, oven	$T_{108,\ Champ\text{-}OC}$ = 1,500 hours PCE‡ @ T_{108} = 20%	(*21*)
$Cs_{0.05}MA_{0.10}FA_{0.85}PbI_3$	ITO/NiO_x/PVSK/3F-PEA/ C_{60}/SnO_2/Ag (encapsulated)	White LED, MPP tracking, 65 °C, RH ~ 50%, air	$T_{92,\ Champ\text{-}MPP}$ = 500 hours MPP tracking @ T_{92}= 21.9%	(*48*)
$Cs_{0.10}FA_{0.90}PbI_3$	ITO/PTAA/PVSK:$PEAMA^+$/ C_{60}/SnO_2/Cu (unencapsulated)	White LED, V_{OC}, 85 °C, nitrogen	$T_{90,\ Average\text{-}Voc}$ = 750 hours†,‡ PCE‡ @ T_{90} = 21%	(*50*)
$Cs_{0.05}MA_{0.05}FA_{0.90}PbI_3$	FTO/NiO_x/AlO_x/PVSK/ C_{60}/GABr/BCP/Ag (encapsulated)	LED, MPP tracking, 85 °C, RH ~ 65%, air	$T_{97,\ Champ\text{-}MPP}$ = 2,000 hours† MPP efficiency @ T_{97}‡ = 19.84%	(*78*)
$Rb_{0.05}Cs_{0.05}MA_{0.05}FA_{0.85}Pb(I_{0.95}Br_{0.05})_3$	FTO/NiO_x/MeO-2PACz/ PVSK/C_{60}/YbO_x/Cu (encapsulated)	White LED, MPP tracking, 85 °C, RH ~ 50%, air	$T_{85,\ Champ\text{-}MPP}$ = 500 hours MPP efficiency @ T_{85} = 20.06%	(*79*)
$Cs_{0.05}(MA_{0.15}FA_{0.85})_{0.95}Pb(I_{0.85}Br_{0.15})_3$	ITO/PTAA/PVSK/PCBM/ ZrL3:bis-C_{60}/BCP/Ag (encapsulated)	White LED, MPP tracking, 85 °C, nitrogen	$T_{92,\ Champ\text{-}MPP,\ PCE}$ = 1,000 hours PCE‡ @ T_{92} = 19%	(*80*)

PVSK: perovskite; OC: open circuit; MPP: maximum power point; PCE: power conversion efficiency; †: light-soaking; ‡: post-burn-in
*: In the literature work reported by C. Li et al. (*21*), the light source was placed outside the aging oven.
‡: Values were estimated based on extrapolations and interpretations of the data presented in the referenced literature.

Movie S1. Time-dependent GIWAXS patterns of an APTMS-treated perovskite film.

Movie S2. Time-dependent GIWAXS patterns of an APTMS-treated perovskite film with the background signals from air scattering, Kapton-taped window, glass, and ITO removed.

Movie S3. Time-dependent GIWAXS patterns of an AEAPTMS-treated perovskite film.

Movie S4. Time-dependent GIWAXS patterns of an AEAPTMS-treated perovskite film with the background signals from air scattering, Kapton-taped window, glass, and ITO removed.

Movie S5. APTMS vapor treatment on an $Cs_{13}Br_{10}$ perovskite film.

Movie S6. Electroluminescence signals recorded for a 1-cm^2 $Cs_{15}Br_{40}$ perovskite solar cell when sweeping between 0 and 4 V.

Movie S7. Water ingression test on an AEAPTMS-treated $Cs_{13}Br_{10}$ film (placed on the right side in the movie) and a reference $Cs_{13}Br_{10}$ film (placed on the left side in the movie).

References

57. J. C. de Mello, H. F. Wittmann, R. H. Friend, An improved experimental determination of external photoluminescence quantum efficiency. *Adv. Mater.* **9**, 230-232 (1997).
58. T. Kirchartz, J. A. Márquez, M. Stolterfoht, T. Unold, Photoluminescence-Based Characterization of Halide Perovskites for Photovoltaics. *Adv. Energy Mater.* **10**, 1904134 (2020).
59. A. M. Ulatowski, M. D. Farrar, H. J. Snaith, M. B. Johnston, L. M. Herz, Revealing Ultrafast Charge-Carrier Thermalization in Tin-Iodide Perovskites through Novel Pump–Push–Probe Terahertz Spectroscopy. *ACS Photonics* **8**, 2509-2518 (2021).
60. C. Wehrenfennig, M. Liu, H. J. Snaith, M. B. Johnston, L. M. Herz, Charge-carrier dynamics in vapour-deposited films of the organolead halide perovskite CH3NH3PbI3−xClx. *Energy Environ. Sci.* **7**, 2269-2275 (2014).
61. G. Ashiotis, A. Deschildre, Z. Nawaz, J. P. Wright, D. Karkoulis, F. E. Picca, J. Kieffer, The fast azimuthal integration Python library: pyFAI. *J. Appl. Crystallogr.* **48**, 510-519 (2015).
62. G. Kresse, J. Hafner, Ab initio molecular dynamics for liquid metals. *Phys. Rev. B* **47**, 558-561 (1993).
63. G. Kresse, J. Furthmüller, Efficient iterative schemes for ab initio total-energy calculations using a plane-wave basis set. *Phys. Rev. B* **54**, 11169-11186 (1996).
64. G. Kresse, J. Furthmüller, Efficiency of ab-initio total energy calculations for metals and semiconductors using a plane-wave basis set. *Comput. Mater. Sci.* **6**, 15-50 (1996).
65. P. E. Blöchl, Projector augmented-wave method. *Phys. Rev. B* **50**, 17953-17979 (1994).
66. J. P. Perdew, A. Ruzsinszky, G. I. Csonka, O. A. Vydrov, G. E. Scuseria, L. A. Constantin, X. Zhou, K. Burke, Restoring the Density-Gradient Expansion for Exchange in Solids and Surfaces. *Phys. Rev. Lett.* **100**, 136406 (2008).
67. S. Grimme, J. Antony, S. Ehrlich, H. Krieg, A consistent and accurate ab initio parametrization of density functional dispersion correction (DFT-D) for the 94 elements H-Pu. *J Chem Phys* **132**, 154104 (2010).
68. C. L. Davies, J. B. Patel, C. Q. Xia, L. M. Herz, M. B. Johnston, Temperature-Dependent Refractive Index of Quartz at Terahertz Frequencies. *J. Infrared Millim. Terahertz Waves* **39**, 1236-1248 (2018).
69. K. Galkowski, A. Mitioglu, A. Miyata, P. Plochocka, O. Portugall, G. E. Eperon, J. T.-W. Wang, T. Stergiopoulos, S. D. Stranks, H. J. Snaith, R. J. Nicholas, Determination of the exciton binding energy and effective masses for methylammonium and formamidinium lead tri-halide perovskite semiconductors. *Energy Environ. Sci.* **9**, 962-970 (2016).
70. A. Miyata, A. Mitioglu, P. Plochocka, O. Portugall, J. T.-W. Wang, S. D. Stranks, H. J. Snaith, R. J. Nicholas, Direct measurement of the exciton binding energy and effective masses for charge carriers in organic–inorganic tri-halide perovskites. *Nat. Phys.* **11**, 582-587 (2015).
71. V. D'Innocenzo, G. Grancini, M. J. P. Alcocer, A. R. S. Kandada, S. D. Stranks, M. M. Lee, G. Lanzani, H. J. Snaith, A. Petrozza, Excitons versus free charges in organo-lead tri-halide perovskites. *Nat. Commun.* **5**, 3586 (2014).
72. B. L. Henke, E. M. Gullikson, J. C. Davis, X-Ray Interactions: Photoabsorption, Scattering, Transmission, and Reflection at E = 50-30,000 eV, Z = 1-92. *At. Data Nucl. Data Tables* **54**, 181-342 (1993).

73. O. J. Weber, D. Ghosh, S. Gaines, P. F. Henry, A. B. Walker, M. S. Islam, M. T. Weller, Phase Behavior and Polymorphism of Formamidinium Lead Iodide. *Chem. Mater.* **30**, 3768-3778 (2018).
74. D. B. Mitzi, Synthesis, Crystal Structure, and Optical and Thermal Properties of (C4H9NH3)2MI4 (M = Ge, Sn, Pb). *Chem. Mater.* **8**, 791-800 (1996).
75. T. J. Jacobsson, A. Hultqvist, A. García-Fernández, A. Anand, A. Al-Ashouri, A. Hagfeldt, A. Crovetto, A. Abate, A. G. Ricciardulli, A. Vijayan, A. Kulkarni, A. Y. Anderson, B. P. Darwich, B. W. Yang, B. L. Coles, C. A. R. Perini, C. Rehermann, D. Ramirez, D. Fairen-Jimenez, D. Di Girolamo, D. L. Jia, E. Avila, E. J. Juarez-Perez, F. Baumann, F. Mathies, G. S. A. González, G. Boschloo, G. Nasti, G. Paramasivam, G. Martínez-Denegri, H. Näsström, H. Michaels, H. Köbler, H. Wu, I. Benesperi, M. I. Dar, I. B. Pehlivan, I. E. Gould, J. N. Vagott, J. Dagar, J. Kettle, J. Yang, J. Z. Li, J. A. Smith, J. Pascual, J. J. Jerónimo-Rendón, J. F. Montoya, J. P. Correa-Baena, J. M. Qiu, J. X. Wang, K. Sveinbjörnsson, K. Hirselandt, K. Dey, K. Frohna, L. Mathies, L. A. Castriotta, M. H. Aldamasy, M. Vasquez-Montoya, M. A. Ruiz-Preciado, M. A. Flatken, M. V. Khenkin, M. Grischek, M. Kedia, M. Saliba, M. Anaya, M. Veldhoen, N. Arora, O. Shargaieva, O. Maus, O. S. Game, O. Yudilevich, P. Fassl, Q. S. Zhou, R. Betancur, R. Munir, R. Patidar, S. D. Stranks, S. Alam, S. Kar, T. Unold, T. Abzieher, T. Edvinsson, T. W. David, U. W. Paetzold, W. Zia, W. F. Fu, W. W. Zuo, V. R. F. Schröder, W. Tress, X. L. Zhang, Y. H. Chiang, Z. Iqbal, Z. Q. Xie, E. Unger, An open-access database and analysis tool for perovskite solar cells based on the FAIR data principles. *Nat. Energy* **7**, 107-115 (2022).
76. X. Zhao, T. Liu, Q. C. Burlingame, T. Liu, R. Holley, G. Cheng, N. Yao, F. Gao, Y.-L. Loo, Accelerated aging of all-inorganic, interface-stabilized perovskite solar cells. *Science* **0**, eabn5679 (2022).
77. S. Bai, P. Da, C. Li, Z. Wang, Z. Yuan, F. Fu, M. Kawecki, X. Liu, N. Sakai, J. T.-W. Wang, S. Huettner, S. Buecheler, M. Fahlman, F. Gao, H. J. Snaith, Planar perovskite solar cells with long-term stability using ionic liquid additives. *Nature* **571**, 245-250 (2019).
78. Y. Yang, S. Cheng, X. Zhu, S. Li, Z. Zheng, K. Zhao, L. Ji, R. Li, Y. Liu, C. Liu, Q. Lin, N. Yan, Z. Wang, Inverted perovskite solar cells with over 2,000 h operational stability at 85 °C using fixed charge passivation. *Nat. Energy*, (2023).
79. P. Chen, Y. Xiao, J. Hu, S. Li, D. Luo, R. Su, P. Caprioglio, P. Kaienburg, X. Jia, N. Chen, J. Wu, Y. Sui, P. Tang, H. Yan, T. Huang, M. Yu, Q. Li, L. Zhao, C.-H. Hou, Y.-W. You, J.-J. Shyue, D. Wang, X. Li, Q. Zhao, Q. Gong, Z.-H. Lu, H. J. Snaith, R. Zhu, Multifunctional ytterbium oxide buffer for perovskite solar cells. *Nature* **625**, 516-522 (2024).
80. S. Wu, Z. Li, M.-Q. Li, Y. Diao, F. Lin, T. Liu, J. Zhang, P. Tieu, W. Gao, F. Qi, X. Pan, Z. Xu, Z. Zhu, A. K. Y. Jen, 2D metal–organic framework for stable perovskite solar cells with minimized lead leakage. *Nat. Nano.* **15**, 934-940 (2020).